Universität Stuttgart

Modeling and Simulation of Cabin Air Filtration with Focus on Electrostatic Effects

Von der Graduate School of Excellence advanced Manufacturing Engineering (GSaME) der Universität Stuttgart zur Erlangung der Würde eines Doktor-Ingenieurs (Dr.- Ing.) genehmigte Abhandlung

von

Carolin Schober

aus Miltenberg

Hauptberichter: Prof. Dr. rer. nat. habil. Miriam Mehl

Mitberichter: Univ.-Prof. Dr.-Ing. habil. Uwe Janoske

Tag der mündlichen Prüfung: 16. Mai 2019

Institut für Parallele und Verteilte Systeme (IPVS)

Universität Stuttgart

2019

Zusammenfassung

Innenraumfilter dienen dazu, Schadstoffe aus dem Luftstrom zu entfernen, der in den Fahrgastraum eintritt. Elektrostatische Ladungen auf den Filtermedien verbessern den Partikel-Abscheidegrad von Innenraumfiltern erheblich, ohne dabei die Luftdurchlässigkeit zu beeinflussen, und bewirken so eine deutliche Effizienzsteigerung. Um die Leistungskennzahlen zu optimieren, ist ein grundlegendes Verständnis der elektrostatischen Filtrationseffekte erforderlich. Diese Effekte sind jedoch aufgrund der begrenzten experimentellen Möglichkeiten weitgehend unerforscht.

Numerische Simulationen ermöglichen tiefere Einblicke in grundlegende physikalische Vorgänge als die Messung makroskopischer Größen. Der bisher standardmäßig verwendete, unidirektional gekoppelte Simulationsansatz führt jedoch für elektrostatisch geladene Systeme zu Abweichungen von experimentellen Ergebnissen. Zahlreiche unbekannte Parameter, wie die Ladungsverteilung auf Filterfasern und Staubpartikeln, und die fehlende Implementierung aller gleichzeitig wirkenden elektrostatischen Abscheidemechanismen sind die Ursache für diese Unterschiede.

Diese Dissertation liefert einen erweiterten, vollständig gekoppelten Modellierungsansatz zur Simulation spezifischer elektrostatischer Filtrationseffekte. Im neuen Simulationsmodell wird die Wechselwirkung stark bipolar geladener Staubpartikeln untereinander, mit Filterfasern und mit der Hintergrundströmung berücksichtigt. Umfangreiche Studien belegen die Notwendigkeit dieses hohen Detailgrades, um elektrostatische Agglomerationseffekte im Einströmbereich aufzulösen. Darüber hinaus liefert die Kombination aus numerischen und experimentellen Testszenarien qualitative Ergebnisse zur Auswirkung induzierter Dipole und Spiegelladungen. Die Verknüpfung des neuen, voll gekoppelten Modellierungsansatzes mit der bisherigen Standard-Simulationsmethode in einem zweistufigen Verfahren wird für weitere Forschungsarbeiten sehr empfohlen.

Abstract

Cabin air filters serve to remove harmful pollutants from the air flow supplied to the car passenger compartment. Electrostatic charges on cabin air filter media significantly improve the degree of particle separation without compromising the air permeability, thus achieving superior filtration performance. In order to optimize the performance metrics, a basic understanding of electrostatic filtration effects is required. However, these effects are largely unexplored due to limited experimental measurement options.

Numerical simulations allow a deeper insight into fundamental physical processes than the measurement of macroscopic quantities. However, the uni-directionally coupled status quo simulation approach leads to results deviating from experimental observations for electrostatically charged systems. Numerous unknown parameters such as the charge distribution on filter fibers and dust particles and the lacking implementation of all simultaneously effective electrostatic separation mechanisms cause these differences.

This dissertation provides an enhanced fully-coupled modeling approach to simulate specific electrostatic filtration effects. The new simulation model includes the interaction of highly bipolar charged dust particles with each other, with filter fibers, and with the background air flow. Extensive studies demonstrate the necessity of this high level of detail in order to dissolve electrostatic agglomeration effects in the inflow area. In addition, combined numerical and experimental test scenarios provide qualitative results allowing to observe the effect of induced dipoles and mirror charges. A combination of the fully-coupled modeling approach with the status quo simulation method in a two-step procedure is highly recommended for further research studies.

Acknowledgements

At this point, I would like to thank everyone who contributed to the success of this thesis. Without you this work would not have been possible.

First and foremost, I would like to thank my doctoral advisor Prof. Miriam Mehl for her tremendous commitment to the supervision and for sharing her valuable experience. I thank her for her constantly quick but constructive feedback and for giving me creative food for thought.

I would also like to thank Prof. Uwe Janoske from the university of Wuppertal for his willingness to take over the position as co-advisor.

I thankfully acknowledge the financial support from MANN+HUMMEL GmbH as well as the facilitation of international collaborations with colleagues from Raleigh and Bangalore. In particular, I would like to thank Florian Keller, David Keerl and Martin Lehmann for their professional supervision. Many thanks to Andreas Beck and Ralf Blum for the access to their fully utilized test facilities and for intensive discussions of experimentally obtained results.

Furthermore, I would like to thank the whole research groups at SGS and GSaME for a memorable time.

I would like to give many thanks to my friends Jule, Steffen, Anna, Nina, Jörn, Vani, Paul and Janna for giving me the necessary distraction in stressful times.

My special thanks to my parents, Monika and Andreas, and my sister Jennifer for their wholehearted support during this journey. Equally, I express my gratitude to my future parents-in-law, Heide and Harald, for their affectionate backing.

With all my heart I thank my future husband Simon, who always lovingly stood by my side despite all deprivation and strain. Without you, I wouldn't be where I am today.

Publications & Conference Contributions

In the course of this dissertation project, a number of publications and conference contributions were created.

The publications are listed here:

(1) C. Schober, D. Keerl, F. Keller, M. Lehmann, M. Mehl. "Influence of Bipolar Dust Particle Charges on the Filtration Efficiency of Wired Weaves." Submitted to: *Journal of Aerosol Science.*

(2) S. Hirschmann, M. Lahnert, C. Schober, M. Brunn, M. Mehl, D. Pflüger. "Load-Balancing and Spatial Adaptivity for Coarse-Grained Molecular Dynamics Applications." In: *High Performance Computing in Science and Engineering '18.* Springer (2018)

(3) C. Schober, D. Keerl, M. Lehmann, M. Mehl. "Simulating the Interaction of Electrostatically Charged Particles in the Inflow Area of Cabin Air Filters Using a Fully Coupled System." In: *Proceedings of the VII International Conference on Coupled Problems in Science and Engineering.* Rhodes (2017), pp. 77-88.

The conference contributions are listed here:

(1) C. Schober, D. Keerl, M. Lehmann, M. Mehl. "Simulation of Charged Particle Dynamics in the Inflow Area of Cabin Air Filter Media." Talk at: *American Association of Aerosol Research* 36^{th} *Annual Conference.* Raleigh (2017)

(2) C. Schober, D. Keerl, M. Lehmann, M. Mehl. "Modeling and Simulation of Electrostatically Charged Particle Dynamics in the Inflow and Transition Area of Cabin Air Filter Media." Talk at: *European Aerosol Conference.* Zurich (2017)

(3) C. Schober, D. Keerl, M. Lehmann, M. Mehl. "Simulating the Interaction of Electrostatically Charged Particles in the Inflow Area of Cabin Air Filters using a Fully Coupled System." Talk at: *VII International Conference on Coupled Problems in Science and Engineering.* Rhodes (2017)

(4) C. Schober, D. Keerl, M. Lehmann, M. Mehl. "Simulation der Wechselwirkungen zwischen elektrostatisch geladenen Partikeln im Anströmbereich von Innenraumfiltern." Talk at: *Jahrestreffen der ProcessNet-Fachgruppe Gasreinigung.* Frankfurt (2017)

(5) C. Schober, D. Keerl, M. Lehmann, M. Mehl. "Simulation of Cabin Air Filter Media – Molecular Dynamics vs. Continuum Approach." Talk at: *European Congress on Computational Methods in Applied Sciences and Engineering.* Crete (2016)

(6) C. Schober, D. Keerl, M. Lehmann, M. Mehl. "Simulation of Cabin Air Filtration in ESPResSo." Poster at: *ESPResSo Summer School.* Stuttgart (2015)

(7) C. Schober, M. Lehmann, M. Mehl, A. Scope. "Improving Filtration Efficiency by means of Electret Effect – collection of status quo and challenges." Poster at: 7^{th} *International Conference on Porous Media & Annual Meeting.* Padua (2015)

(8) C. Schober, D. Keerl, M. Lehmann, M. Mehl. "Molecular Dynamics for the Simulation of the Electret Effect?" Talk at: *Jahrestreffen der ProcessNet-Fachgruppen Adsorption und Gasreinigung.* Duisburg (2015)

Contents

1 Introduction **17**
1.1 Initial Situation 18
1.2 Problem Definition 19
1.3 Main Contributions 20

2 Fundamentals & State of Science **23**
2.1 Cabin Air Filters 23
2.1.1 Performance Metrics & Filtration Effects 24
2.1.2 Manufacturing & Electrostatic Charging the Filter Media 29
2.2 Experimental Test Facility for Cabin Air Filter Media 31
2.2.1 Test Rig 31
2.2.2 Test Aerosols 32
2.2.3 Corona Discharge Unit 33
2.2.4 Particle Measurement Techniques 34
2.3 Status Quo Simulation Approach 36
2.3.1 Continuum Mechanics 37
2.3.2 Lagrangian Approach 38
2.3.3 Electrostatic Fiber-Particle Interactions 40
2.3.4 Implementation in the Software Package GeoDict 40
2.4 Literature Review 43
2.4.1 Single Fiber Analysis 44
2.4.2 Complex Filter Structure Analysis 49
2.5 Summary & Research Issue 52

3 Enhanced Fully-Coupled Modeling of Air Filtration Processes 55
3.1 The Lattice-Boltzmann Method 57
3.2 Molecular Dynamics for Particle-Particle and Fiber-Particle Interactions 59
3.2.1 Particle Collisions 60
3.2.2 Particle Deposition on Filter Fibers 63
3.2.3 Electrostatic Particle-Particle and Fiber-Particle Interactions . . 63
3.3 Implementation in the Software Package ESPResSo 65
3.4 Coupling of the Model Components 69
3.5 Summary 70

4 Modeling & Simulation of Single Fibers 71
4.1 Verification of Four-Way Coupled Modeling Approach 72
4.1.1 Simulation Experiment Setup 72
4.1.2 Numerical Results for Mechanical Particle Collection 75
4.2 Uni-Directional Simulation of Charged Single Fibers 85
4.2.1 Simulation Experiment Setup 86
4.2.2 Numerical Results for Unipolar Fiber Charges 88
4.2.3 Numerical Results for the Expansion to Dipole Fibers 92
4.3 Uni-Directional Simulation of Charged Fiber Arrays 95
4.3.1 Simulation Experiment Setup 96
4.3.2 Numerical Results for Mixed Fiber Charges 100
4.4 Summary 109

5 Numerical & Experimental Analysis of Particle Dynamics 111
5.1 Fully-Coupled Simulation of Electrostatic Particle-Particle Interactions 112
5.1.1 Simulation Experiment Setup 113
5.1.2 Numerical Results 123
5.2 Uni-Directional Simulation of Particle Dynamics in the Test Facility . 133
5.2.1 Simulation Experiment Setup 133
5.2.2 Numerical Results 135
5.3 Experimental Analysis 140
5.3.1 Experimental Testing Setup 140
5.3.2 Experimental Testing Results 143
5.4 Summary 146

6 Numerical & Experimental Analysis of Wired Weaves 149
6.1 Specification of Wired Weaves 150
6.2 Experimental Analysis 152
6.2.1 Experimental Testing Setups 153
6.2.2 Experimental Testing Results 157
6.3 Simulation Study 168
6.3.1 Simulation Experiment Setup 168
6.3.2 Numerical Results 170
6.3.3 Remarks on Parallelization of the Simulations 176
6.4 Comparison of Simulation Results with Experiments 179
6.4.1 Electrostatically Neutral System 179
6.4.2 Influence of Electrostatically Charged Particles 181
6.5 Summary 183

7 Numerical & Experimental Analysis of Cabin Air Filter Media 185
7.1 Specification of Cabin Air Filter Media 186
7.2 Experimental Analysis 188
7.2.1 Experimental Testing Setup 189
7.2.2 Experimental Testing Results 192
7.3 Uni-Directional Simulation of Cabin Air Filter Media 198
7.3.1 Simulation Experiment Setup 198
7.3.2 Numerical Results & Comparison with Experiments 200
7.4 Summary 206

8 Conclusions & Future Work 209

List of Figures 213

List of Tables 217

List of Abbreviations 219

Bibliography 221

Declaration of Authorship 233

Chapter 1

Introduction

Very high particulate matter levels, especially in conurbations such as Stuttgart or Munich, are currently attracting nearly daily attention in the media and are nationally well-known. Fine dust particles with a mean aerodynamic diameter of 2.5 µm ($PM_{2.5}$) particularly pose a very high health risk as they can penetrate into the alveoli of the lungs by inhalation.

Cabin air filters are applied to prevent harmful particles such as pollen, fine dust and soot amongst others from being transferred through the HVAC (Heating, Ventilation, Air Conditioning) system into the interior (cabin) of a vehicle. Further improvement of the respective fibrous filter structures is essential due to steadily increasing requirements on air quality in car cabins as well as increasing exposure to pollutants at the same time – especially in fast-growing markets such as China. One promising approach to achieve enhanced filtration performance while maintaining high air permeability is the electrostatic charging of filter media. In such so-called electret filters, electrostatic filtration effects supplement the well-known mechanical collection mechanisms (such as inertia, diffusion, etc.). However, the lack of long-time stability of the electrostatic charges is a major problem and is not yet sufficiently understood.

Since traditional experimental development methods are very expensive and in addition reach their limits of feasibility in some respect, virtually prototyping filter media has been an ongoing research subject for years [62]. Computer-aided simulation tools enable a virtual separation of several simultaneously effective filtration mechanisms in order to make them specifically analyzable in terms of their impact. However, developing and validating suitable simulation models is

particularly challenging with regard to electrostatic separation mechanism. This thesis aims at contributing to understanding the complex underlying physical processes. The initial situation and derived problem definition are presented below. In the remainder of this chapter, the major contributions are condensed and the structure of this thesis is outlined.

1.1 Initial Situation

As mentioned above, the performance of a cabin air filter medium can be considerably improved by electrostatically charging the polymer fibers [24]. However, this positive effect does not persist for long as the fiber charge rapidly decreases due to neutralization by deposited particles, moisture and temperature effects. Prior enhancements of filter media have been primarily driven by trial and error. A variation of filter media characteristics such as grammage, porosity or fiber diameter distribution in combination with different charging parameters is applied to develop new filter media with improved filtration performances. Evaluating new filter media is carried out by measuring the three characteristic filter metrics, i.e., separation efficiency, pressure drop and dust holding capacity. Since this methodology of experimental development is very time-consuming and cost-intensive, knowledge-based optimization is intended to be performed instead. In particular with regard to electrostatic separation, however, the fundamental understanding is still missing. Numerical simulation methods are supposed to reveal new insights and potentials in this research field.

From a simulation point of view, well-established approaches regarding the conventional mechanical filtration process are already available. The software package GeoDict allows simulating the particulate air flow through porous filter media as well as the particle deposition and accumulation on fiber surfaces. With regard to electrostatic effects, however, the only effect implemented is the Coulomb force between charged fibers and particles. Further potentially important effects such as the interaction between electrostatically charged particles are completely neglected due to the high degree of complexity. On account of these major simplifications, the simulation results differ significantly from experimentally determined filtration efficiencies. Sophisticated measurement techniques allow determining the initial

collection efficiency for any combination of charged or discharged filter media with untreated (charged) or discharged dust particles. With each variation, different filtration mechanisms become effective resulting in different separation efficiencies. The uni-directionally coupled, status quo simulation approach provides satisfactorily consistent results with experiments for a completely neutral system of filter medium and particles. However, significant discrepancies occur as soon as electrostatic charges are considered on the filter fibers and/or the particles. Two factors mainly cause these discrepancies: Firstly, not all required electrostatic separation mechanisms are implemented in the simulation approach, and secondly the exact charge intensity and distribution on filter fibers and particles are not known.

1.2 Problem Definition

Simulating particulate air flow through cabin air filter media poses some major challenges. The main problem in reconstructing physical phenomena in experiments consists in the large number of unknown parameters. As mentioned above, electrostatic charge distributions and intensities on filter fibers and dust particles are not known as they are hardly accessible by experiments. Even a demanding determination of the net charge intensity on the surface of the filter medium does not allow drawing any conclusions about the bipolar charge distribution inside the filter medium. In addition to electrostatic parameters, the fluid flow conditions in the interior of the test facility are unobservable. Both the geometry of the test channel itself and the insertion of various measuring instruments could cause particles to behave differently in experiments than modeled in simulation studies. Furthermore, only macroscopic quantities such as the filtration efficiency are available from experiments and can be used for a comparison with simulation results. However, all mentioned uncertainties prevent a direct comparison. Therefore, the focus of this work is on analyzing the influence of individual filtration effects by simulation studies. To identify trends, particle-particle interactions and fiber-particle interactions based on various charge conditions are investigated. The results provide qualitative statements about the respective influence on the overall filtration performance.

1.3 Main Contributions

In essence, the main contributions of this thesis can be summarized as follows:

(1) An enhanced fully-coupled modeling approach is devised to study complex electrostatic effects appearing in cabin air filtration. In particular, the new approach features the simulation of short- and long-range particle-particle and fiber-particle interactions, in addition to a bi-directional coupling between the air flow and solid components.

(2) Extensive numerical studies of realistic, highly bipolar charged dust distributions demonstrate the necessity of the high coupling intensity between all components involved. The alteration of particle size and charge distributions by electrostatic particle-particle agglomeration is essential for simulating the ongoing filtration process.

(3) In addition to electrostatically induced particle movements, intense particle dynamics caused by hydrodynamics are detected in the complex test channel geometry. The simulated particle trajectories in the closed test channel are not visible in experimental analyses.

(4) Combining the fundamentally new modeling approach with the status quo uni-directional coupling method is highly recommended in order to exploit the benefits of both methods. Electrostatic and hydrodynamic effects can be simulated in two consecutive steps.

(5) A set of combined numerical and experimental test scenarios is defined to focus on specific filtration aspects. Qualitative results on the effect of charged filter media and dust particles by Coulomb attraction, induced mirror charges and dipole charges on the overall filtration efficiency are obtained.

(6) The usage of conductive wired weaves is proposed to – numerically and experimentally – further study and validate individual electrostatic filtration mechanisms.

Structure of the Thesis

Chapter 2 starts by providing a detailed insight into the design and the favorable functionality of cabin air filters. Subsequently, the status quo simulation approach for predicting the filtration performance is introduced and a concise review of previous relevant research developments is presented with focus on the respective simulation methodologies. The chapter concludes with the identification of the research gap and the derived research issues of this thesis.

The enhanced fully-coupled modeling approach conceived to solve these research issues is introduced in Chapter 3. In addition to the basic simulation methods used and their implementation in the software package ESPResSo, the chapter focuses on modeling important fiber-particle and particle-particle interactions for filtration processes.

In Chapter 4, this fundamentally new and basic modeling approach regarding cabin air filtration is thoroughly verified using the single fiber model. Furthermore, the influence of different charge distributions on the fiber surface is analyzed using simple fiber setups.

The fully-coupled modeling approach is used in Chapter 5 to investigate the degree of electrostatic particle-particle agglomeration based on diverse particle charge distributions. In addition to electrostatically induced particle dynamics, the particle behavior in a steady-state flow field through the complex test channel geometry is examined. The numerical analyses are supplemented by experimental measurements.

Chapter 6 is dedicated to the numerical and experimental analyses of wired weaves used as simple filter medium substitutes. The influence of specific electrostatic separation mechanisms is characterized on the basis of this conductive material.

The big picture of complex cabin air filtration including all relevant mechanical and electrostatic separation mechanisms is presented in Chapter 7. From a comparison of simulation results with experimental observations, implementations required in addition to the electrostatic effects regarded so far are derived.

Chapter 8 finally summarizes the key findings gained from this thesis and provides recommendations for future research activities.

Chapter 2

Fundamentals & State of Science

This chapter presents the basics of cabin air filtration from an application point of view. The structure as well as particularities of so-called electret filter media are described in detail in Sec. 2.1. Resulting mechanical and electrostatic filtration effects as well as their qualitative influences on established performance metrics are additionally addressed. The basic procedure to experimentally determine the filter performance metrics is described in Sec. 2.2. The focus is on the conception of the test facility used to compare and evaluate simulation results in this work. This includes a description of the test dust used, established particle measurement techniques and the particle discharge unit.

Furthermore, the fundamentals of the status quo simulation approach used to virtualize filtration processes are introduced in Sec. 2.3. After an extensive literature review about previous developments from a simulation perspective in Sec. 2.4, this chapter concludes with the definition of the research questions of this thesis.

2.1 Cabin Air Filters

Cabin air filters are part of the standard equipment in modern vehicles and serve to protect passengers in a car cabin from being exposed to various pollutants. Depending on the type of cabin air filter providing different levels of comfort, dust, pollen, soot, allergens and bacteria as well as unpleasent odors and noxious gases can be filtered out:

Particle filters eliminate particles such as fine dust, pollen and soot.

Combined filters are additionally equipped with a layer of activated carbon to adsorb noxious gases, e.g., NO_2, and unpleasant odors from the environment.

Bio-functional filters comprise a third, functional layer which prevents the growth of microorganisms on the filter media and inactivates captured allergens.

Although the electret effect to be investigated in this thesis plays an important role for all types of cabin air filters, it only refers to particle filters. Obviously, the results also apply to the particle filtration layer in the other two filter designs.

In order to reduce harmful particles in the incoming air stream as energy efficient as possible, fibrous structures are employed in particle filters. Since denser structures reduce the air permeability, these fibrous structures physically reach their limits for purely mechanical particle collection. Synthetic materials such as polypropylene (PP) or polytetrafluoroethylene (PTFE) enable the electrostatic charging of the fiber surfaces [18]. The electrostatic charges induce an additional attractive force between fibers and airborne particles resulting in a significantly improved filtration performance.

2.1.1 Performance Metrics & Filtration Effects

Three key performance indicators are established for the qualitative assessment of particle filter media: the collection efficiency, the pressure drop and the dust holding capacity.

The **collection efficiency** η is defined as the percentage of collected particles in relation to incoming particles. The denotation 'initial' collection efficiency is associated with the particulate flow through a clean, unladen filter medium.

The **pressure drop** Δp denotes the pressure difference between the positions upstream and downstream the filter medium due to flow resistance.

The **dust holding capacity** DHC describes the deposited particle mass with which a filter medium is loaded until a defined pressure drop increase is reached.

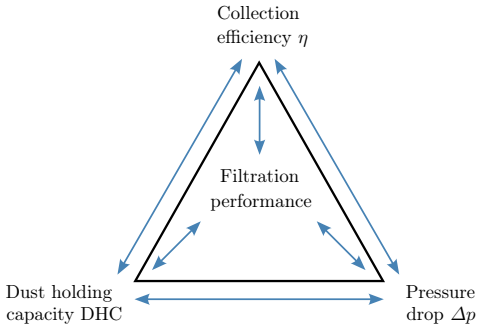

Figure 2.1: Interplay of the three key filtration performance indicators: collection efficiency, dust holding capacity and pressure drop. The axes represent the trade-offs between the metrics in the corners.

As illustrated in Fig. 2.1, the three parameters usually strongly depend on each other. For instance, an improvement in the collection efficiency by means of a denser fiber structure results in a higher pressure drop and lower dust holding capacity. Electret filters, however, offer the possibility to increase the collection efficiency without affecting pressure drop and dust holding capacity. In addition to the known mechanical collection mechanisms, electrostatic filtration effects become effective without changing the fibrous structure. All filtration mechanisms are presented below.

Figure 2.2 summarizes the trajectories of mechanically collected particles, i.e., collected due to diffusion, interception, inertia and sieving, on the basis of a single fiber. Additionally, Fig. 2.3 shows the specific impact of those mechanical collection mechanisms on the fractional collection efficiency. As one of the important mechanisms, Brownian motion ensures that small particles frequently hit the fibers due to temperature fluctuations in the air flow (diffusion). Large particles collide with the fibers due to their geometrical extension (interception) or cannot follow the streamlines fast enough on account of their masses (inertia). Sieving does not play a major role in the field of air filtration. Summing up the effect of all mechanical collection mechanisms yields a so-called most penetrating particle size (MPPS) in the range of 0.3 µm [60].

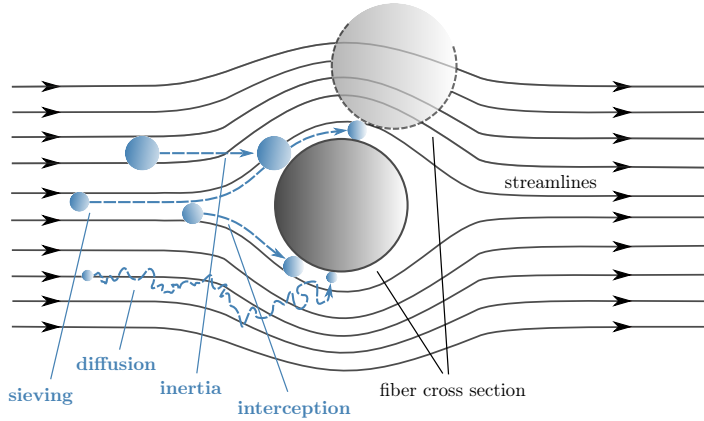

Figure 2.2: Schematic representation of trajectories for particles depositing on a single fiber due to different mechanical collection mechanisms, i.e., sieving, diffusion, inertia and interception. The particle collection through sieving requires a second fiber, which is indicated above the main one.

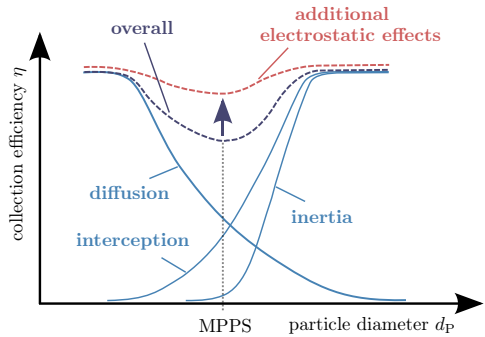

Figure 2.3: Qualitative curves of the collection efficiencies through the three major mechanical collection mechanisms of airborne particles presented in Fig. 2.2. The overall collection efficiency due to mechanical deposition is increased by electrostatic effects, especially in the range of the most penetrating particle size (MPPS).

Experiments show that the electrostatic separation mechanisms are very effective in particular in this area and enhance the filtration efficiency. The following effects are responsible for electrostatic separation:

Coulomb forces between opposing charge polarities on fibers and particles lead to a strong deflection of the particles towards the fibers [10, 29, 45, 47, 77, 111]. Likewise, the repulsive force between two equal charge polarities can cause particles to collide with adjacent fibers.

Induced dipoles are formed in neutral particles due to the propagated electrostatic field of charged fibers. Since the dipoles are always oriented towards the fiber charge, attractive forces act on the particles all the way around the fiber, even on the back side [10, 29, 45, 47].

Mirror charge effects occur when charged particles are in the vicinity of a fiber and induce image charges on its surface. The resulting attraction between fiber and particles also contributes to the overall filtration efficiency [10, 45].

Electrostatic agglomeration of charged dust particles in the inflow area results in a shifted particle size distribution towards bigger particles which in turn enhances the inertia collection mechanism. The adhesion of smaller particles to larger ones and their collection as an agglomerate increases the overall filtration efficiency. The agglomeration effect is usually neglected in literature due to the assumption of very low particle concentrations [85]. However, since electrostatic forces are long-range, particle-particle interactions and their impact on the filtration performance are one of the focal points in this work.

The four elucidated electrostatic separation mechanisms are schematically illustrated in Fig. 2.4.

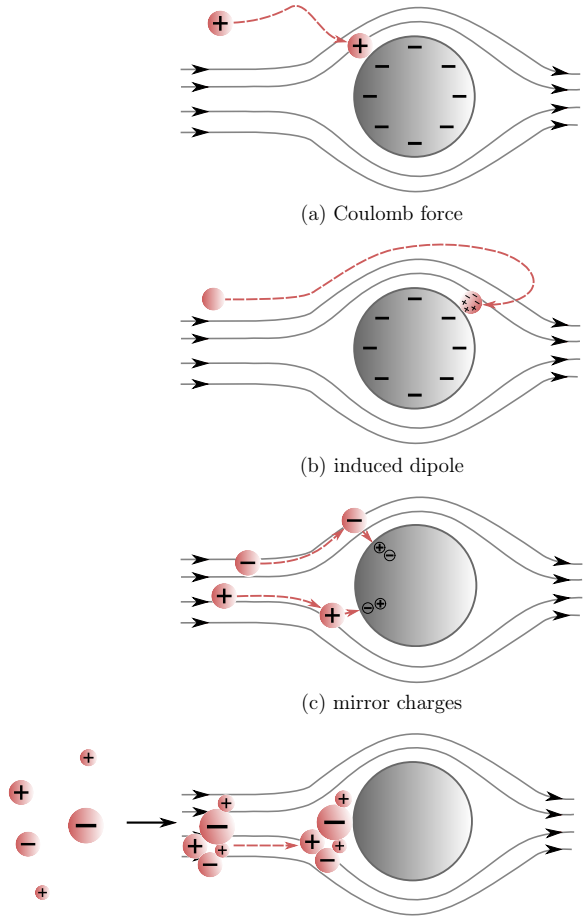

(a) Coulomb force

(b) induced dipole

(c) mirror charges

(d) electrostatic agglomeration

Figure 2.4: Schematic representation of the four electrostatic separation mechanisms by means of a single fiber: (a) Coulomb force, (b) induced dipole, (c) mirror charges and (d) electrostatic agglomeration. The first two mechanisms require an electrostatic charge on the fiber surface, while the separation in the two latter cases is caused by electrostatically charged particles only.

The trajectory based on mechanical and electrostatic mechanisms only indicates whether the particle collides with the fiber or not. Whether the particle really sticks to the fiber or bounces off again is determined by an energy balance. Therefore, the kinetic energy of the colliding particle is contrasted to adhesive forces. This results in a critical impact velocity

$$v_{\text{critical}} = \left(\frac{H}{4\,\pi\,\rho_{\text{P}}\,a_0\,\frac{d_{\text{P}}}{2}^2} \right)^{\frac{1}{2}} \tag{2.1}$$

for a particle with diameter d_{P} and density ρ_{P} hitting the fiber [40]. The Hamaker constant H defines the strength of the two-body van der Waals potential which is responsible for adhesion [36]. It depends on both, the material of the particle and the fiber, as well as on the medium in between. The variable a_0 denotes the minimal adhesion distance between the particle and the fiber surface. The fiber catches the particle if its velocity is smaller than v_{critical}. If the particle's velocity is larger than v_{critical}, the restitution coefficient $R \in [0, 1]$ determines the amount of energy remaining after the collision [41]. If the restitution coefficient is $R = 1$, no energy is lost through plastic deformation and the particle is reflected with the same velocity it had before the collision.

2.1.2 Manufacturing & Electrostatic Charging the Filter Media

The separation behavior of cabin air filter media significantly depends on the design of their microstructure. Relevant parameters such as the packing density or the fiber diameter distribution in turn are determined by the respective manufacturing process. The most established methods for the production of synthetic fibrous structures are the spunbond and the meltblown process. Since samples from both manufacturing processes are used in Chapter 7, they are briefly introduced below. In both processes, the nonwoven fabric is produced by melting thermoplastic polymer granulate.

In the **spunbond process**, the molten polymer is first extruded and subsequently stretched via spinnerets. The filaments are cooled directly with cold air when exiting the nozzles and are then placed on a conveyor belt. This manufacturing method produces rather coarse fibers with diameters over

$d_F = 20\,\mu m$ and a narrow distribution [7]. Hence, the spunbond nonwovens feature a high mechanical stability and a more open strucutre.

The **meltblown process** is based on the same principle as the spunbond process. However, the stretching takes place with heated air at high speed. This causes the fibers to be swirled in a turbulent open-jet. As a result, much finer fibers of $d_F = 1\,\mu m$ to $10\,\mu m$ are produced [7] resulting in a much denser fiber network.

The resulting different fiber sizes not only affect the mechanical collection mechanisms, but also the degree of electrostatic charging. The larger the specific surface area of the filter fibers, the more electrostatic charges can be absorbed. For the filter media analyzed in this thesis, corona charging is applied to generate charged surfaces on the insulating polypropylene material. Figure 2.5 shows a schematic sketch of the underlying principle based on a point-to-plane geometry [35].

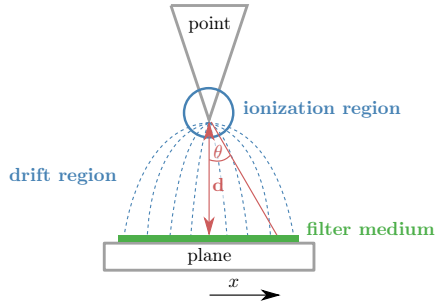

Figure 2.5: Corona charging a filter medium using a point-to-plane geometry for the electrodes. The distance d and the angle θ between the corona needle and the filter medium determine the charge intensity. The image is adapted from Giacometti and Oliveira [35] and Kilic et al. [52].

Between the two asymmetrically shaped electrodes (point and plane), a sufficiently high potential is required in order to initialize the ionization of the surrounding air. The strong electric field near the emitting electrode (point) allows for ionization of the insulating fluid. The resulting ions drift towards the low-field electrode (plane). Since ionization is limited to a region close to the high-field point electrode, the charging distance plays an important role regarding the emerging charge density

and distribution on the filter medium. According to Warburg's law

$$I(x) = I(0)\frac{cos^5\theta}{2d^2}, \tag{2.2}$$

the distance d and the angle θ between the corona needle and the filter sample determine the charge uniformity over the sample [52]. The corona current $I(0)$ at the point of the corona needle ($x = 0$) is preset. In addition, charging time, temperature and humidity have an influence on the charging state. The corona charging method results in quasi-permanently charged filter fibers, which are then called electret fibers [103].

2.2 Experimental Test Facility for Cabin Air Filter Media

To determine the performance factors of cabin air filter media shown in Fig. 2.1, defined testing procedures according DIN 71 460-1 [27] should be followed. The standard specifies certain test conditions in order to obtain comparability between different filter media. The modular test rig configured according to the standard and used to determine fractional collection efficiencies in this work is introduced in Sec. 2.2.1. Furthermore, the generally used test aerosols and how the particles can be electrostatically discharged in the measurements is presented in Sec. 2.2.2 and Sec. 2.2.3. Finally, different particle measurement techniques employed in this work are described in detail in Sec. 2.2.4.

2.2.1 Test Rig

The modular filter media test rig MFP 3000 from Palas GmbH [75] is used to measure fractional collection efficiencies in this work. Figure 2.6 shows the schematic setup including the aerosol provision at the inlet, the upstream and downstream particle sample collection and the optional corona discharge unit.

The test dust is dispersed via a preceding dispersion unit. In this work, the rotating brush generator RBG 1000 from Palas GmbH is used. The other two aerosols which are presented in Sec. 2.2.2 are atomized. The dispersed test dust can subsequently be neutralized by means of a corona discharge unit. Afterwards, the particles are injected to the actual test channel from the top. At each of the

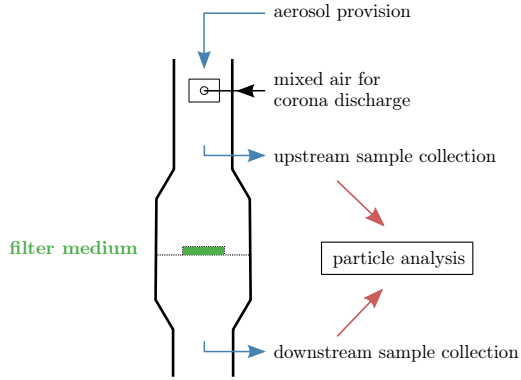

Figure 2.6: Basic measurement setup used to determine fractional collection efficiencies with an MFP 3000 test rig. The setup involves the aerosol provision, an optional corona discharge unit and a quasi-simultaneous measurement of the particle size distribution upstream and downstream the filter medium.

two sample collection points, the respective particle size distribution is determined. According to

$$\eta(d_\mathrm{P}) = 1 - \frac{N_\mathrm{inlet}(d_\mathrm{P})}{N_\mathrm{outlet}(d_\mathrm{P})}, \tag{2.3}$$

where $N_\mathrm{inlet}(d_\mathrm{P})$ and $N_\mathrm{outlet}(d_\mathrm{P})$ denote the number of particles of the size class d_P in the inlet and outlet distribution, the fractional collection efficiency of the filter medium is finally calculated. For the standard testing setup shown, the inlet and outlet distributions correspond to the raw (upstream) and clean (downstream) gas. In the course of this work, however, also modified setups are used. This will be explicitly pointed out in the respective sections. All individual units deployed are explained in detail below.

2.2.2 Test Aerosols

Three different aerosols are used in this work to analyze filtration performances: ISO fine dust, sodium chloride and DEHS particles. Primarily, ISO fine dust is used and also taken as a basis for simulation studies. Only the analysis of real filter media in Chapter 7 additionally refers to the two further aerosols.

ISO fine dust. Arizona desert sand resembles the materials to which cabin air filters are usually exposed during use. The first part of ISO 12103 [44] specifies four grades (A1-A4) of test dusts made from this Arizona desert sand. As a standard test dust for cabin air filters, the ISO fine dust (A2) is generally used for the experiments in this work unless otherwise stated. It mainly consists of quartz with particle diameters up to $d_P = 80\,\mu m$.

As mentioned above, ISO fine dust is dispersed using a rotating brush in this work. Due to the friction of the bristles, the particles are assumed to be strongly electrostatically charged. If needed, a subsequent discharge of the dust particles is possible in order to omit the electrostatic influence on the filtration efficiency in the experimental measurements.

Sodium chloride (NaCl). The mineral commonly known as salt is also a standard aerosol for testing filter media. The atomization of an initial saline solution provides a stable and reproducible particle distribution. In contrast to ISO fine dust particles, NaCl particles are in the submicron range ($d_P < 1\,\mu m$). In addition to particle size, NaCl particles also differ from dust particles in shape and state of charge.

Di-Ethyl-Hexyl-Sabacat (DEHS). This material is a liquid which is insoluble in water. Due to the fact that is a liquid, the atomized particles are spherical in good approximation. DEHS is also highly suitable for stable aerosol generation.

2.2.3 Corona Discharge Unit

The corona discharger CD 2000 from Palas GmbH [75] is used in this work to neutralize the ISO fine test dust. This explicitly allows disregarding the influence of electrostatic particle charges on the filtration efficiency in several instances. As shown in Fig. 2.6, an additional mixed air flow is connected for this purpose. By corona discharge, this air flow is enriched with ions in two ionization chambers beforehand. This requires the application of high positive and negative voltages. Subsequently, the resulting free ions meet the bipolarly charged dust particles in the illustrated mixing chamber and balance their charge. Depending on the charge intensity of the dust particles, their concentration and their residence time

in the mixing chamber, the electrostatic charge is either only reduced or completely removed. As stated by the manufacturer, the principle also allows explicit charging of particles. However, the corona discharge unit is only used to reduce particle charge intensities in this work.

2.2.4 Particle Measurement Techniques

Various measuring instruments are available for the particle analysis in the test channel. The aim of the analysis is to count the particles and classify them according their size in order to calculate the filtration efficiency from Eq. (2.3). For this purpose, three devices with different functional principles are used in this work: the optical particle counter, the aerodynamic particle sizer and the scanning mobility particle sizer. The fundamentals of all three particle measurement techniques are explained below.

Optical Particle Counter (OPC). The basis of the optical particle counter is the photometric determination of the respective particle diameters. In this work, the light-scattering spectrometer Welas® Digital 3000 from Palas GmbH [75] is employed. With the Welas device, the particles of interest flow through a defined measuring volume with a constant volume flow rate $\dot{V} = 4\,\mathrm{l/min}$. A xenon light source is mounted in such a way that it radiates white light into this measuring volume at an angle of 90°. When the light hits a particle, it is scattered by it. The scattered light, which is proportional to the particle's diameter, is subsequently detected by a photomultiplier. Since the light scattering depends on the refractive index of the particle's material, corresponding calibration curves are provided. This method allows particle detection within a range of 200 nm to 100 µm. Depending on the test aerosol used, one can choose from four different size ranges with the Welas® Digital 3000. For instance, the appropriate range for ISO fine dust is 0.3 µm to 17 µm. The optical determination of particle diameters is limited by the particle concentration. If there are too many particles P in the measuring volume, some particles stay hidden behind other particles and are thus not detected. The manufacturer specifies a limit of $10^6\,\mathrm{P/cm^3}$.

Aerodynamic Particle Sizer (APS). In contrast to light-scattering spectrometry, the aerodynamic particle sizer measures particle diameters independently of the materials refractive index. The model 3321 from TSI® [98] is used in this work. It measures the time that a particle needs to pass a certain distance in a defined accelerating flow field. For this purpose, a high-speed timing processor including a light barrier is employed. The aerodynamic diameter

$$d_{\mathrm{P,aer}(\rho)} = d_{\mathrm{P,aer}(\rho_{\mathrm{ref}})} \sqrt{\frac{\rho_{\mathrm{ref}}}{\rho}} \tag{2.4}$$

is defined as the physical diameter of a spherical reference particle, which has the same flight velocity as the concerning particle [106]. For reference, polystyrene latex particles with $\rho_{\mathrm{ref}} = 1050\,\mathrm{kg/m^3}$ are common. The amount of particles in the measuring section is controlled via an upstream dilution stage. This way, recommended particle concentrations for the APS method range from $0.001\,\mathrm{P/cm^3}$ to $1000\,\mathrm{P/cm^3}$. The APS measuring method allows for sizing particles in the range of 0.5 µm to 20 µm. Since flow resistance and inertial effects are decisive for the measured diameter, the shape factor of particles is, unlike in the OPC, also taken into account.

Therefore, discrepancies are expected between APS and OPC results especially for non-spherical particles with rough surfaces. The DIN 71460-1 [27] standard gives an approximate conversion formula between the two diameters according to

$$d_{\mathrm{OPC}} = d_{\mathrm{APS}} \sqrt{\frac{1}{\rho_{\mathrm{P}}}}. \tag{2.5}$$

Scanning Mobility Particle Sizer (SMPS). In contrast to the measurement techniques presented so far, the SMPS serves to analyze nanoparticles. Therefore, the SMPS is only used in Chapter 7 to determine the particle size distributions of alternative aerosols, i.e., NaCl and DEHS. The model 3080 electrostatic classifier from TSI [98] used in this work allows analyzing particles with $d_{\mathrm{P}} = 2\,\mathrm{nm}$ to 1000 nm. The underlying principle is based on a selection due to the particles' electrical mobility. This electrical mobility describes the ability of a particle to

cross an electric field $\mathbf{E}$ and is defined according to

$$\mu = \frac{\|\mathbf{v}_\mathrm{d}\|}{\|\mathbf{E}\|}, \tag{2.6}$$

where $\mathbf{v}_\mathrm{d}$ denotes the drift velocity. The SMPS contains a differential mobility analyzer (DMA), which is used to determine the electrical mobility μ of the particles. The DMA consists of a cylinder with an inner and outer electrode. By applying a voltage, a radially symmetrical electric field is generated inside the pillar. Based on a laminar auxiliary air flow and the electric field, the aerosol particles are carried through. Depending on the inertia, the particles are transported at different distances before colliding with the inner electrode. After a certain length, a small gap is arranged at this electrode through which monodisperse particles emerge. The idea of the SMPS is scanning through different applied voltages to allow different particle sizes to pass the gap. In a downstream step, the particles escaping from the gap are counted using a condensation particle counter (CPC). For particle counting, the model 3775 from TSI [98] is employed in this work. For the principle to work, a defined charge distribution of the aerosol must be ensured in a preceding step.

2.3 Status Quo Simulation Approach

The simulation of particulate flow through cabin air filter media requires the implementation of three components: a flow solver, an electrostatic solver and a particle tracker. Since solid and fluid phase interact with each other, forces have to be exchanged via a coupling. The status quo simulation used so far to investigate and virtually enhance the filtration performance of filter media is based on a uni-directionally coupled modeling approach. As schematically illustrated in Fig. 2.7, the status quo approach, thus, considers a one-way exchange of forces only. From both the fluid flow and the electrostatic field, forces are transmitted to the particles. The retroactive effects are neglected based on the assumption that particle motion exerts no or very little influence on the flow field. Furthermore, particle-particle interactions through collisions or electrostatic attraction are also omitted.

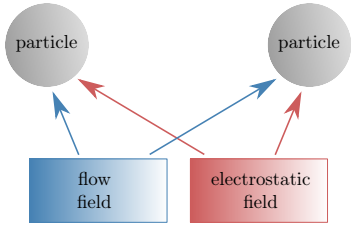

Figure 2.7: Schematic illustration of the uni-directionally coupled status quo simulation approach. The approach only takes a one-way influence between hydrodynamics, electrostatics and solid particles into account: from the flow and electrostatic fields to particle motion. Note that, the electrostatic field is only induced by charged filter fibers in this case and only acts on charged particles. The electrostatic interaction between charged particles is neglected.

The well-established software GeoDict [108] provided by Math2Market GmbH and used in this work applies a continuum approach for the simulation of the air flow through the unladen porous filter medium. The calculation of the electrostatic field is based on solving the Poisson equation. To subsequently model the particle transport, a Lagrangian approach is used. The following sections introduce the fundamentals of the individual methods mentioned above. Finally, their implementation in the software package GeoDict and the procedure for the simulation of filtration processes is presented.

2.3.1 Continuum Mechanics

The fluid dynamics method is based on the assumption that the observed fluid is continuously distributed in the space it occupies. The behavior of the fluid is described by macroscopic state variables such as density, temperature and velocity. Since these functions are continuous, the values can be calculated in three spatial dimensions at any point in time. The underlying mathematical model consists of a system of partial differential equations (PDEs) of second order. It is derived by the division of the continuum into individual, connected volume elements, in which the conservation of physical quantities is applied. In order to model the fluid behavior in a simulation domain $\Gamma \in \mathbb{R}^3$ for the time period $t \in [0, t_{\text{end}}]$, momentum and

mass conservation according to

$$\rho\Big(\underbrace{\frac{\partial \mathbf{u}(\mathbf{x},t)}{\partial t}}_{\text{velocity change}} + \underbrace{(\mathbf{u}(\mathbf{x},t)\cdot\nabla)\,\mathbf{u}(\mathbf{x},t)}_{\text{convection}}\Big) = \underbrace{-\nabla p(\mathbf{x},t)}_{\text{pressure gradient}} + \underbrace{\mu\Delta\mathbf{u}(\mathbf{x},t)}_{\text{diffusion}} + \underbrace{\mathbf{f}(\mathbf{x},t)}_{\text{external force}},$$

$$\underbrace{\nabla\cdot\mathbf{u}(\mathbf{x},t)}_{\text{mass balance}} = 0 \tag{2.7}$$

must be ensured. The change in the fluid velocity $\mathbf{u}(\mathbf{x},t)$ over time thus requires a convection and a diffusion term to conserve momentum. The left-hand side of the first equation with ρ being the fluid density, describes the inertial fluid transport along the flow. On the right-hand side, the acceleration due to a pressure gradient $\nabla p(\mathbf{x},t)$ and due to external forces $\mathbf{f}(\mathbf{x},t)$ is considered in addition to the diffusion term with the dynamic viscosity μ. The conservation of mass is mathematically ensured by a divergence-free velocity field as the focus is on incompressible flow. The combination of both conservation laws together is well-known as the Navier-Stokes equations. For a small Reynolds number implying a laminar fluid flow, the inertial term, i.e., convection, and time-dependence can be neglected yielding the Stokes equations

$$0 = -\nabla p(\mathbf{x},t) + \mu\Delta\mathbf{u}(\mathbf{x},t) + \mathbf{f}(\mathbf{x},t), \quad \nabla\cdot\mathbf{u}(\mathbf{x},t) = 0 \quad \text{in } \Gamma\times[0,t_{\text{end}}]\,. \tag{2.8}$$

2.3.2 Lagrangian Approach

The simulation of the particle transport in the uni-directionally coupled simulation is based on the previously calculated flow field. Taking the friction between the fluid and the particles as well as external forces into account, the motion of particles in the stationary flow field is calculated. Thereby, the geometrical expansion of particles is omitted such that only their mass centers are tracked. According to Newton's second law

$$\mathbf{F}(\mathbf{x},t) = m\,\frac{d\mathbf{v}(\mathbf{x},t)}{dt}, \tag{2.9}$$

the acceleration of a particle at position $\mathbf{x}$, time t and with the velocity $\mathbf{v}(\mathbf{x},t)$ and mass m is calculated based on the attacking forces $\mathbf{F}(\mathbf{x},t)$. The Lagrangian

formulation

$$\frac{d\mathbf{v}(\mathbf{x},t)}{dt} = \underbrace{\gamma\left(\mathbf{u}(\mathbf{x},t)-\mathbf{v}(\mathbf{x},t)\right)}_{\text{friction}} + \underbrace{\frac{q\mathbf{E}(\mathbf{x},t)}{m}}_{\text{electrostatics}} + \underbrace{\mathbf{B}(\mathbf{x},t)}_{\text{Brownian motion}} + \underbrace{\mathbf{f}(\mathbf{x},t)}_{\text{external forces}} \tag{2.10}$$

includes all relevant forces acting on the particle at position $\mathbf{x}$ at time t yielding an ordinary differential equation (ODE). The drag force from the fluid on a spherical particle is calculated via the friction coefficient

$$\gamma = 6\pi\mu\frac{R}{C_{\mathrm{C}}} \tag{2.11}$$

in the first term on the right-hand side. This coefficient depends on the fluid viscosity μ and the particle radius R. When calculating the drag on very small particles, a Cunningham correction factor $C_{\mathrm{C}} \neq 1$ is used to account for non-continuum effects instead of no-slip conditions [12]. The subsequent term takes into account the electrostatic interaction of any existing particle charge q among an external electric field $\mathbf{E}$ generated by the filter fibers. Note that, the electrostatic force term only considers the electrostatic field induced by the filter fibers acting on charged particles. In particular, effects on neutral particles such as the above mentioned induced dipoles are neglected. The term $\mathbf{B}(\mathbf{x},t)$ in the Lagrangian equation corresponds to modeling the diffusive motion of small particles. The time-steady process of Brownian motion can be modeled independently for each particle at position $\mathbf{x}$ at time t according to

$$\mathbf{B}(\mathbf{x},t) = \sigma d\mathbf{W}(\mathbf{x},t), \tag{2.12}$$

with

$$\sigma^2 = \frac{2k_B T\gamma}{m}. \tag{2.13}$$

The Wiener measure $d\mathbf{W}$ serves as a mathematical model for the stochastic particle motion due to temperature fluctuations. The strength of Brownian motion is directly proportional to the square root of the Boltzmann constant k_{B}, the temperature T and the friction coefficient γ. As the strength of Brownian motion is inversely proportional to the particle mass, it primarily influences small particles. The last term in the Lagrangian formulation $\mathbf{f}(\mathbf{x},t)$ models additional external forces.

2.3.3 Electrostatic Fiber-Particle Interactions

Taking into account the electrostatic fiber-particle interactions in the Lagrangian equation requires a preceding calculation of the electrostatic field $\mathbf{E}(\mathbf{x}, t)$. Starting point for this calculation is a charge density ξ_{F} on the surface of filter fibers. By solving the Poisson equation

$$\Delta \Phi(\mathbf{x}, t) = -\frac{\xi_{\mathrm{F}}}{\epsilon_0} \int_{\partial G} \delta \quad \text{in } \Gamma \times [0, t_{\mathrm{end}}]\,, \tag{2.14}$$

i.e., by integrating over the fiber surface ∂G, the electrostatic potential Φ is derived. The permittivity of air is given by $\epsilon_0 = 8.854\,188 \cdot 10^{-12}\,\mathrm{A\,s\,m/V}$ and δ denotes the Dirac distribution. The electrostatic field is expressed by the negative gradient of the potential according to

$$\mathbf{E}(\mathbf{x}, t) = -\nabla \Phi(\mathbf{x}, t) \quad \text{in } \Gamma \times [0, t_{\mathrm{end}}]\,. \tag{2.15}$$

Finally, the resulting force $\mathbf{F}(\mathbf{x}, t)$ on a particle with the charge q and mass m is given by

$$\mathbf{F}(\mathbf{x}, t) = \frac{q\mathbf{E}(\mathbf{x}, t)}{m}. \tag{2.16}$$

2.3.4 Implementation in the Software Package GeoDict

The software package GeoDict [108] offers modular tools for the multi-scale simulation of materials and fluid flows in diverse applications. The designation GeoDict is composed of *GEO*metrical material designer and material property pre*DICT*or. Originally, the software package was developed to model the behavior of porous media and composite materials. For this purpose, GeoDict offers the possibility to virtually generate structures as well as to simulate multiphase flow physics in porous media. Hence, GeoDict is well-suited for simulating filtration procedures, composites, the oil and gas transport through digital rocks or electrochemical processes in fuel cell and battery media.

Simulating the separation efficiency of cabin air filter media with the software GeoDict demands four successive steps:

1. the generation of a digital filter structure,
2. the calculation of the air flow field through this filter structure,
3. the derivation of the electrostatic field from the surface charges, and
4. the simulation of the particle trajectories.

The implementation of the four individual steps in GeoDict is described below. Furthermore, the uni-directional coupling is explained.

Generation of the Filter Structure. GeoDict basically offers two methods for the creation of digital filter structures based on the provided 'ImportGeo' and 'FiberGeo' modules. With the first method, digital twins of real filter media can be obtained from x-Ray micro-computed tomography (xCT) scans. In order to convert the large series of two-dimensional images to a three-dimensional structure, the 'ImportGeo-Vol' interface is used. The module is based on a segmentation of gray values to extract filter fibers from the background. In addition, it provides tools for image processing in order to properly prepare the structure for further analysis.

A detailed characterization of the digitized filter media provides a deep insight into the microscale structure. Details about the fiber size distribution and orientation, gradients in packing density amongst others can be obtained.

With the second method, three-dimensional fiber objects are modeled mathematically. Statistical properties such as fiber parameters, packing density and thickness of filter media serve as input parameters to generate the structure. Thus, the method allows modifying individual parameters of the fibrous structure while leaving the rest untouched to a certain extent. The simulation of the respective impacts on filtration performance constitutes a great advantage over experimental testings [62]. Furthermore, 'FiberGeo' enables the generation of simplified structures such as the single fibers used in Chapter 4 or the wired weaves used in Chapter 6.

Hydrodynamics in GeoDict. Once the digital structure is generated, the actual simulation is started using the 'FilterDict' module [110]. In order to solve the flow Eqs. (2.7) before, inside and after filter media, GeoDict uses an equidistant

voxel mesh discretization. Since a stationary flow field is assumed in GeoDict, the time derivatives of the (Navier-) Stokes equations are neglected. The following three methods are implemented in GeoDict to iteratively solve the PDEs [65].

The **Explicit Jump (EJ)** immersed interface method is based on a finite difference method on a regular grid [109]. The solver is limited to Stokes flow and is especially suitable for the simulation of highly porous media.

The **SIMPLE-FFT** is an enhancement of the semi-implicit methods for pressure linked equations (SIMPLE) which uses a Fast Fourier transformation (FFT) as a fast solver for the pressure Poisson equation. The solver can be used to aquire a solution of the Stokes equations as well as the Navier-Stokes equations. By contrast to the EJ solver, the SIMPLE-FFT converges very fast for very dense filter structures.

The **LIR (Left Identity Right)** solver uses a combination of Octrees and KD-trees for spatial partitioning. The mathematical structure of the LIR tree is based on the set of three symbols $A = \{L, I, R\}$. The LIR solver enables a local grid refinement in areas where the velocity or pressure gradient is high [65].

Due to its short computational runtime through the adaptivity and at the same time low memory requirements for porous media, only the LIR solver is deployed in this work.

Electrostatics in GeoDict. In the software GeoDict, the assigned surface charge density ξ_F is divided between the two adjacent voxels to the fiber surface. Subsequently, the electrostatic potential and the electrostatic field are calculated according to Eq. (2.14) and Eq. (2.15). Periodic boundary conditions are specified for the potential Φ perpendicular to the direction of flow. At the inlet and outlet position in flow direction, zero Dirichlet boundary conditions are applied. These specifications lead to the fact that the constant component of the calulated potential depends on the inflow and outflow length. However, since the shape of the function remains the same, the electrostatic field, i.e., the gradient of the potential, is independent of the position of the zero Dirichlet boundaries [110].

Particle Tracking in GeoDict. By means of the given fluid flow and electrostatic fields the particle trajectories through the filter media can be calculated in the next step according to the equation of motion (Eq. 2.10). This particle tracking is also part of the 'FilterDict' module in GeoDict: A batch of particles is added to the inflow area. Since particles do not interact with each other, particle concentration only influences the intensity of fluctuations in the filtration efficiency. In order to make a precise statement about whether a particle with a certain diameter is collected or not, the particle trajectories of as many starting positions as possible must be considered. During particle tracking, GeoDict permanently searches for collisions of particles with the filter medium. The ratio between the number of captured particles and the number of added particles provides the filtration efficiency according to Eq. (2.3).

Coupled Simulation in GeoDict. By neglecting particle-particle interactions and the retroactive effect of the particle movement on the flow field, the uni-directional coupling method allows to calculate the individual components consecutively in separate steps. Both, the flow field and the electrostatic field are calculated in preceding steps and exported. The fields are subsequently read in again to calculate the particle trajectories.

For the simulation of a filter lifetime with GeoDict, the fiber structure is extended by the collected particles at regular intervals. Based on the updated geometry, a new flow field and a new electrostatic field are calculated and, subsequently, the next batch of particles is tracked and so forth. In this work, however, only initial collection efficiencies are simulated.

2.4 Literature Review

This literature review summarizes previous pioneering research studies – both experimentally and numerically – on electrostatically charged filter media and presents the current state of science. The focus lies on simulation studies and the respective methods applied. A common approach in the field of air filtration, which is also used in this thesis, is the analysis on the basis of single fibers. The single fiber model reflects the essential filtration effects and is ideal for gaining a deeper understanding of underlying physical processes. Relevant publications about

single fiber analysis are collected in Sec. 2.4.1. Since the accurate representation of mechanical collection mechanisms is the basis for the simulation of a realistic particle behavior, the section also refers to conventional non-charged systems.

Transferring the findings from the single fiber analysis to complex filter media poses a major challenge. Due to limited compute power, the respective simulation analyses are mostly based on simplifications. The most important milestones with regard to the simulation of particle separation on realistic fibrous structures are presented in Sec. 2.4.2. Again, a distinction is made between purely mechanical collection and additional electrostatic separation mechanisms.

2.4.1 Single Fiber Analysis

As shown in Fig. 2.2 and Fig. 2.4, the predominant mechanisms in air filtration are based on particle separation on individual filter fibers (and not on sieving effects as in liquid filtration). Therefore, the filtration analysis based on single fibers is often very informative and has been a common approach for several decades. Relevant publications mainly deal with understanding two challenging processes that depend on each other: Firstly, the initial particle deposition on a clean filter fiber through mechanical and electrostatic separation mechanisms and secondly, the influence of deposited particles on further loading kinetics. Since the morphology of deposited particles on the fiber surface influences the subsequent flow and, thus, the entire filtration process, the investigation of accumulated particles on individual fibers is of great importance. Furthermore, the arrangement of deposited particles directly affects the pressure drop, which is one of the three key performance indicators as shown in Fig. 2.1. Previous simulation studies on both respective subjects are presented below, subdivided into mechanical and electrostatic separation. Beforehand, the most important findings from experimental analysis are presented briefly in each case, but the key focus is on numerical investigations.

Mechanical Collection on Single Fibers. The initial collection efficiency of single fibers due to mechanical mechanisms has been experimentally investigated by many researchers [30, 40, 70, 80, 82, 92, 96]. Kasper et al. [50] provided an overview of the resulting empirical fit functions obtained for different Stokes and Reynolds numbers in the inertia and interception regime. Particle deposition on

conventional, i.e., non-charged, filter fibers were experimentally observed to result in the formation of chain-like dendrites, which were mainly formed in the upstream direction [14, 22, 48]. Myojo et al. [72] expressed the ratio of the collection efficiency of a dust-loaded fiber to the collection efficiency of a clean fiber by a linear function of the mass load of deposited particles. However, reliable analytical expressions of the mechanical collection efficiency are lacking. This is why precise simulations of the underlying physics are required. The simulation approaches developed and used so far as well as the corresponding outcomes achieved are presented below.

The Kuwabara cell method [54] is frequently applied to express the fluid stream lines around circular cylinders. Kanaoka et al. [48] additionally used a Monte Carlo simulation technique to investigate the three-dimensional growing process of particle dendrites based on the Kuwabara flow. They obtained fairly good agreement with experimental observations when comparing the resulting dendrite shapes. Furthermore, the authors derived a linear correlation between the collection efficiency and the deposited mass, which was later experimentally confirmed by Myojo et al. [72] as already mentioned above.

Due to the formation of the dendrite structure, the boundary conditions for the flow field continuously alter during particle loading. The Lattice-Boltzmann method enables a dynamic adaptation of the boundary conditions to the complex surface and, thus, is well suited for the simulation of the background flow field. Filippova and Hänel [33] used a Lagrangian approach to track the particles in the three-dimensional Lattice-Boltzmann flow field. Without any retroactive influence of the particle dendrites on the flow pattern, they were able to reconfirm the linear correlation between the collection efficiency and the dust load as proposed by Kanaoka et al. [48]. By taking the feedback of dendrites on the flow field into account, however, a constant mechanical collection efficiency was achieved after some loading time.

Przekop et al. [79] also took advantage of the possibility to dynamically adapt the boundary conditions with the Lattice-Boltzmann method. In their two-dimensional simulation studies, they analyzed the influence of the Péclet number, which defines the ratio between advective and diffusive particle transport, on the shape of deposited particles. For the diffusion dominant flow regime, they observed intensively branched deposited particle clusters. A higher contribution of convection, i.e.,

higher Péclet numbers, resulted in narrow and more regularly shaped dendrites, which were mainly located upstream the fiber. Later on, the authors extended their method to three dimensions and investigated the mechanical particle deposition on a mixture of individual nanofibers and microfibers [78].

Wang et al. [104] developed a new Lattice-Boltzmann method to simulate the two-phase flow of fluid and particles. For fluid dynamics, they used the classical Lattice-Boltzmann method, whereas the transport of solid particles was handled by a cellular probabilistic approach. Hence, the simulated particle concentrations were constrained to move only on the same regular nodes as the fluid populations and their motion probabilities to neighboring nodes were calculated. The characteristics of real particles such as their positions or velocities can be derived from summing all fictive simulation particles and taking a weighting factor into account. Using the proposed method for simulating clean and dust-loaded fibers led to good agreement with previous theoretical predictions and experimental observations.

A different simulation approach was used in the single fiber analysis by Lehmann [61], who extended the commercial software tool ANSYS Fluent via so-called user defined functions. The particle trajectories were calculated with the discrete phase model (DPM). In his three-dimensional simulation studies, the feedback of deposited particles to the flow pattern as well as the adhesion and rebound of particles according to the theory of Hiller [41] were taken into account. The simulation of single fiber loading kinetics showed the same trends and reconfirmed previous [33, 48] insights.

Especially in the regime dominated by inertia and interception, an accurate flow field is the basis for the resulting particle trajectories and, thus, for the collision efficiency. Müller et al. [71] also used the commercial CFD software ANSYS Fluent to simulate the air flow pattern around a single fiber in a periodic row. They validated the flow field simulated for low and moderate Reynolds numbers for numerous parameter sets using an analytical approximation proposed by Miyagi [69]. Based on this flow field, particle trajectories were obtained by solving the equation of motion. The collision efficiency with single fibers in a periodic row was finally calculated based on the limiting trajectory as proposed by Brown [19]. Furthermore, a valid fit function for a broad parameter range was derived from the simulation results.

The good agreement of numerous simulation results with experimental observations demonstrates the good understanding of the theory behind mechanical particle collection on individual fibers.

Electrostatic Separation on Single Fibers. Compared to the analysis of mechanical collection mechanisms, less experimental data are available for the electrostatic separation on single fibers. However, theoretical expressions exist to describe the separation efficiency based on individual electrostatic mechanisms, i.e., Coulomb attraction, induced dipoles and mirror charges [17, 57, 74]. In order to predict the overall filtration performance, the efficiencies due to individual mechanical and electrostatic separation mechanisms are usually summed up. However, since the electrostatic mechanisms interfere, this approach is doubtful and simulation studies combining all effects simultaneously are required.

Baumgartner and Löffler [11] followed the stochastic model approach based on Kuwabara flow as proposed by Kanaoka et al. [48]. For the single electret fiber analysis, they used monodisperse particles which were charged at Boltzmann equilibrium. The respective two-dimensional simulation of loading kinetics led to a uniform spatial distribution of small particles deposited on the fiber surface. When taking fiber neutralization by deposited charged particles into account, the formation of small dendrites was observed. Moreover, the authors extended their simulation approach to three dimensions and additionally analyzed the influence of polydisperse particles [9]. They concluded that the separation of several large particles leads to a more random overall particle deposition compared to the case of monodisperse particles.

Besides the exploration of loading kinetics, Baumgartner et al. [10] also pursued another approach to gain a better understanding of the motion of charged particles. With a high-speed camera, the authors recorded particle trajectories in the vicinity of a single fiber with a bipolar electric charge. They superimposed the particle trajectories resulting from their two-dimensional simulation with the experimentally determined paths. They fitted the fiber charge in their model such that the simulated trajectories match the measurement results.

Walsh and Stenhouse [99] built on the work from Baumgartner and Löffler [11] and additionally considered the polarization force on neutral particles. The

authors also concluded that the particles settle more uniformly around the fiber when electrostatic separation effects are taken into account. Based on this result, they predicted a higher dust holding capacity for electrostatically charged filters compared to conventional ones.

Kanaoka et al. [47] expanded their three-dimensional simulation method for the mechanical particle collection [48] to electret fibers. They analyzed the dendrite growing for uncharged as well as identically charged monodisperse particles at a bipolarly charged fiber. Charged particles resulted in the formation of taller dendrites in a more limited area of the fiber surface, i.e., the area of opposite polarity to the particles, compared to non-charged particles, which were captured by polarization effects. In addition, the dipole rotation with respect to the flow direction significantly affected the spatial distribution of deposited particles. A good agreement with their experimental observations was observed for both, uncharged and charged particles. The three-dimensional stochastic model for cylindrical electret fibers with induced dipole and Coulomb forces was later enhanced by including Brownian motion by Tanthapanichakoon et al. [97]. For weak electrostatic forces, loading kinetics could still be approximated by the linear function proposed for mechanical collection [33, 48, 72]. In the case of higher charges, two different linear functions were required to describe the particle collection at low dust load and at high dust load.

Also based on Kuwabara flow, Oh et al. [73] included force terms for Coulomb, polarization and mirror charge effects to the simulation. The statements that electrostatic effects favor uniform particle deposition on the fiber surface was confirmed. This observation applied to both, small ($d_\mathrm{P} = 0.1\,\mu\mathrm{m}$) and large ($d_\mathrm{P} = 0.5\,\mu\mathrm{m}$) monodisperse particles.

Wei et al. [107] also studied the influence of Coulomb forces and dielectrophoresis using the stochastic simulation approach. The deposition of particles larger than $d_\mathrm{P} = 0.5\,\mu\mathrm{m}$ were mainly subjected to a polarization force (in addition to impaction and interception), whereas Coulomb forces were prevailing when the particle size decreases.

The simulation models for the mechanical collection of single fibers based on the Lattice-Boltzmann method [33] were also supplemented with electrostatic

separation mechanisms. Lantermann and Hänel [56] solved the Laplace equation for the electrostatic potential and revealed an essential effect of recalculating the electrostatic field when charged particles deposit on the fiber.

The uniform particle distribution observed in many research studies is supposed to delay the clogging of pore spaces and, thus, to ensure a lower increase in the pressure drop compared to conventional uncharged filter media. Furthermore, it has been shown that mechanical and electrostatic effects are effective simultaneously [49] and that the interference has to be considered in simulation studies. However, all presented research studies focus on weakly charged submicron particles such as sodium chloride or stearic acid particles. The filtration behavior of coarser particles carrying significantly more elementary charges due to their larger surface area is practically unknown.

2.4.2 Complex Filter Structure Analysis

Analytically transferring single fiber theories to realistic complex filter structures is quite challenging as further influencing factors need to be considered. For instance, different fiber orientations and the resulting shape of the pores play a role. Furthermore, the interference of electrostatic fields induced by adjacent fibers must be taken into account. The required compute power additionally increases dramatically compared to the simulation of individual fibers.

Mechanical Collection on Complex Filter Structures. As the introduction to the status quo simulation approach in Sec. 2.3 indicates, the simulation of filtration processes in GeoDict is already well advanced. In contrast to the above-mentioned research studies, where single fiber experiments are analyzed, GeoDict allows simulating whole filter media segments over their complete thickness. The software tool originated from the Fraunhofer Institute for Industrial Mathematics (ITWM) in Kaiserslautern in 2001. Since the foundation of Math2Market as a spin-off in 2011, GeoDict has been developed and marketed by this company.

Early publications in the field of filtration processes already provided the algorithms for a stochastic geometry generation [58] and the import and image processing of xCT data of real filter media [59]. This enabled the investigation of the influence of individual structural parameters such as fiber orientation, fiber

diameter distribution, shape of the fibers or the packing density profile. Latz and Wiegmann [59] already included the proposed methods in the software GeoDict and the corresponding FilterDict module also used in this work. However, the underlying solver was previously based on the Lattice-Boltzmann method. Later on, they switched to solving the Navier-Stokes equations by means of the finite differences method [83, 84]. The simulation of the standard test in oil filtration, i.e, the multi pass test, was proposed by Becker et al. [13]. They also extended their software to model the cake formation after the clogging point of the filter medium is reached [12].

The software GeoDict can also be extended via so-called user-defined functions, which was exploited by Lehmann et al. [63]. They enhanced the implemented modeling of particle capturing and included particle re-entrainment based on models proposed by Banzhaf [6]. For the oil multi pass test simulation of three-dimensional fibrous structures, they were able to predict loading kinetics and achieved results comparable to experiments. Moreover, Lehmann et al. [62] proposed a method for virtual filter media development in three steps: The starting point is the real filter medium, which is characterized in the first step. Based on determined structural parameters a virtual clone is generated as a parametric model of the three-dimensional filter medium. In the third and final step, the virtual clone is optimized by parameter modifications. A challenge with this method is that validation is often based on macroscopic quantities. In addition, the image processing step has a sensitive effect on the resulting simulated filtration behavior.

In conclusion, all necessary models to simulate the mechanical collection of particles in non-charged systems have been implemented.

Electrostatic Separation on Complex Filter Structures. Experimental investigations proved that electret filters lead to a significantly higher filtration efficiency compared to conventional filters with similar pressure drop [8, 11, 100, 101, 102]. However, the experiments also revealed that (particularly small) deposited particles neutralize the filter fibers. This reduces the separation performance during particle loading. Large particles, by contrast, block the pores and provoke improved mechanical particle collection. The process of fiber neutralization and of the resulting temporary efficiency minimum is not yet sufficiently understood.

Therefore, simulation studies aim to provide more information.

Wiegmann et al. [110] presented the inclusion of electrostatic fiber-particle interactions in the software GeoDict. The respective implementations are already described above, where the fundamentals of this status quo simulation approach were introduced in Sec. 2.3.3. Significantly more particles were separated by the simulation of an electrostatically charged example structure compared to conventional, uncharged fibers [85]. However, the authors also pointed out that the surface charges of the fibers and the particles are not known.

Schmidt et al. [89] followed a similar simulation approach and developed their own direct numerical simulation code called DNSlab. As in the software GeoDict, they also solve the steady-state Navier-Stokes equations based on a voxel discretization. For the electrostatic field, they applied different boundary conditions than Wiegmann et al. [110] such that the Poisson Eq. (2.14) had a non-zero right-hand side only at the flow boundaries and $\Delta\Phi = 0$ was assumed inside the flow domain [94]. In addition to the simulation, Hellmann et al. [38] used an empirical formula and experimental measurements to determine the filtration efficiency of an electrostatically charged medium. Whereas the empirical formula did not lead to adequate results for charged fibers, the three-dimensional model allowed a good fit with the measured separation efficiency. Additionally, Kerner et al. [51] included the generation of bipolar surface charge distributions in the software DNSlab. The simulation results for submicron sodium chloride particles with charges between $q = -2\,e$ and $q = +2\,e$ reproduced the measurement results very well.

In comparison with experimental measurements, simulation studies offer the advantage of full insight into the filtration process. Information about when and where particles are deposited in the fibrous microstructure can be obtained. However, there are still many open issues to numerically reproduce and predict the behavior of electrostatically charged filters. For example, the neutralization of the fibrous filter structure by separated charged particles is not considered so far. Analogous to single fiber analyses, the simulation studies concentrate on weakly charged sodium chloride particles. The behavior of highly charged dust particles with a potentially bipolar charge distribution was not referred to so far.

2.5 Summary & Research Issue

Cabin air filters convince by their high separation efficiency, low pressure drop, and a high dust holding capacity at the same time. The electrostatically charged fibrous filter material is responsible for these favorable performance factors. Different electrostatic separation mechanisms are effective in addition to the conventional mechanical particle collection. In order to simulate the separation of airborne particles by filter media and to calculate the resulting filtration performance, the uni-directionally coupled modeling approach implemented in the software GeoDict represents the status quo. However, the software package is incomplete with respect to this simulation of electrostatic separation mechanisms due to their high complexity.

A proven approach in air filtration is the basic analysis of the separation behavior by means of single fibers. The detailed literature review revealed that the simulation of mechanical collection mechanisms and of the resulting loading kinetics on this simplified filter structure is already very sophisticated. By contrast, the simulation of the various electrostatic separation mechanisms is stated to be more complex and is, therefore, mostly based on theoretical expressions.

Applying the gained theories based on single fibers to realistic filter media is deemed to be very challenging as further effects occur. For instance, different fiber orientations, packing density profiles or the interference of electrostatic fields induced by adjacent charged fibers must additionally be considered for real filter media. Furthermore, an analysis at this level of detail known from single fibers is not possible due to limited compute power and, thus, makes simplifications necessary. The overarching research issue to be answered in this thesis is primarily aiming at the simplifications and is specified as:

Which models for the microstructure simulation of fibrous structures are necessary to simulate cabin air filter media with regard to electrostatic charges?

This can be broken down to three more specific central research questions that are elaborated and specified below. Although test dust particles often carry a high amount of bipolar electrostatic charges, the interaction between individual particles during their movement in the flow field is commonly neglected in simulation studies.

This results in the formulation of the first research question:

How does electrostatic dust agglomeration caused by particle-particle interactions affect the filtration performance?

Previous investigations focused on the simulation of particles in a Boltzmann equilibrium or weakly charged sodium chloride particles. For these specific aerosols and at the same time low particle concentrations, the uni-directionally coupled modeling of the status quo simulation approach was assumed to be sufficient. In this thesis, the following second and more scientific research question is addressed:

To what extent does the accuracy of the simulated particle behavior depend on the coupling intensity between the individual components, i.e., electrostatically charged solid particles and the fluid flow field?

In addition, further potential filtration effects resulting from the highly charged dust particles are to be identified and quantified. The third research question that arises from the intensity of different electrostatic filtration effects is:

Which further electrostatic mechanisms need to be implemented in order to reliably predict the filtration performance of real cabin air filter media?

In order to fill major gaps in research, these three research issues are examined in detail in this thesis. The modeling of previously unaddressed electrostatic filtration effects aims to broaden the knowledge base on cabin air filters.

Chapter 3

Enhanced Fully-Coupled Modeling of Air Filtration Processes

Simulating particle dynamics in the test channel of air filter media requires the mathematical description of the underlying physical processes. Due to the high degree of complexity, however, the mathematical model cannot reflect the exact representation of real test dust. Therefore, the modeling is based on some general, simplifying assumptions such as treating particles as solid spheres instead of considering diverse particle shapes, and tracking only their mass centers instead of their full motion including rotation. The status quo modeling approach described in Sec. 2.3 furthermore assumes that particles neither influence the pattern of the background fluid flow nor interact with each other. This is where the fundamentally new fully-coupled modeling approach comes into play. The novel simulation approach models interactions between single molecules or particles based on a molecular dynamics (MD) like method and includes the full transient interaction between the background flow field and particles.

The sophisticated simulation of the particulate flow requires modeling and integrating three individual components: short-range MD potentials to model particle collisions, long-range electrostatic interactions and the background flow field. For the latter, the Lattice-Boltzmann method (LBM) is used to approximate the Navier-Stokes equations (Eq. (2.7)). The principles of both simulation methods,

i.e., LBM and MD, are described in detail in Sec. 3.1 and Sec. 3.2.

A focal point of this modeling chapter is to combine appropriate molecular dynamics potentials in order to properly model the behavior of aerosol particles. This involves modeling electrostatic interactions as well as the formation of agglomerates through particle collisions. To properly simulate the motion of aerosol particles, moreover, the choice of appropriate input parameters and boundary conditions is of major importance. Particularly the particle size distribution as well as the unknown particle charge distribution represent important influencing factors. Since different input parameters and boundary conditions are applied for different simulation experiments, however, this information is provided specifically in the respective result chapters.

Section 3.3 covers the implementation of the individual components in the software package ESPResSo used in this work. In addition, the bi-directional coupling method between particles and the background flow field is presented in Sec. 3.4. Figure 3.1 schematically illustrates the full coupling between MD particles and the LBM based air flow.

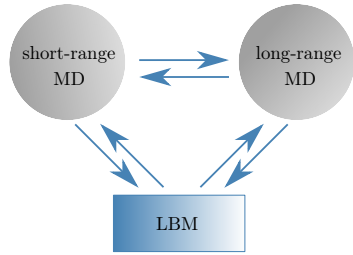

Figure 3.1: Schematic illustration of the fully-coupled modeling approach. The short-range and long-range interactions between MD particles and their coupling to the fluid flow field calculated with the LBM are displayed. Fiber-particle interactions are also modeled using short-range and long-range MD potentials in this work.

In addition to the interaction between particles and the fluid, the simulation of filtration processes requires modeling the interaction with the filter medium. Section 3.2.2 introduces a devised method for modeling particle separation on filter fibers based on short- and long-range MD.

3.1 The Lattice-Boltzmann Method

The Lattice-Boltzmann method incorporates the fact that a fluid consists of microscopic particles. Fluid movement in the LBM is based on the transport of particle distributions. The established probability density function $f(\mathbf{x}, \mathbf{p}, t)$ indicates the probability of (virtual) particles at the position $\mathbf{x}$ with the momentum $\mathbf{p}$ at time t. Temporal evolution of the stochastic particle distribution in the simulation domain $\Gamma \in \mathbb{R}^3$ for the time period $t \in [0, t_{\text{end}}]$ is modeled with the Boltzmann equation given by

$$\frac{df\,(\mathbf{x}, \mathbf{p}, t)}{dt} = \Omega\,(f)\,, \tag{3.1}$$

where Ω is a so-called collision operator.

In order to make the Boltzmann equation solvable, the LBM discretizes the velocity space with a finite number of discrete velocities $\mathbf{c}_i$ and finite differences on a cubic grid in the three-dimensional coordinate space. The discrete velocities are chosen in such a way that they transport particles from one lattice node to one of its neighbors within one time step. Figure 3.2 shows the widely used D3Q19 discretization for velocities with 19 components associated to the center of a three-dimensional cubic grid cell. The individual velocity components connect the node with itself (blue dot), the six face (green arrows) and twelve edge (red arrows) neighbors.

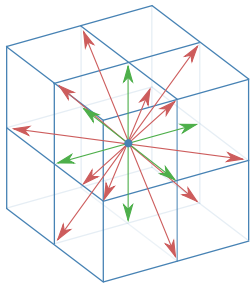

Figure 3.2: The velocity vectors $\mathbf{c}_i$ for a D3Q19 lattice connect the central grid point to its six face (green) and twelve edge (red) neighbors. The 19^{th} velocity vector is the rest mode (zero velocity) marked as a blue dot. The image is adapted from Schiller [88].

The interaction between the particles in the simulation domain $\Gamma \in \mathbb{R}^3$ for the time period $t \in [0, t_{\text{end}}]$ is modeled with the Lattice-Boltzmann equation according to

$$\underbrace{f_i\left(\mathbf{x} + \mathbf{c_i} dt, t + dt\right) - f_i\left(\mathbf{x}, t\right)}_{\text{streaming}} = \underbrace{-\frac{dt}{\tau}\left(f_i\left(\mathbf{x}, t\right) - f_i^{eq}\left(\mathbf{x}, t\right) + F_i(\mathbf{x}, t)\right)}_{\text{collision}} =: \Omega_i(f_i(\mathbf{x}, t)). \tag{3.2}$$

During their movements particles exchange momentum and energy through streaming and collisions with other particles. For the complex collision operator Ω_i, which describes a two-body collision, several simplified models are available, e.g., the Bhatnagar-Gross-Krook (BGK) model [67] used in this work.

The two steps of the LBM algorithm, i.e., streaming (modeling convection) and collision, are illustrated in Fig. 3.3. For better overview, the two-dimensional D2Q9 lattice is used.

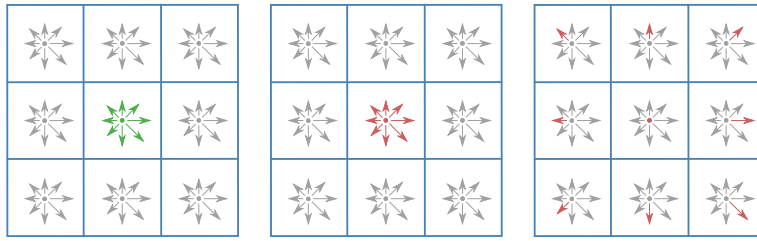

(a) initial state (b) after collision (c) after streaming

Figure 3.3: Schematic illustration of the two-step LBM algorithm consisting of the streaming and the collision step. The arrows indicate the particle populations f_i with their respective grid velocities in the two-dimensional D2Q9 lattice. The sketch on the left-hand side shows the initial state (a) of populations before executing an integration step. The discrete velocities marked in green are located in the cell under consideration. After the collision step (b), a modified population f_i occurs. Subsequently, this population is streamed to the neighboring cells as shown on the right-hand side (c).

Expansions by Chapman show that the Lattice-Boltzmann equation segues into the Navier-Stokes equations for small Mach numbers [28]. Hence, the Lattice-Boltzmann equation presents a mesoscopic model, which is situated between the microscopic description of individual particles and a macroscopic observation.

3.2 Molecular Dynamics for Particle-Particle and Fiber-Particle Interactions

As already mentioned, calculating the interaction between individual particles is based on a molecular dynamics (MD) like approach. Instead of single molecules, coarse-grained dust particles are simulated in this work. The basis of particle-particle interactions is the potential energy $U(\|\mathbf{r}\|)$ induced by each pair of particles. This potential energy depends on the distance $\|\mathbf{r}\|$ between two interacting particles. Depending on the radius in which a potential energy is effective, a distinction is made between short-range and long-range potentials. In this thesis, two short-range potentials, i.e., the Hertzian and the harmonic bond potential, and the long-range electrostatic potential are applied to model the behavior of dust particles. The focus of Sec. 3.2.1 is on short-range interactions of a particle at position $\mathbf{x}_i$ resulting from the interaction with a second particle at position $\mathbf{x}_j$. The long-range interactions are tackled in Sec. 3.2.3. This appropriate combination of MD potentials has already been published prior to this thesis [91].

The accelerating force $\mathbf{F}(\mathbf{x}_i, \mathbf{x}_j)$ on the particle of interest results from the principle of minimizing its potential energy according to

$$\mathbf{F}(\mathbf{x}_i, \mathbf{x}_j) = -\nabla_{\mathbf{x}_i} U(\|\mathbf{r}\|) \quad \text{with} \quad \mathbf{r} = \mathbf{x}_i - \mathbf{x}_j. \tag{3.3}$$

The equation of motion

$$\ddot{\mathbf{x}}_i = \frac{\mathbf{F}(\mathbf{x}_i, \mathbf{x}_j)}{m} \tag{3.4}$$

describes the resulting particle transport.

The total force acting on particle i is obtained by summing up the forces with all interaction partners.

$$\mathbf{F}_i = \sum_{j \neq i} \mathbf{F}(\mathbf{x}_i, \mathbf{x}_j) \tag{3.5}$$

3.2.1 Particle Collisions

Short-range MD is used in the fully-coupled model to represent particle-particle (and fiber-particle) collisions. Such collisions primarily occur due to electrostatic attraction, but also due to relative movements based on the flow pattern. The best-known potential to model particle contacts in classical molecular dynamics is the Lennard-Jones (LJ) potential. However, this LJ potential models the short-range interaction of molecules or atoms based on their positive atomic nucleus and the negative electron shell. In contrast, a more elastic collision is assumed for dust particles. For that, different potentials have to be used for the simulation of airborne particles. Through the mutual exertion of forces on each other, the respective particles change their state of motion during collision and possibly also their shape. In order to model the impact of two dust particles, an elastic collision is combined with an adhesive contact. In addition, a dynamic bonding mechanism prevents particles from sliding around each other after coming into contact. All required interactions for the simulation of dust particles are included in the wide range of the potentials provided by the software package ESPResSo [64]. The applied models are presented in detail below.

Elastic collision. In order to model the elastic collision of dust particles, the purely repulsive Hertzian [76] potential

$$U_{\mathrm{Hz}}\left(\|\mathbf{r}\|\right) = \begin{cases} \epsilon\left(1 - \frac{\|\mathbf{r}\|}{\sigma}\right)^{\frac{5}{2}} & \text{for } \|\mathbf{r}\| \leq \sigma, \\ 0 & \text{for } \|\mathbf{r}\| > \sigma \end{cases} \tag{3.6}$$

is employed. The variable σ is defined as the sum of both radii of the involved particles (see Fig. 3.5) and ϵ is the associated interaction strength. The Hertzian potential becomes effective as soon as two particles touch each other at $\|\mathbf{r}\| = \sigma$ and increases with further approach. The left-hand side of Fig. 3.4 shows the resulting curve for the potential U_{Hz} as well as the absolute value of the force $\mathbf{F}_{\mathrm{Hz}}$ as a function of the distance $\|\mathbf{r}\|$ between the particle centers. The model describes the interaction of weakly deformable spheres and prevents colliding particles from overlapping [68]. Therefore, it is a simple representation of a soft sphere interaction which remains finite at $\|\mathbf{r}\| = 0$.

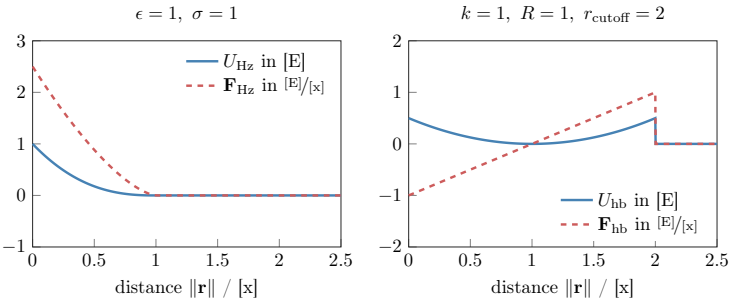

Figure 3.4: The Hertzian (left) potential models an elastic collision between two particles. The harmonic bond potential (right) is responsible for the fact that colliding particles adhere to each other. In addition to the potentials, the respective forces are plotted over the distance $\|\mathbf{r}\|$ between the particle centers.

Adhesive contact. Due to the rough surfaces of dust particles, high frictional forces are assumed to arise during contact and lead to adhesion of the colliding particles. This mechanical connection by interlocking of the respective particles is modeled by the harmonic bond potential

$$U_{\mathrm{hb}}\left(\|\mathbf{r}\|\right) = \begin{cases} \frac{1}{2}k\left(\|\mathbf{r}\| - R\right)^2 & \text{for } \|\mathbf{r}\| \leq r_{\mathrm{cutoff}}, \\ 0 & \text{for } \|\mathbf{r}\| > r_{\mathrm{cutoff}}. \end{cases} \tag{3.7}$$

The symmetric interaction modeled after Hooke's law is directly proportional to the spring constant k as well as to the square of the difference between the distance $\|\mathbf{r}\|$ and the equilibrium length R. The harmonic bond potential becomes effective at the distance $\|\mathbf{r}\| = R$ and acts repulsively at closer approach of the particles as can be seen on the right-hand side of Fig. 3.4. When the rejection of the particles leads to a distance of $\|\mathbf{r}\| > R$ again, they sense an attractive potential that holds the particles together. A solely acting harmonic potential would lead to a harmonic oscillation of the two particles around the equilibrium length R. Optionally, the bond can be reported as broken, whenever the harmonic bond gets larger than a defined cutoff radius r_{cutoff}.

Dynamic bonding. During the simulation, ESPResSo permanently searches for particle collisions. The creation of a bond and, thus, the formation of an agglomerate occurs when the distance between two particles is smaller than the sum of both radii $\sigma < \mathrm{r}_1 + \mathrm{r}_2$. Whenever particles collide, the harmonic bond potential additionally becomes effective. ESPResSo provides various mechanisms for the bonding process. In the simplest case, the harmonic bond potential acts between the centers of two colliding particles as illustrated on the left-hand side of Fig. 3.5.

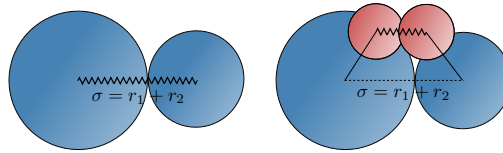

Figure 3.5: Simple bonding mechanism with a harmonic bond potential acting between particle centers (left) and introduction of virtual sites marked in red to fix the particles at the point of collision (right). In the latter case, the harmonic bond potential is effective between the virtual sites, which are in turn rigidly connected to the respective real particle. The virtual particles are generated on the connecting line of the real particles, but shifted in the illustration for visualization purposes.

In this arrangement, the particles can still rotate around each other. For dust particles, however, it is assumed that they directly entangle at their point of impact. To model this characteristic, two so-called virtual sites are introduced in each collision. As shown on the right-hand side of Fig. 3.5, these virtual particles are rigidly connected to their respective real particles. In addition to this rigid connection, the harmonic bond potential acts between the virtual particles as illustrated by the schematic spring. In order to use the same equilibrium length $R = 0$ of the harmonic bond potential for arbitrary combined particle sizes, the virtual sites are placed directly on top of each other. In Fig. 3.5, the virtual particles are shifted for visualization purposes only. Therefore, the mechanism enables the adhesive collision of polydisperse particles. When the particles carry bipolar electrostatic charges – as assumed for dust particles – the described dynamic collision detection is particularly important as collisions are supposed to occur very frequently.

3.2.2 Particle Deposition on Filter Fibers

To apply the fully-coupled modeling approach to the simulation of filtration processes, the deposition of aerosol particles on filter fibers must be modeled. For this purpose, the cylindrical fibers are filled with fixed auxiliary particles of the same diameter $d_P = d_F$. As illustrated in Fig. 3.6, these particles strongly overlap to represent the geometry of the fiber adequately. The auxiliary particles enable the accumulation of moving aerosol particles.

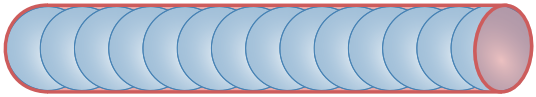

Figure 3.6: The cylindrical fiber (red) filled with fixed auxiliary particles (blue) forms the basis of modeling the particle deposition.

Between the moving dust particles and the auxiliary particles the same short-range MD potentials, i.e., Hertzian potential and harmonic bond potential, are applied as for standard particle-particle interactions. This way, particles deposit on filter fibers at their point of collision. Since the number of MD particles significantly increases through this approach, there is a threshold between an optimal fiber representation and a minimal simulation runtime.

As boundary conditions for the fluid flow, an additional constraint, i.e., an exact cylinder or imported voxel structure, is used to represent the fiber.

3.2.3 Electrostatic Particle-Particle and Fiber-Particle Interactions

The high amount of bipolar charges on filter test dust is expected to lead to a mutual electrostatic interaction between the respective particles. This interaction of two point charges q_1 and q_2 is mathematically defined by the Coulomb potential

$$U_C\left(\|\mathbf{r}\|\right) = C\frac{q_1 q_2}{\|\mathbf{r}\|}. \tag{3.8}$$

The potential $U_C(\|\mathbf{r}\|)$ is inversely proportional to the distance $\|\mathbf{r}\|$ between the respective point charges. The prefactor

$$C = \frac{1}{4\pi\epsilon_0\epsilon_r} \tag{3.9}$$

contains the vacuum permittivity ϵ_0 and the relative permittivity ϵ_r of the respective medium. Since the electrical polarizability of air is very low ($\epsilon_r = 1.00059$), the difference in permittivity between vacuum and air can often be considered negligible.

The Coulomb energy is physically balanced by the thermal fluctuation energy $E_{\text{th}} = k_{\text{B}}T$ with the Boltzmann constant k_{B} and the temperature T. The distance at which the electrostatic energy of two charges becomes comparable to E_{th} is defined by the Bjerrum length

$$l_{\text{B}} = \frac{e^2}{4\pi\epsilon_0\epsilon_r k_B T}, \tag{3.10}$$

where $e \approx 1.602 \cdot 10^{-19}\,\text{C}$ denotes the elementary charge. For air at room temperature, the Bjerrum length is $l_{\text{B}} = 58\,\text{nm}$ [15].

Based on the Bjerrum length, the prefactor C becomes

$$C = l_{\text{B}} k_{\text{B}} T. \tag{3.11}$$

Applying Eq. (3.3) to the Coulomb potential leads to an inverse-square law for the resulting Coulomb force $\mathbf{F}_C(\mathbf{x}_i, \mathbf{x}_j)$ according to

$$\mathbf{F}_C(\mathbf{x}_i, \mathbf{x}_j) = l_{\text{B}} k_{\text{B}} T \frac{q_1 q_2}{\|\mathbf{r}\|^3}(\mathbf{x}_i - \mathbf{x}_j) \quad \text{with} \quad \mathbf{r} = \mathbf{x}_i - \mathbf{x}_j. \tag{3.12}$$

Figure 3.7 shows the characteristic curve of the Coulomb potential as well as the resulting force value as a function of the charge distance $\|\mathbf{r}\|$. The polarities of the point charges q_1 and q_2 determine the direction of the force on their connecting line. Opposite polarities lead to a negative and, thus, attractive force as plotted in Fig. 3.7. Equal polarities, by contrast, result in a positive force and repelling point charges. If there are more than two charge points, the individual force vectors resulting from pair interactions are summed up according to the superposition principle.

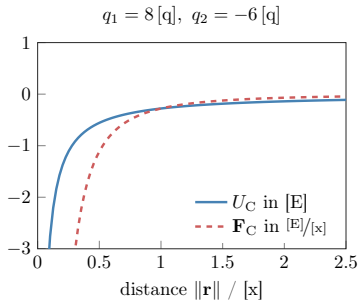

Figure 3.7: Example of an attractive Coulomb potential U_C and the resulting Coulomb force value $\mathbf{F}_\mathrm{C}$ over the distance $\|\mathbf{r}\|$ between the interacting point charges. The values for the charges are arbitrarily chosen as $q_1 = 8\,[\mathrm{q}]$ and $q_2 = -6\,[\mathrm{q}]$. All information is given in the reduced units defined in Tab. 3.1.

Since the potential is approaching zero very slowly ($\propto \frac{1}{\|\mathbf{r}\|}$), the Coulomb energy is referred to as a long-range potential. Hence, it is effective and must be considered even for large distances. Besides the slow decay, the Coulomb potential is singular at $\|\mathbf{r}\| = 0$. As a result, it is difficult to handle in terms of computational effort. The algorithm used in the software package ESPResSo is explained in the following section.

By assigning charges to the auxiliary fiber particles introduced in Fig. 3.6, the method offers the possibility of arbitrarily distributing electrostatic fiber charges. Hence, electrostatic fiber-particle interactions can be taken into account in addition to particle-particle interactions.

3.3 Implementation in the Software Package ESPResSo

The software package ESPResSo (*E*xtensible *S*imulation *P*ackage for *RES*earch on *SO*ft matter), is based on a molecular dynamics approach for soft matter simulations. Classical examples for soft matter systems are polymers, colloids, liquid crystals or glasses [64]. Besides these applications, for which ESPResSo was originally developed, the software package also comprises efficient algorithms for electrostatics [2, 3, 4, 5, 25, 26], dielectrics, magnetostatics and hydrodynamics [86].

By means of coarse-graining, ESPResSo enables simulations with diverse length scales on a mesoscopic level. That also allows for yoking molecules together to dust particles in the size of micrometers as they occur in real aerosols used for testing air filter media. Therefore, ESPResSo does not specify a defined system of units, but allows the user to choose suitable length, time and energy scales. All remaining units such as the mass and electrostatic charge scale are derived from these three basic choices. Table 3.1 presents the system of so-called reduced units used in this work.

	reduced unit	SI unit
Length scale	[x]	$1 \cdot 10^{-5}\,\mathrm{m}$
Time scale	[t]	$1 \cdot 10^{-6}\,\mathrm{s}$
Energy scale	[E]	$1.76 \cdot 10^{-8}\,\mathrm{J}$
Mass scale	[m]	$1.76 \cdot 10^{-10}\,\mathrm{kg}$
Electrostatic charge scale	[q]	$1.60 \cdot 10^{-19}\,\mathrm{C}$

Table 3.1: Specification of the reduced units used in this work.

The following paragraphs provide an insight into the specific implementation of the LBM, the short-range MD and long-range electrostatic MD interactions.

LBM in ESPResSo. The software package ESPResSo uses a D3Q19 model as presented in Fig. 3.2 for discretization. The fluid particle densities f_i in Eq. (3.2) are located in the cell centers of the lattice. Different collision operators are available to relax the velocity populations towards their equilibrium distribution f_i^{eq}. In addition to the simple BGK model where all velocity components are relaxed linearly with the same relaxation parameter, a multiple relaxation concept (MRT) is implemented [5]. It allows defining individual relaxation parameters for different linear combinations of the velocity populations [55]. This way, the fixed ratio between shear and bulk viscosity from the BGK model are overcome.

For modeling the flow domain and obstacles in the domain, the software package ESPResSo provides different shapes such as spheres, cylinders or walls. Moreover, ESPResSo allows importing external files to simulate hydrodynamics in more complex geometries such as filter structures. Zero velocity boundaries are implemented

using the bounce back algorithm [114]. Setting movable LBM boundaries is also supported by adapting the reflected velocity populations [95].

Parallelization of the LBM is implemented via domain decomposition and the MPI communication interface. The subdomains are distributed among the respective CPU ranks. Besides the CPU version, ESPResSo can also employ GPU acceleration. The implementation for a GPU uses the CUDA programming model [86].

Short-Range MD in ESPResSo. A direct calculation of all pairwise interactions requires a high computational effort of $\mathcal{O}(N^2)$, which increases quadratically with the number N of particles. In order to reduce the computational effort, ESPResSo applies different algorithms depending on the effective range of the potential energy. Short-range potentials have the advantage of decreasing very quickly with an increasing particle distance $\|\mathbf{r}\|$. For d-dimensional problems, short-range potentials consist of a linear combination of terms $\propto \frac{1}{r^p}$ with $p > d$ [20]. This property allows considering the potential energy solely within a defined sphere with the radius r_{cutoff}. In combination with the linked-cell algorithm illustrated in Fig. 3.8, the computational effort is reduced to linear complexity $\mathcal{O}(N)$.

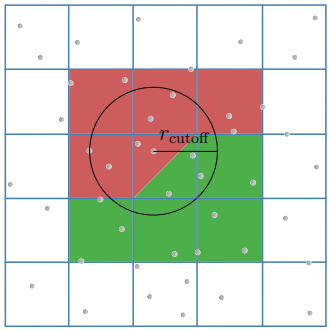

Figure 3.8: Schematic representation of the linked-cell algorithm. The interaction partners of the particle of interest are located in the so-called half-shell neighbored cells (red). By applying Newton's third law, calculating the interactions with the particles located in the area marked in green can be omitted.

The idea of the algorithm is to sort all particles into cubic cells with the edge length r_{cutoff} according to their spatial position. Applying Newton's third law, each pairwise particle interaction has to be calculated only once. Therefore, the consideration of interaction partners in half of the neighboring cells (half-shell neighbors) is sufficient for the force calculation. This further reduces the computational effort. In order to parallelize the linked-cell algorithm, the cells are subdivided equally among the respective ranks. Cuboid sub-volumes are used for the domain decomposition.

The implementation of long-range potentials is presented specifically in the following section using the example of electrostatic particle interactions.

Electrostatics in ESPResSo. The long-range Coulomb potential introduced in Sec. 3.2.3 is slowly decaying with $\|\mathbf{r}\|$ and, therefore, must not be cut off. To calculate the computationally very expensive electrostatic interactions, ESPResSo uses the particle-particle-particle mesh (P^3M) algorithm [21, 64] initially proposed by Hockney and Eastwood [43]. The algorithm is based on the Ewald summation, in which the calculation of the Coulomb energy is split into two parts with

$$\frac{1}{\|\mathbf{r}\|} = \underbrace{\frac{f(\|\mathbf{r}\|)}{\|\mathbf{r}\|}}_{\text{long-range}} + \underbrace{\frac{1-f(\|\mathbf{r}\|)}{\|\mathbf{r}\|}}_{\text{short-range}}, \tag{3.13}$$

where f is the Gaussian error function erf and $(1-f)$ is the complementary error function $erfc$ [25]. The short-range particle-particle (P^2) potential can be tackled in real space based on a cutoff radius and the linked-cell algorithm introduced above. The long-range potential is handled in Fourier space. In this particle-mesh (PM) method, the particles or charge points are interpolated onto a grid. If the long-range part is smooth everywhere and regular at the origin, the summation over all particle pairs can be replaced by pointwise multiplication in Fourier space. The separate consideration of the singularity at each particle position and the slow decay for large distances solves both challenges. The P^3M algorithm leads to a very high accuracy and a computational effort of $\mathcal{O}(NlogN)$ [25, 26]. Thus, the method scales nearly linear with the number N of particles.

3.4 Coupling of the Model Components

The desired fully-coupled system requires the linking of all components presented above, i.e., short-range MD potentials, long-range electrostatics and hydrodynamics. All short-range potentials U_{sr} and long-range potentials U_{lr} acting on a particle are summed up according to the superposition principle

$$U_{\mathrm{total}}(\|\mathbf{r}\|) = \sum U_{\mathrm{sr}}\left(\|\mathbf{r}\|\right) + \sum U_{\mathrm{lr}}\left(\|\mathbf{r}\|\right). \tag{3.14}$$

The bi-directional coupling of the respective solid particles with hydrodynamics is achieved by means of a continuous force exchange as described in detail by Dünweg and Ladd [28]. The MD particle is point-coupled to the LBM via the frictional force density

$$\mathbf{F}(\mathbf{x},t) = -\gamma(\mathbf{u}(\mathbf{x},t) - \mathbf{v}(\mathbf{x},t))\frac{1}{a^3}, \tag{3.15}$$

where γ denotes the friction coefficient given in Eq. (2.11), a the LBM grid spacing, $\mathbf{u}(\mathbf{x},t)$ and $\mathbf{v}(\mathbf{x},t)$ the flow and particle velocity at the position $\mathbf{x}$ at the time t. Hence, the frictional force is proportional to the velocity difference $(\mathbf{u}-\mathbf{v})$ between the fluid and particles. As described by Schiller [88], the frictional force density $\mathbf{F}$ is transformed to LBM external force terms F_i in Eq. (3.2) with suitable transformation rules fulfilling the two conditions

$$\sum_i F_i = 0 \quad \text{and} \quad -\frac{1}{\tau}\sum_i F_i \mathbf{c}_i = \mathbf{F} \tag{3.16}$$

in order to ensure mass and momentum conservation. According to Newton's third law, the opposing force to Eq. (3.15) is exerted on the particle by the background fluid. By contrast, the resulting drag force for a particle i lacks the scaling factor and is given by

$$\mathbf{F}_{\mathrm{d},i}(\mathbf{x}_i(t),t) = 6\pi\eta R(\mathbf{u}(\mathbf{x}_i,t) - \dot{\mathbf{x}}_i(t)). \tag{3.17}$$

LBM and MD time stepping schemes are not synchronized such that multiple MD time steps can be performed during a single LBM time step. Due to the continuous exchange of forces between the fluid and particles, the fully-coupled modeling approach demands very high computational effort, but provides very precise results for the movement of particles.

3.5 Summary

The fully-coupled modeling of particle movement in a background flow field constitutes a fundamentally new approach with respect to filtration processes. The novel modeling approach offers new possibilities to examine important electrostatic filtration effects such as electrostatic particle-particle agglomeration in the inflow area.

To model these effects, the use of a coarse-grained molecular dynamics approach in conjunction with the well-established Lattice-Boltzmann solver is proposed. This chapter presents both, the basics of the applied approaches and the efficient implementation of the underlying models in the software package ESPResSo. Particle collisions resulting from the strong electrostatic attraction are modeled as an elastic collision with a combined adhesive contact. Mathematically, the collision of two particles is described by the Hertzian potential and the harmonic bond potential. These short-range MD potentials are calculated using the linked-cells method. Moreover, a dynamic bonding mechanism serves to detect and handle particle collisions during the simulation.

To model the deposition process of aerosol particles on filter fibers, the short-range MD potentials and the bonding mechanisms are likewise used. For this purpose, fixed auxiliary particles in the fiber geometry serve as bonding partners. Thereby, all key components for simulating the particulate air flow through filter media are modeled. Complementary to the uni-directional status quo approach, the fully-coupled modeling provides the potential to focus on previously neglected electrostatic particle-particle agglomeration effects between particles.

Chapter 4

Modeling & Simulation of Single Fibers

The complexity of three-dimensional fibrous structures poses major challenges regarding the simulation of filtration performances. To verify the fundamentally new four-way coupled simulation approach, a single fiber provides a more suitable model and better starting point. It represents a very simple structure, which allows the depiction of the most important relevant collection mechanisms (see Sec. 2.1) and is, therefore, widely used in the field of air filtration. As a key parameter, the single fiber efficiency, moreover, allows drawing conclusions about the filtration behavior of unloaded filter media [22]. Therefore, both experimental [10, 40, 70, 80, 82, 92, 113] and simulation studies [40, 61, 70, 71, 80, 96, 112] have been carried out extensively on the basis of single fibers in the last decades (see literature review in Sec. 2.4). The main outcome of previous publications were several fit functions characterizing the particle deposition process on the surface of the fiber. Kasper et al. [50] summarized a selection of notable expressions for the collision efficiency derived from diverse research projects, which, however, are all only valid in certain Stokes and Reynolds regimes.

In Sec. 4.1, the single fiber is used to verify the fundamentally new fully-coupled modeling approach by means of simulating conventional mechanical collection mechanisms. Subsequently, individual electrostatic filtration effects are analyzed in detail in Sec. 4.2 and Sec. 4.3, using the single fiber model as well as simple fiber arrays.

4.1 Verification of Four-Way Coupled Modeling Approach

In this section, the single fiber model serves as a proven benchmark scenario in order to verify the newly deployed four-way coupled simulation approach. Since a single fiber constitutes the smallest representative element of a real filter medium, it allows simulating the collision efficiency of airborne particles with feasible computational effort. Therefor, this clearly defined scenario provides a good basis to evaluate the validity of the novel four-way coupled simulation approach. To this end, it is initially examined whether the fundamentally new modeling approach can be used to reproduce the particle deposition results caused by mechanical filtration effects which can also be modeled using the well-established uni-directionally coupled simulation approach. Therefore, the simulation of combined efficiencies by inertia and interception, only serves as an appropriate comparison scenario. As a basis for the verification the simulation experiment proposed by Müller et al. [71] is used.

The setup and procedure of the single fiber simulation study are described in detail in Sec. 4.1.1. Subsequently, the results generated with both simulation approaches – uni-directional coupling with GeoDict and four-way coupling with ESPResSo – are presented, and additionally compared to published data in Sec. 4.1.2.

4.1.1 Simulation Experiment Setup

This section presents the applied simulation workflow used to verify the applicability of the fully-coupled simulation approach in the field of air filtration. Firstly, the characteristics of the single fiber setup are comprehensively described. Secondly, the procedure of the simulation runs themselves as well as the evaluation of the simulated collision efficiency are introduced.

4.1.1.1 Simulation Domain & Boundary Conditions

The single fiber setup used in this work consists of a cylindrical fiber in a periodic row, which is realized by periodic boundary conditions in cross-flow direction. The resulting fiber array gives more realistic agreement with the behavior of real filter media than one isolated fiber [50]. The left-hand side of Fig. 4.1 shows a two-dimensional sketch of the simulation domain based on detailed specifications presented by Müller et al. [71]. All simulation runs, though, are performed in three

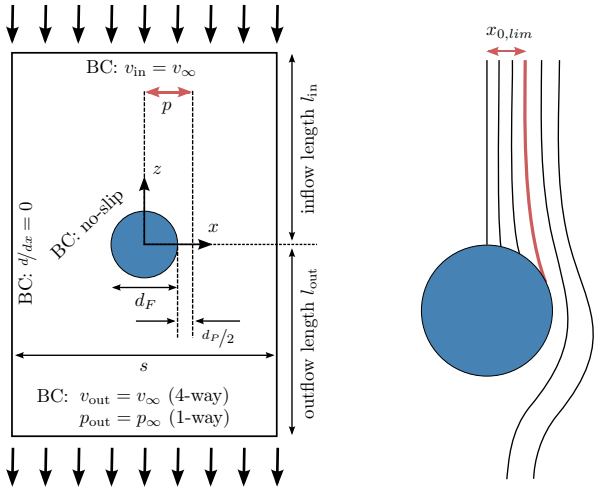

Figure 4.1: Two-dimensional display of the experimental setup and boundary conditions for the simulation of a single fiber in a periodic row (left). Schematic trajectories for particles with different starting positions along the particle addition zone p (right). The trajectory highlighted in red indicates the limiting trajectory, whose starting position $x_{0,\mathrm{lim}}$ is necessary for the calculation of the single fiber collision efficiency.

dimensions using a constant depth of 40 µm in y-direction.

The cylindrical fiber is placed in the center of the domain with a dimensionless fiber offset s/d_F in x-direction. In ESPResSo, the air flow around the fiber in negative z-direction is driven by applying Dirichlet boundary conditions with the undisturbed air velocity v_∞ at the inlet and the outlet. With the GeoDict software by contrast, Dirichlet boundary conditions are only applied at the inlet and Neumann boundary conditions with the ambient air pressure $p_\infty = 1013\,\mathrm{mbar}$ are used at the outlet. The influence of this difference will be covered in more detail in Sec. 4.1.2.2. In both software approaches, no-slip boundary conditions are employed at the fiber surface. The schematic illustration furthermore depicts the line segment p, where particles are inserted into the flow region.

4.1.1.2 Simulation & Evaluation Procedures

As a pre-processing step, the pure fluid flow field around the single fiber is calculated until a stable state is reached. Therefore, a grid spacing of $a = 1\,\mu\text{m}$ is used for the spatial discretization of the simulation domain. Subsequently, one particle at a time is added to the specified section p in the inflow area. This excludes particle-particle interactions in the four-way coupled approach, making the achieved single fiber results comparable to those from the one-way coupled simulation. The length of the line segment

$$p = \frac{d_\text{F}}{2} + \frac{d_\text{P}}{2} \tag{4.1}$$

results from the outermost particle starting position with which it is theoretically possible for a particle to come into contact with the fiber. This case only occurs if the particle trajectory is not affected by the air flow field at all and the particle moves in an undisturbed straight line. The dimensionless interception parameter

$$R = \frac{d_\text{P}}{d_\text{F}}, \tag{4.2}$$

which is kept constant at $R = 0.1$ for all simulation runs, yields the length of particle provision segment p.

In this work, the trajectories for a total number of 120 particles are calculated for each simulation setup. Their respective starting positions are equidistantly distributed over the particle addition segment. Depending on the software approach, tracing the particles follows the respective method described in Sec. 2.3 or Sec. 3.4. During particle tracking, the algorithms constantly search for a collision of the particles with the fiber surface. The well-established uni-directionally approach of the software GeoDict delivers this feature out-of-the-box. In the four-way coupling approach, this is implemented by querying the distance between the particle center and the center of the fiber after each time step. A collision occurs at a distance of p or smaller. Since rebound effects are completely neglected in this section, a collided particle is always considered as deposited. After the particle has been collected or passed by the fiber, it is deleted from the simulation domain and the initial flow field is loaded again. Note that, the uni-directional coupling approach allows all particles to be tracked at the same time as they do not influence each other.

It is evident that particles which are added closer to the center axis of the fiber are more likely to be separated. Based on the outermost trajectory leading to a contact of the particle with the fiber, which is depicted on the right-hand side of Fig. 4.1, the single fiber collision efficiency η_{SF} is deduced. The efficiency is given by

$$\eta_{\mathrm{SF}} = 2\frac{x_{0,\mathrm{lim}}}{d_{\mathrm{F}}}, \tag{4.3}$$

where $x_{0,\mathrm{lim}}$ denotes the starting position of the limiting trajectory in x-direction.

In the following comparison of the one-way and the four-way coupled approach, results for the effect of different flow fields are investigated. For this purpose, the dimensionless fiber offset s/d_{F} and the Reynolds number

$$Re = \frac{\rho_{\mathrm{air}}\, v_\infty\, d_{\mathrm{F}}}{\eta_{\mathrm{air}}} \tag{4.4}$$

are varied. The Reynolds number is set by adjusting the value for the air velocity v_∞ in z-direction. The density $\rho_{\mathrm{air}} = 1.204\,\mathrm{kg/m^3}$ and dynamic viscosity $\eta_{\mathrm{air}} = 1.834 \times 10^{-5}\,\mathrm{kg/(m\,s)}$ of air are predefined and kept constant. Reynolds numbers between $Re = 0.2$ and $Re = 5$ are investigated. Simulation runs are performed for each parameter set with Stokes numbers

$$St = \frac{\rho_{\mathrm{P}}\, d_{\mathrm{P}}^2\, v_\infty}{18\,\eta_{\mathrm{air}}\, d_{\mathrm{F}}} \tag{4.5}$$

ranging from $St = 0.02$ to $St = 500$. The particle density ρ_{P} is varied for this purpose. All parameters used for the single fiber simulations are summarized in Tab. 4.1.

4.1.2 Numerical Results for Mechanical Particle Collection

According to the described workflow, various simulation runs are performed in order to verify the new modeling approach. Firstly, some preliminary investigations are carried out to determine correct numerical parameters and, thus, to ensure the simulation of realistic particle trajectories. In particular, the influence of the coupling intensity between fluid and particles, represented by the friction coefficient γ_{bare}, is analyzed for the novel fully-coupled simulation approach. In addition, the

Parameter		Value
Stokes number	St	0.02 - 500
Reynolds number	Re	0.2 - 5
Fiber offset	s/d_F	2 - 10
Interception parameter	R	0.1
Dynamic viscosity (Air)	η_{air}	$1.834 \cdot 10^{-5}\ \frac{kg}{ms}$
Density (Air)	ρ_{air}	$1.204\ \frac{kg}{m^3}$

Table 4.1: Overview of the parameter ranges used for the simulation of single fiber collision efficiencies η_{SF}.

required lengths for inlet l_{in} as well as outlet l_{out} region are determined for both modeling approaches used in order to ensure comparability.

Based on the knowledge gained, finally a detailed comparison of the simulation results obtained by the fully-coupled and uni-directionally coupled modeling approaches are presented. In addition, the obtained single fiber collision efficiencies η_{SF} are compared to published data by Müller et al. [71].

4.1.2.1 Influence of the Coupling Intensity

While a particle is transported in the direction of the fiber, a frictional force is acting on the interface between the particle and the background air flow according to Eq. (3.17). The intensity of the friction determines whether a particle follows the streamlines or deviates from them due to inertia. In other words, the simulated collection through inertia depends to a large extent on the coupling strength.

The effective particle mobility $\mu_{eff} = 1/\gamma_{eff}$ resulting from Eq. (2.11) is composed of two parts, i.e., the bare mobility μ_{bare} by the relative velocity $(\mathbf{v} - \mathbf{u})$ between particle and fluid, and a purely hydrodynamic term μ_{HD}, according to

$$\mu_{eff} = \frac{1}{\gamma_{bare}} + \mu_{HD}. \tag{4.6}$$

The latter, hydrodynamic part

$$\mu_{HD} = \frac{1}{g\eta_{air}a} \tag{4.7}$$

contains the feedback from the fluid and, thus, involves the dynamic fluid viscosity η_{air} as well as the lattice spacing a. The numerical factor g has been extensively tested for the software package ESPResSo and was found to be $g \approx 25$ regardless of the bare coupling coefficient γ_{bare} and lattice spacing a [1, 5]. The point force in ESPResSo only includes the bare friction coefficient γ_{bare}, which can be adjusted as needed. Based on Eq. (4.6) and Eq. (4.7), this coefficient is determined to be $8 \cdot 10^{-6}\,{}^{[m]}/_{[t]}$ under the defined conditions used in this work, summarized in Tab. 4.1. The reduced units used for the simulation runs are specified in Tab. 3.1.

The bare friction coefficient can also be determined experimentally by pulling a particle through a flow field with a constant velocity by a constant force $\mathbf{F}$. The stationary velocity $\mathbf{v}_{\text{s}}$ that the particle finally reaches allows calculating the effective mobility according to

$$\mu_{\text{eff}} = \frac{\|\mathbf{v}_{\text{s}}\|}{\|\mathbf{F}\|}. \tag{4.8}$$

For this experiment, the bare friction coefficient must be chosen such that the resulting effective mobility corresponds to the Stokes friction.

The strong influence of the coefficient γ_{bare} on the single fiber collision efficiency simulated with the four-way coupled approach is demonstrated in Fig. 4.2 for various Stokes numbers. All curves show the typical shape for a combined inertia and interception collection. Particles with small Stokes numbers, i.e., low particle densities, can easily follow the streamlines around the fiber and therefore show a collision efficiency close to zero. Some particles nevertheless come into contact with the fiber due to their geometric expansion. With a growing Stokes number, the inertial collection plays an increasingly important role resulting in raised collision efficiencies up to more than $\eta_{\text{SF}} = 100\,\%$. Note that, collision efficiencies up to $\eta_{\text{SF}} = 110\,\%$ are possible in this single fiber simulation experiment due to the calculation according to Eq. (4.3).

An impact of the investigated bare friction coefficient γ_{bare} on the collision efficiency is clearly recognizable: Low friction coefficients cause the particles to detach easily from the streamlines and, thus, to collide with the fiber even for high starting positions $x_{0,\text{lim}}$. With an increasing intensity of fluid-particle coupling, the probability of impact decreases and converges against a fixed value for each Stokes number. The simulation study reveals the importance of considering the

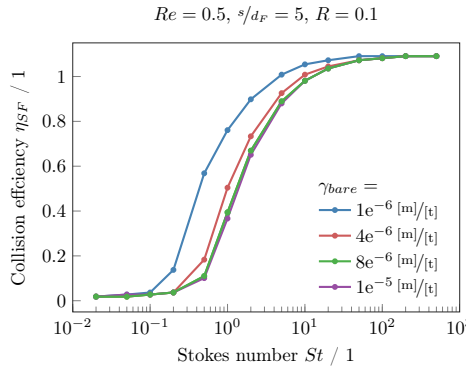

Figure 4.2: Single fiber collision efficiency η_{SF} over the Stokes number St for various coupling strengths between fluid and particles. For this purpose the applied friction coefficient γ_{bare} in ESPResSo was varied.

hydrodynamic mobility part for the simulation of particles moving in an air flow field.

4.1.2.2 Influence of the Domain Size

In addition to the correct friction intensity, the undisturbed air velocity at the inlet and the outlet must be ensured. A non-zero horizontal velocity component at the starting positions of the particles would lead to a falsified collision behavior. In order to avoid this, inlet and outlet lengths must be chosen sufficiently large. The analysis is carried out separately for both software approaches as different boundary conditions are used at the outlet.

Since the focus of the single fiber experiment is on the inertial collection and, thus, on the ability of particles to follow the streamlines, the collision efficiencies strongly depend on the fluid flow. The initial stable flow field in turn is decisively determined by the specified domain size. Since there is no fluid motion in y-direction, the domain expansion in this direction does not need to be investigated. Hence, only the lengths of the inflow and outflow areas remain as critical parameters. Both software approaches, i.e., one-way and four-way coupled, are analyzed in the following. The fiber offset is preset to $s/d_{\mathrm{F}} = 5$ for these experiments.

Results for the Uni-Directionally Coupled Approach. To initiate the flow field, the uni-directionally coupled approach uses an inlet velocity and an outlet pressure. Under these boundary conditions, the inlet length is varied in the first step, while keeping the outlet length $l_{\text{out}} = 12.5\,\text{d}_\text{F}$ constant. The left-hand side of Fig. 4.3 shows the simulated collision efficiencies for a fixed Stokes number $St = 10$ over the dimensionless inflow length ${}^{l_\text{in}}/_{d_\text{F}}$.

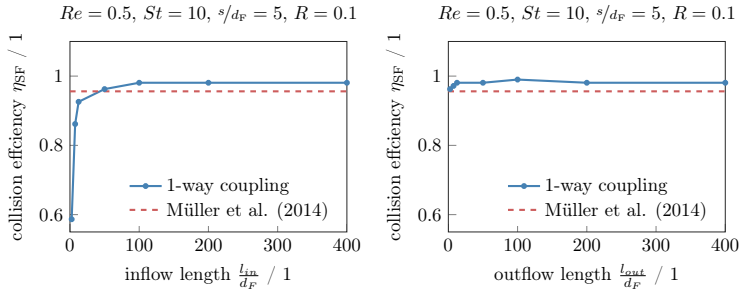

Figure 4.3: Influence of inflow (left) and outflow (right) length on the single fiber collision efficiency obtained by the uni-directionally coupled approach implemented in the software GeoDict. The results are shown for a constant Stokes number $St = 10$. In addition to the simulated efficiencies, the published value by Müller et al. [71] is plotted as constant dashed, red line.

The plot demonstrates that small inflow lengths extremely affect the degree of particle impact. If the length is chosen too short, the flow field contains a velocity component in x-direction at the height of the particle starting positions. This causes the particles to drift away from the fiber axis right at the beginning, and directs them around the fiber more likely. From a length of $l_\text{in} = 100\,\text{d}_\text{F}$, a constant level for the collision efficiency is reached. The diagram additionally contains the value achieved by Müller et al. [71] for the given parameter set: $Re = 0.5$, $St = 10$, ${}^{s}/_{d_\text{F}} = 5$ and $R = 0.1$. This value ($\eta_\text{SF} = 0.956$), marked as dashed red line, seems to be slightly overestimated if the results obtained by using the uni-directional coupling approach are followed. However, the deviation of about 2.6 % is negligibly small.

The right-hand side of Fig. 4.3 depicts the results for the same procedure, but analyzing the outflow length. In generating these results, the required inflow length of $l_{\text{in}} = 100\,\text{d}_\text{F}$ is chosen and constant. The plot shows that, for a sufficiently large inlet length, the outlet length no longer plays a decisive role. Only for very small outflow lengths ($l_{\text{out}} < 7.5\,\text{d}_\text{F}$), a minimal reduction in the collision efficiency is observed. This results in a required total height of the simulation domain of $l_{\text{total}} = 107.5\,\text{d}_\text{F}$, which is comparatively low with respect to the proposed value $l_{\text{total}} = 252\,\text{d}_\text{F}$ by Müller et al. [71].

Results for the Fully-Coupled Approach. The experiments are carried out similarly with the novel, four-way coupled modeling approach. Figure 4.4 shows the corresponding results for the simulated single fiber collision efficiencies with varying inflow (left) and outflow (right) lengths.

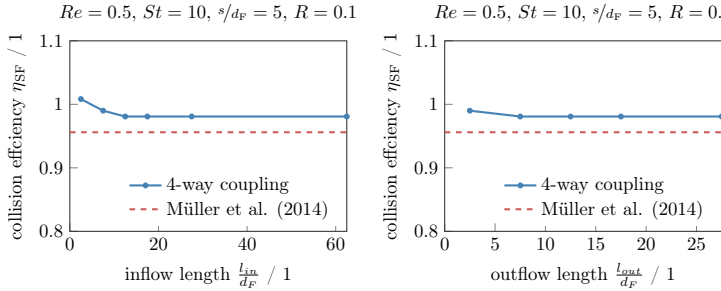

Figure 4.4: Influence of inflow (left) and outflow (right) length on the single fiber collision efficiency obtained by the fully-coupled simulation approach implemented in the software ESPResSo. The results are shown for a constant Stokes number $St = 10$. In addition to the simulated efficiencies, the published value by Müller et al. [71] is plotted as constant dashed red line.

Both curves are now approaching the published value by Müller et al. [71] from above. This effect is caused by the velocity boundary conditions at the in- and outlet. If the domain height is chosen too low, the fluid has not enough time to evade the fiber obstacle. This also presses the particles more strongly against the fiber and causes raised collision efficiencies. However, a constant level is also reached

with the fully-coupled simulation approach using an inflow length $l_{\text{in}} = 12.5\,\text{d}_\text{F}$ and outflow length $l_{\text{out}} = 7.5\,\text{d}_\text{F}$. With the new modeling approach, a much smaller total domain height $l_{\text{total}} = 20\,\text{d}_\text{F}$ is thus sufficient. Nevertheless, the simulated single fiber collision efficiencies also exceed the literature value by about 2.6 %.

4.1.2.3 Comparison of Simulation Methods

For a meaningful comparison between the two software approaches of interest, the preliminary results for the friction coefficient as well as the domain height are taken into account. In order to cover a wide range of air flow conditions, the two dimensionless parameters are varied: fiber offset $^s/_{d_\text{F}}$ and Reynolds number Re.

Influence of the Fiber Offset. Depending on the dimensionless fiber offset $^s/_{d_\text{F}}$, the fiber differently affects the air flow field. The resulting dissimilar trajectories lead to discrepancies in the collision efficiency [69]. This section is about verifying the newly deployed modeling approach over a wide range of parameters. The three diagrams plotted at the end of this section in Fig. 4.5 show the curve of single fiber collision efficiencies for different ratios of domain width to fiber diameter: $^s/_{d_\text{F}} = [2,\ 5,\ 10]$. All diagrams contain the results obtained by the novel four-way coupled approach, the status-quo one-way coupled simulation and published data by Müller et al. [71].

For this simple scenario, good agreement is achieved between the results from all presented simulation methods. The new modeling approach shows only minimal deviations in terms of collision efficiency over the complete investigated parameter range for $^s/_{d_\text{F}}$. To quantify the deviation obtained by two different modeling approaches M1 and M2, the relative error δ_{SF} is used. Based on the method of least squares, δ_{SF} is determined according to

$$\delta_{\text{SF}} = \left(\frac{1}{i} \sum_{\text{St}=0.02}^{500} \left(\eta_{\text{St,M1}} - \eta_{\text{St,M2}}\right)^2 \right)^{\frac{1}{2}}, \tag{4.9}$$

where i denotes the number of Stokes numbers examined. Calculating the relative error for the results from the four-way coupled compared to the one-way coupled simulation leads to a maximum (when comparing the three parameter sets) of $\delta_{\text{SF}} = 2.6\,\%$. The additional comparison with published data is also highly satisfactory.

In this case, the maximum relative error is $\delta_{\mathrm{SF}} = 4.9\,\%$. The largest deviations occur for the smallest fiber offset $^{s}/_{d_{\mathrm{F}}} = 2$. With an increasing fiber offset, the spread shrinks. It is noticeable, however, that both, the one-way and the four-way coupled simulation, slightly exceed the published results over almost the complete parameter ranges.

Influence of the Reynolds Number. The Reynolds number Re also influences the flow pattern and, thus, the resulting collision efficiency of the single fiber. Figure 4.6, also attached at the end of this section, shows the comparison of the results obtained by the different approaches for three Reynolds numbers: $Re = [0.2,\ 0.5,\ 5]$. The fiber offset is fixed to $^{s}/_{d_{\mathrm{F}}} = 5$ for this analysis.

As already in the case of the fiber offset analysis, all curves for a particular set of parameters coincide well. The maximal occurring relative error $\delta_{\mathrm{SF}} = 3.4\,\%$ between the new four-way coupling and the well-established one-way coupling approach is insignificantly small. The trend towards moderately increased collision efficiencies for the generated data compared to published data, however, is observed again. The maximal relative error to the published data by Müller et al. [71] is a little higher with $\delta_{\mathrm{SF}} \leq 3.9\,\%$.

The results by means of the simple scenario prove that the fully-coupled simulation approach implemented in the software package ESPResSo is well suitable for the use in air filtration. Therefore, the approach is used in the following chapters to simulate electrostatic filtration effects that can not be covered by the uni-directionally coupled status quo approach.

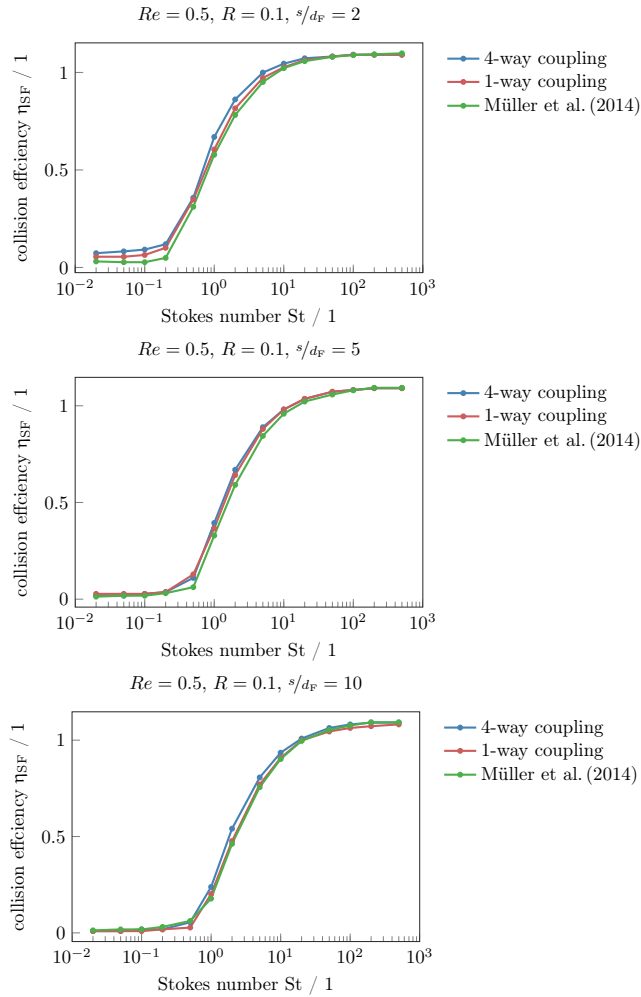

Figure 4.5: Comparison of single fiber efficiencies η_{SF} simulated with the fully-coupled system, the one-way coupled approach and published data by Müller et al. [71]. In order to ensure comparability, uncharged particles and fibers are employed. Interactions between particles in the four-way coupled approach are omitted by simulating them consecutively. In the three plots, the dimensionless fiber offset s/d_F is varied.

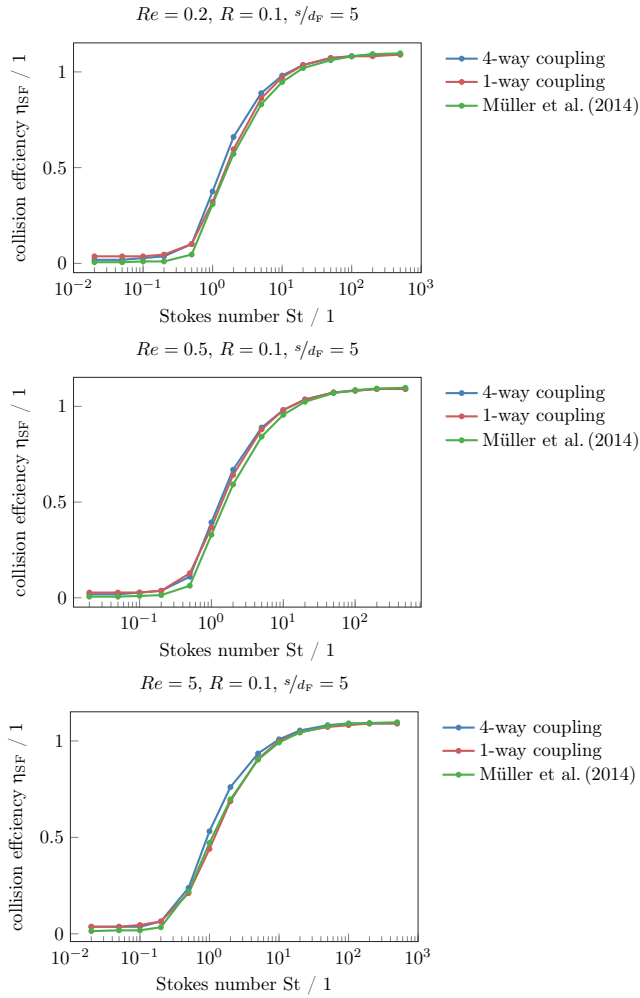

Figure 4.6: Comparison of single fiber efficiencies η_{SF} simulated with the fully-coupled system, the one-way coupled approach and published data by Müller et al. [71]. In order to ensure comparability, uncharged particles and fibers are employed. Interactions between particles in the four-way coupled approach are omitted by simulating them consecutively. In the three plots, different Reynolds numbers Re are examined.

4.2 Uni-Directional Simulation of Charged Single Fibers

The rather simple model of a single fiber is not only perfectly suitable for the simulation of mechanical collection mechanisms, but also for analyzing electrostatic fiber-particle interactions. To characterize the additional attraction between the fiber and incoming particles by Coulomb effects, the modeled fiber depicted in Fig. 4.1 is considered electrostatically charged in this section.

As both, the charge intensity and the charge distribution on fiber surfaces, are hardly accessible by experiments and are therefore unknown, the choice of appropriate electrostatic parameters poses great challenges. Besides a unipolar charge distribution [11, 17, 73, 77], fibers with a permanent dipole [17, 23, 45, 53] are often proposed in literature. Since both polarities are present on dipole charged fibers, they are capable of filtering positively and negatively charged particles efficiently. The simulation in contrast enables arbitrary charge distributions, but already for the single fiber model numerous variations are conceivable. Therefore, the aim of this section is to elaborate the basics of Coulomb separation by analyzing some reasonable parameter variations. More precisely, the influence of unipolarly and dipole charged fibers on the separation efficiency is investigated. In addition to the arrangement of electrostatic charges on the fiber surface, the charge intensity is varied. By means of these two parameters, i.e., distribution and intensity, the high complexity of electrostatic filtration effects is intended to be demonstrated.

Since the focus of this section is on fiber-particle interactions, the uni-directional coupling method is used for all simulation studies. The software package GeoDict, moreover, already provides an implementation for the uniform and unipolar charge distribution on fiber surfaces. Firstly, this basic charge distribution is used to quantify the influence of the charge intensity. Secondly, the source code of the software is extended in order to model dipole charged fibers (and other charge distributions along the fiber axis such as linear, sinusoidal or step functions which are not dealt with in more detail). For this case, the orientation of the dipole with respect to the flow direction is investigated in addition to different charge intensities.

4.2.1 Simulation Experiment Setup

In principle, the setup from Fig. 4.1 is also used for the simulation of electrostatically charged fibers. The fiber offset $s/d_F = 5$ and the interception parameter $R = 0.1$ are kept constant in this case. A Reynolds number $Re = 0.5$ is applied for the simulation of the background flow field. In order to generate a Coulomb interaction between the fiber and incoming particles, an electrostatic charge must also be assigned to the particles. Since the focus is intended to be on the fiber charge configuration in this section, all particles are charged with a constant, arbitrarily chosen charge density $\xi_P = -1 \cdot 10^{-6}\,\mathrm{C/m^2}$. This way, it is ensured that only one parameter is varied at a time. Besides the electrostatic charging, the only further deviation from the previous experimental setup is the method of particle addition: The electrostatic attraction from the fiber allows particles to be separated despite the fact that they are added at great distances from the projection of the fiber axis, i.e., at high x_0. In order to take all particle starting positions into account which could potentially lead to a separation, a generous line segment $p = 3\,d_F$ is chosen. Since the particles can also move across the fiber axis for certain fiber charge configurations, this line segment is aligned centrally above the fiber. Furthermore, the number of simulated particles is increased to 2000 in order to obtain accurate results for the separation efficiency. The particle starting positions are still equidistantly distributed over p.

Distributing a unipolar charge density ξ_F on the entire surface of a fiber is part of the standard GeoDict software. The calculation of the resulting force on charged particles is implemented as described in 2.3. The procedure for distributing charges according to the user specified fiber charge density ξ_F is explained in the following by means of the fiber cross section plotted in Fig. 4.7. In a first step, the surface voxels of the fiber must be identified. To get this information for each slice of the fiber, the algorithm runs through the simulation domain in x- and z-direction consecutively. All voxels detected as adjacent to one edge of the fiber are marked as surface voxels and a charge is assigned to them. Since the actual surface – highlighted in green – is always located between two voxels, the quantity of charge is divided over both neighboring voxels. The coloring of the voxels in the figure shows the Laplace operator of the electrostatic potential Φ as the result of Eq. (2.14)

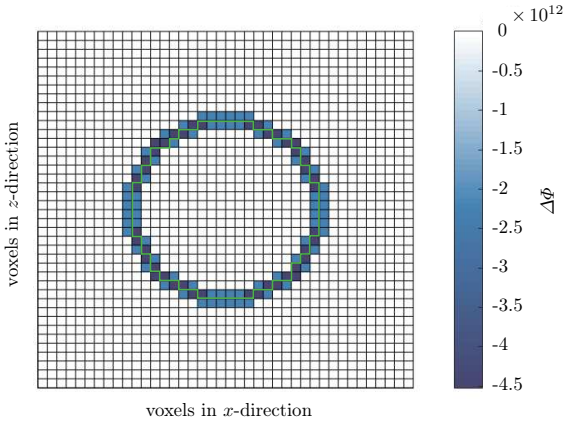

Figure 4.7: Cross section of a part of the voxel discretized simulation domain in the software GeoDict containing a single fiber. A unipolar and uniformly distributed charge density $\xi_F = 4 \cdot 10^{-5}\,\mathrm{C/m^2}$ is applied to the fiber surface. This charge is assigned to all voxels adjacent to the actual fiber surface highlighted in green. The coloring of the voxels shows the resulting values for $\Delta\Phi$ depending on how many edges touch the surface of the fiber.

for an exemplary applied surface charge density $\xi_F = 4 \cdot 10^{-5}\,\mathrm{C/m^2}$. Integrating in both directions results in some voxels (with two adjacent edges) receiving the actual value for $\Delta\Phi$, others (with one adjacent edge) receiving only half.

To model a dipole in GeoDict, a plane is defined that splits the fiber into two halves of equal size. A positive charge density is then assigned to all fiber surface voxels on one side of the plane, and a negative charge density to those on the other side. This leads to the distribution of $\Delta\Phi$ plotted in two dimensions in Fig. 4.8 for the same exemplary fiber charge density $\xi_F = 4 \cdot 10^{-5}\,\mathrm{C/m^2}$. In this example, the plane is spanned in y-z-direction and the resulting dipole is thus rotated by $\alpha = 90°$. Apart from having a bipolar charge distribution, the allocation on the surface voxels is carried out analogously to the unipolarly charged fiber.

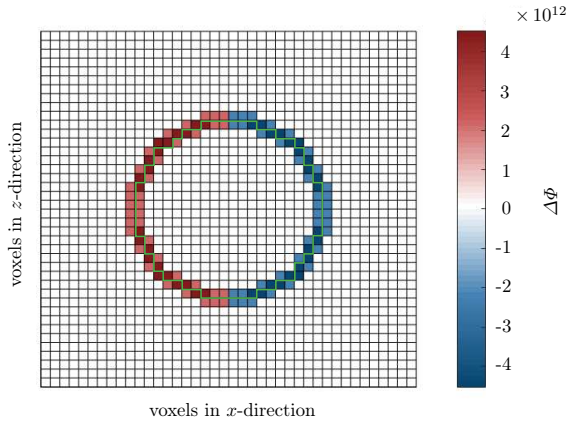

Figure 4.8: Cross section of a part of the voxel discretized simulation domain in the software GeoDict containing a single fiber. The fiber boasts a dipole charge distribution with a charge density $\xi_F = 4 \cdot 10^{-5}\,\mathrm{C/m^2}$. Positive and negative charges are assigned to the surface voxels depending on which side of the dipole plane the voxels are located. The actual fiber surface is highlighted in green again. The coloring of the voxels shows the resulting values for $\Delta\Phi$ depending on how many edges touch the surface of the fiber.

4.2.2 Numerical Results for Unipolar Fiber Charges

Originating from each charged surface voxel, a potential spreads out into the simulation domain depending on the distance r. The resulting aggregated potential Φ initiated by the unipolarly charged single fiber is plotted in Fig. 4.9. This electrostatic potential directly correlates with the force on a charged particle in the simulation domain according to Eq. (2.15) and Eq. (2.16). In the direction of flow only a small part of the simulation domain ($\approx 14\,\%$ of the total domain height) is displayed in order to visualize the fast decrease ($\propto 1/r^2$) of the potential. Figure 4.10 depicts the entire domain to additionally show that the potential completely vanishes at the inlet and the outlet. Hence, the injected particles are not influenced by the electrostatic field at the beginning of the tracking. Only when they get closer to the fiber, an attraction or repulsion occurs depending on the polarity of their charge.

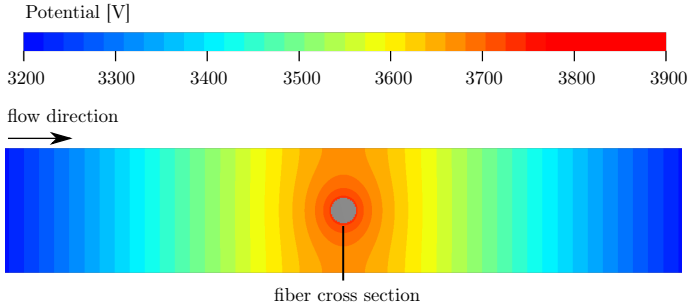

Figure 4.9: Electrostatic potential Φ induced by a unipolar surface charge density $\xi_F = 4 \cdot 10^{-5}\,\mathrm{C/m^2}$. Only a part of the simulation domain is shown in the direction of flow.

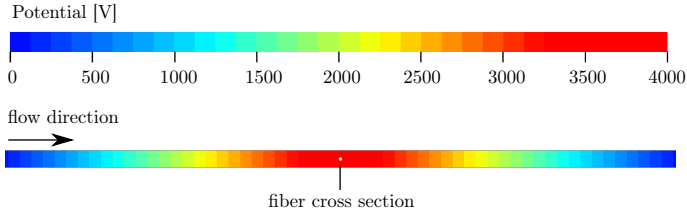

Figure 4.10: Electrostatic potential Φ induced by a unipolar surface charge density $\xi_F = 4 \cdot 10^{-5}\,\mathrm{C/m^2}$ over the total simulation domain.

The behavior of uniformly charged particles in the electrostatic field is illustrated in Fig. 4.11. The particle trajectories are plotted for different charge conditions. To mathematically describe the electrostatic charging state the charge density ratio

$$\theta = -\frac{\xi_F}{\xi_P} \quad \text{for} \quad \xi_P \neq 0 \tag{4.10}$$

between the fiber ξ_F and the particle ξ_P charge density is introduced. The particle trajectories show clear differences depending on this charge density ratio θ. Strongly, equally charged fibers and particles ($\theta = -20$) cause all particles to pass around

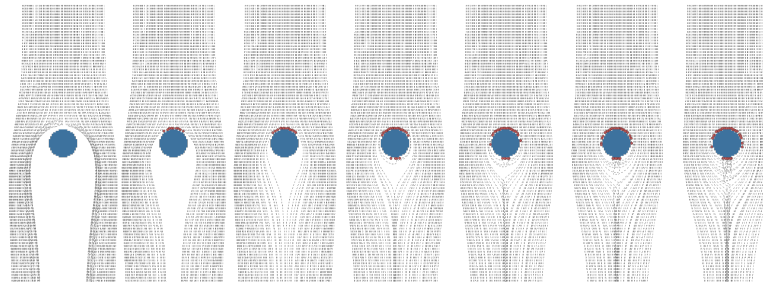

(a) $\theta = -20$ (b) $\theta = -8$ (c) $\theta = 0$ (d) $\theta = 20$ (e) $\theta = 40$ (f) $\theta = 60$ (g) $\theta = 80$

Figure 4.11: Particle trajectories around unipolarly charged fibers simulated with the uni-directional coupling implemented in the software package GeoDict. Particles collided with the fiber surface are indicated in red. The charge density ratio θ increases in the images from left to right. Both, particle size ($d_\mathrm{P} = 2\,\mu\mathrm{m}$) and particle charge density ($\xi_\mathrm{P} = -1 \cdot 10^{-6}\,\mathrm{C/m^2}$), are identical in all simulation runs. For better visualization, only 100 particle trajectories are plotted for each illustration (2000 particles are tracked to determine the collection efficiency).

the fiber. Particles which move towards the fiber due to their inertia change their direction shortly before a possible collision. Due to the strong repulsive force, they partially bounce off at an acute angle (before touching the fiber) and move past the fiber thereafter. This rebound effect is no longer observed for a lower charge density ratio $\theta = -8$. Most particles are still visibly directed around the fiber. For some particles, however, inertia outweighs the electrostatic repulsion force and causes the particles to hit the fiber despite being charged with the same polarity. Particles collided with the fiber surface are indicated in red. Compared to the neutral fiber ($\theta = 0$), the particle trajectories are on average further away from the fiber. Thus, significantly more particles deposit on the uncharged fiber, where only mechanical collection mechanisms are effective. If the fiber and particles are oppositely charged, particles attach to the fiber both upstream and downstream. The higher the charge density ratio, the more particles that are already passing the fiber are deflected from the streamlines in such a way that they reach the fiber from behind. Due to the strong electrostatic attraction, some particles even move

upwards against the flow direction. Looking at the trajectories from all charge conditions at a glance, it is additionally noticeable that the particle trajectories behind the fiber differ significantly. This in turn is bound to have crucial effects on the deposition behavior on subsequent fibers in a real filter medium. Therefore, the consequences are examined in more detail in Sec. 4.3 on the basis of fiber arrays.

The influence of the different particle trajectories around unipolarly charged single fibers with regard to the number of separated particles are summarized in Fig. 4.12. The method of the limiting trajectory based on Eq. (4.3) is still used to calculate the collection efficiency.

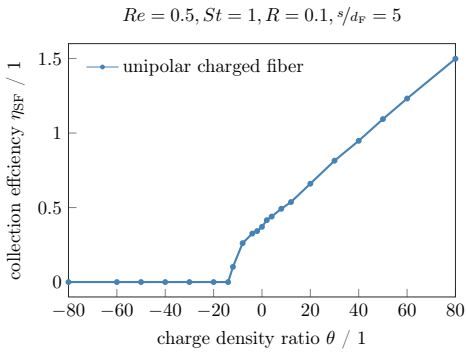

Figure 4.12: Single fiber collection efficiency η_{SF} depending on the applied fiber charge intensity. Both, particle size ($d_P = 2\,\mu m$) and particle charge density ($\xi_P = -1 \cdot 10^{-6}\,C/m^2$), are identical in all simulation runs.

Strongly negative charge density ratios, i.e., same polarities for the fiber and particles, cause no particles at all to collide with the fiber and, thus, result in $\eta_{SF} = 0$. When the absolute value of the charge density ratio decreases, the repulsive force is no longer sufficient to exceed the inertial effects. Hence, there are still low collection efficiencies ($\eta_{SF} \leq 37\,\%$) achieved for these charge configurations. Opposite polarities of the fiber and particles lead to a linear increase of the separation efficiency. Since the particles are added over a large range p, the efficiency also increases significantly beyond $\eta_{SF} = 100\,\%$. In a nutshell, the uniformly, unipolarly charged fiber is excellently suited for separating particles of

the opposite polarity, but the charge distribution is not suitable for filtering equally charged particles efficiently.

4.2.3 Numerical Results for the Expansion to Dipole Fibers

Following, the rotation of the dipole plane in relation to the inflow direction is examined in addition to the assigned charge intensity. The investigation aims to show the influence of the fiber orientation on the particle deposition behavior. For illustration, the emerging potential is plotted for different rotation angles α in Fig. 4.13. The reference angle $\alpha = 0°$ defines a dipole plane perpendicular to the flow direction with an attractive potential directed towards the incoming particles. Starting from there, the rotation is clockwise.

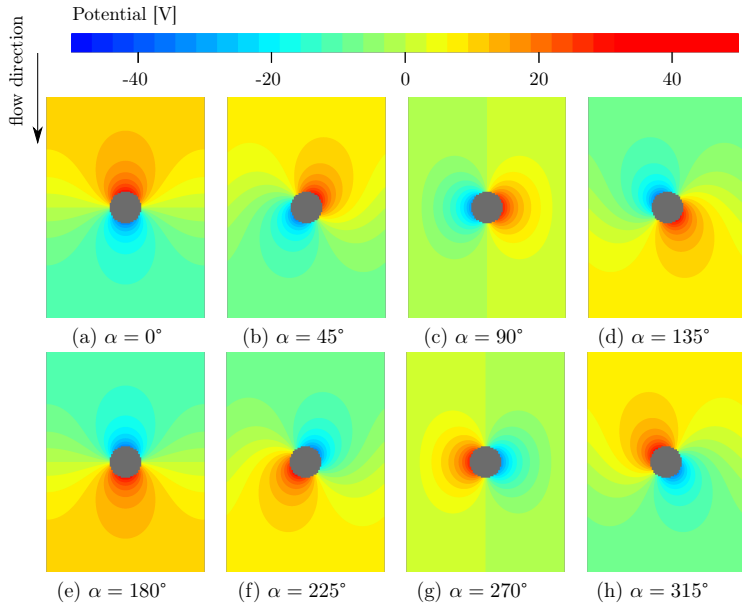

Figure 4.13: Electrostatic potential Φ for dipole charged fibers which are aligned differently with respect to the direction of flow. In each case, only a small section of the simulation domain around the fiber is shown in z-direction.

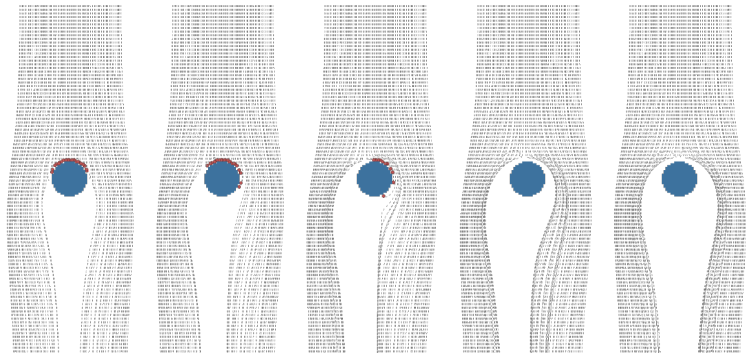

(a) $\alpha = 0°$ (b) $\alpha = 45°$ (c) $\alpha = 90°$ (d) $\alpha = 135°$ (e) $\alpha = 180°$

Figure 4.14: Particle trajectories around dipole charged fibers simulated with the uni-directionally coupled approach implemented in the software package GeoDict. Particles collided with the fiber surface are indicated in red. The angle of the dipole plane with respect to the inflow direction is varied between $\alpha = 0°$ and $\alpha = 180°$. The charge density ratio $\theta = 80$ is kept constant for all simulation runs. For better visualization, only 100 particle trajectories are plotted for each illustration (2000 particles are tracked to determine the collection efficiency).

The particle trajectories simulated with GeoDict are plotted in Fig. 4.14 for dipoles with different degrees of rotation. Dipoles with planes rotated more than $\alpha = 180°$ are omitted as they do not provide any added value, i.e, the trajectories are just mirrored on the z-axis of the fiber. To generate these plots, the highest charge density ratio $\theta = 80$ used in this work was chosen as the particle movements are most clearly differentiated in this case. The basic observations, though, also apply to lower charge densities. Furthermore, only 100 out of 2000 simulated particle trajectories are plotted for a clearer representation. Most particles evidently hit the fiber, i.e., the best separation is achieved, when the attractive part of the dipole is aligned towards the incoming particles ($\alpha = 0°$). However, also for the angles $\alpha = 45°$ and $\alpha = 90°$, many particle trajectories end at the fiber surface (deposited particles are marked in red). Only when the repulsive potential predominates at the front of the fiber, the particles are completely directed around the fiber. In this case, the equally polarized charges facing the particulate flow repel the particles

in such a strong way that they have no chance to adhere at the back of the fiber. The particles move too far away from the attractive part of the fiber to be drawn back against flow.

Figure 4.15 shows the separation efficiencies resulting from the particle trajectories as a function of the applied charge density ratio θ. In addition to the dipole charged fibers, the collection efficiency of the unipolarly charged fiber from Fig. 4.12 is included.

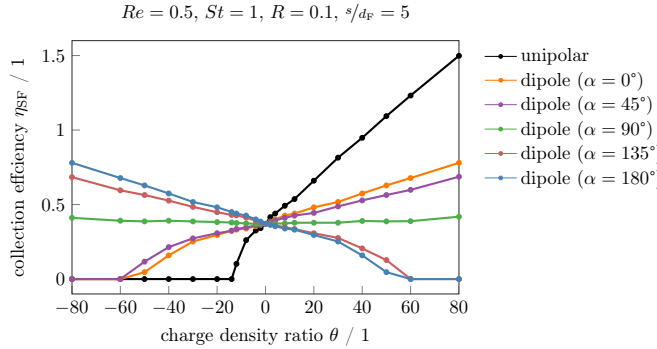

Figure 4.15: Single fiber collection efficiency η_{SF} depending on the charge density ratio. Different distributions of the charges on the fiber surface are compared with each other, i.e. unipolarly and dipole (with various rotation angles) charged fibers.

If only positive, i.e., attractive, charge density ratios are considered at first, the unipolarly charged fiber achieves the best results by far. As already apparent from the analysis of the particle trajectories, the rotation angle $\alpha = 0°$ leads to the highest separation among the dipoles. Although the deviation in collection efficiencies shrinks with decreasing charge differences between the fiber and particles, this statement retains its validity. For negative charge density ratios, the mirrored behavior for the collection efficiencies of dipole charged fibers is observed. The number of particles depositing on the unipolarly charged fiber, by contrast, quickly drops to zero due to strong repulsive forces exerted from the entire fiber surface. Dipole charged fibers have the advantage of attracting particles of both polarities. The effect appears to be most extreme for a rotation angle $\alpha = 90°$, for which the

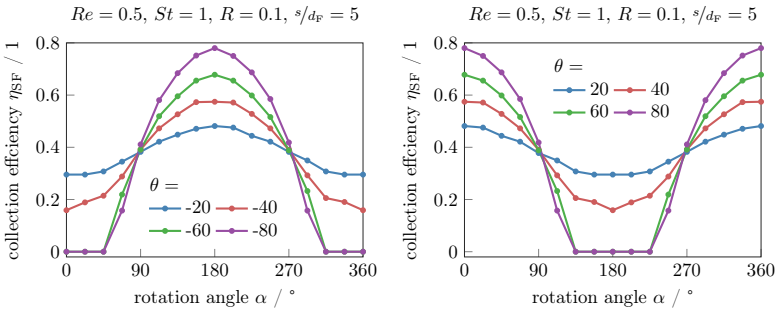

Figure 4.16: Influence of the dipole rotation angle α on the single fiber collection efficiency η_{SF} for negative (left) and positive (right) charge density ratios θ. The results are obtained using the software GeoDict.

collection efficiency is almost constant over all investigated θ.

The symmetry of the separation efficiencies for dipole charged fibers is also shown in Fig. 4.16, where the collection efficiencies are plotted over the rotation angle. On the left-hand side negative charge density ratios are shown. Since the particle charge density remains unchanged from previous investigations, the dipole with $\alpha = 180°$ results in the best filtration performance. For lower charge densities, the influence of the rotation angle decreases. This also corresponds to the claim that the rotation of a neutral fiber has no influence. The right-hand side of the figure shows the analog evaluation for positive charge density ratios. As expected, the curves are shifted by 180°.

4.3 Uni-Directional Simulation of Charged Fiber Arrays

Taking into account the periodic boundary conditions, the single fibers modeled so far have technically already represented fiber arrays. In this section, the single fibers in a periodic row are extended by further fiber layers. The resulting multifiber models have been primarily used in literature to enhance the fluid flow conditions with regard to pressure drop and interception mechanism [16, 31, 32, 66]. By the deflection of the streamlines through the first layer, the subsequent fibers

are exposed to different flow conditions. This in turn significantly changes the mechanical collection of airborne particles. Liu and Wang [66] observed a periodic flow field through uniform fiber arrays along the direction of flow. Due to the repetitive flow pattern, a small volume element is already representative.

In addition to the fluid flow field, the electrostatic field induced by charged fibers strongly affects the particle movements. This effect is already evident from the trajectories plotted around single fibers plotted in Fig. 4.11 and Fig. 4.14. This section focuses on the subsequent impact on the separation behavior of downstream fibers. The aim is to find out how the deflection of particles by the first fiber layer changes the deposition behavior of following fibers. In comparison to the single-layered structures investigated so far, the complexity of the charge configuration further increases. Even if the fiber array only consists of a few fibers, there is a magnitude of possible combinations of the surface charge distributions used so far, i.e., unipolarly and dipole charged fibers with different rotation angles. In order to determine the most efficient setup regarding filtration performance, different variations are modeled in this section. The results of the fiber arrays are expected to provide better transferability to real filter media than single fiber investigations.

4.3.1 Simulation Experiment Setup

The simulation experiment model consists of an arrangement of several cylindrical filter fibers. This implies an extension of the existing single fiber setup with additional fiber layers. All fibers are modeled with the same diameter and remain aligned normally to the direction of flow. Both plots in Fig. 4.17 show the same, basic arrangement of the fibers used in this section. For visualization reasons, only the part of the simulation domain containing the fibers is shown in z-direction. According to the simulation results from Fig. 4.3, inflow and outflow area are chosen sufficiently large in the simulation runs. The length of the line segment p introduced in Fig. 4.1 must be extended to the complete domain width ($p = s$) as every starting position can potentially lead to a deposition. Therefore, the number of simulated particles is set to 10.000 in this section.

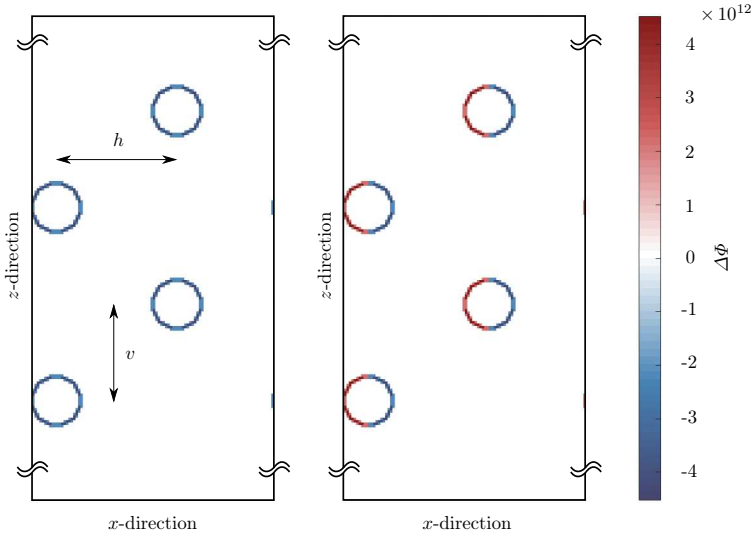

Figure 4.17: Cross section of a part of the voxel discretized simulation domain in the software GeoDict containing the experimental setup for fiber arrays with a unipolar charge distribution (left) and dipole charged fibers (right). The charge density $\xi_F = 4 \cdot 10^{-5}\,\mathrm{C/m^2}$ is analogues to Fig. 4.7 and Fig. 4.8. As before, the coloring of the voxels corresponds to the resulting values for $\Delta\Phi$ depending on whether one or two edges touch the fiber surface.

The used setup represents a so-called staggered array. In contrast to parallel arrays, the fibers from two successive layers feature a horizontal displacement h in addition to the vertical offset v. The ratio between horizontal and vertical distances between the fiber centers is arbitrarily set to $h/v = 5/4$ in this work. The boundary conditions for the air flow as well as the electrostatic field are chosen analogous to previous simulation studies in this chapter.

To generate the electrostatic field, various charge distributions and intensities on the fiber surfaces are considered. In addition to the completely neutral system, a unipolar charge distribution on all fibers is first analyzed. This corresponds to the setup depicted on the left-hand side of Fig. 4.17. Since the two leftmost fibers

are lined up precisely with the border of the periodic simulation domain, some adjacent surface voxels appear on the opposite side. As can be seen in the figure, these voxels are also assigned a value for $\Delta\Phi$. For the unipolarly charged fiber array, the particle separation behavior is compared for different charge density ratios θ.

In a subsequent step, dipole charged fibers are examined in terms of their filtration performances. Initially, all four dipoles are rotated equally as shown on the right-hand side of Fig. 4.17 for an exemplary rotation angle $\alpha = 90°$. Modeling is designed in such a way that each fiber is assigned its own plane, which distinguishes positive from negative electrostatic charges.

Finally, differently aligned dipoles are combined in one simulation setup. For this purpose, eight distinct cases are selected from a multitude of possible scenarios. The resulting $\Delta\Phi$-distributions for the mixed dipole setups are summarized in Fig. 4.18. The cases 1 to 4 are based on either horizontal or vertical dipole planes for all fibers. Both options are merged subsequently in the cases 5 and 6. Cases 7 and 8 use dipoles which are inclined at $\alpha = 45°$ and $\alpha = 135°$, respectively, to the incoming particulate flow.

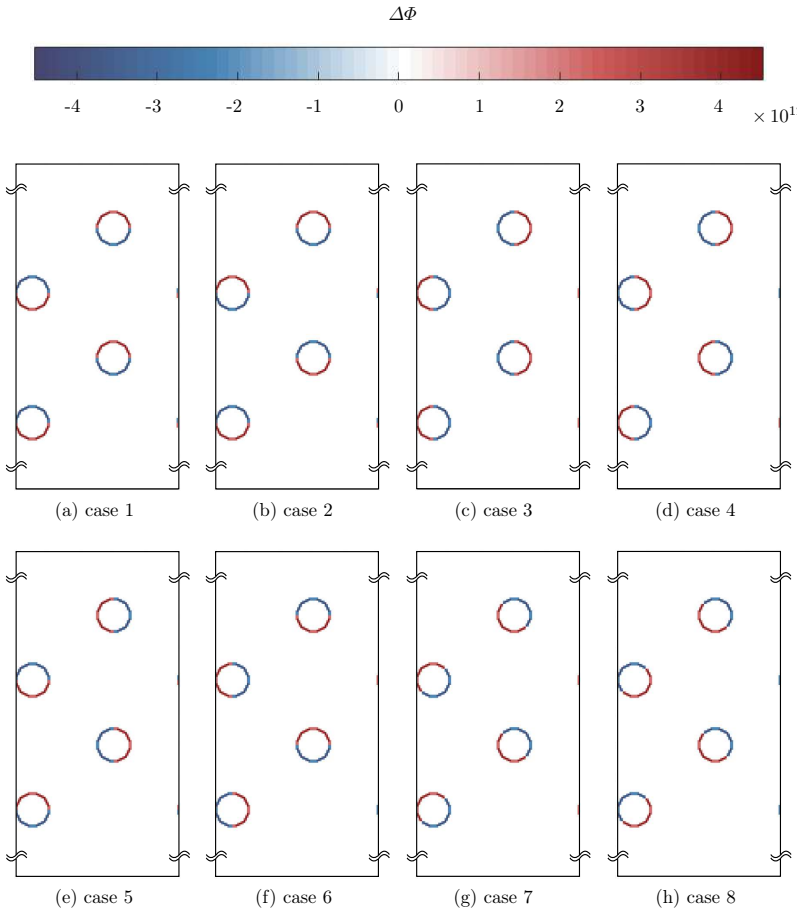

(a) case 1 (b) case 2 (c) case 3 (d) case 4

(e) case 5 (f) case 6 (g) case 7 (h) case 8

Figure 4.18: Cross sections of fiber arrays combining electrostatic dipoles of different rotation angles α in one simulation setup. The applied charge density $\xi_F = 4 \cdot 10^{-5}\,\mathrm{C/m^2}$ is analogue to previous illustrations. As before, the coloring of the voxels corresponds to the resulting values for $\Delta\Phi$ depending on how many edges touch the fiber surface.

4.3.2 Numerical Results for Mixed Fiber Charges

The movements of uniformly charged particles with $\xi_P = -1 \cdot 10^{-6}\,\mathrm{C/m^2}$ through unipolarly charged fiber arrays (see left-hand side of Fig. 4.17) are plotted in Fig. 4.19 for different charge density ratios θ. It is evident that the particle trajectories differ significantly from each other and, thus, lead to collections between zero and all particles. In the case of $\theta = -40$, the particles are repelled by equally charged fibers to such an extent that they all weave their way through the intermediate spaces. Already well before getting close to the first fiber, the particles are strongly deflected from the fluid streamlines. As a result, the particles are virtually pressed against the next fiber and come comparatively close to it. However, the repulsive potential of the second fiber is large enough to prevent the particles from colliding. Since the particles do not interact with each other in the applied uni-directionally coupled simulation approach, the resulting overlap of the particle trajectories has no further effect. As the charge intensity of the fibers decreases ($\theta = -20$), the electrostatic force of the second fiber is overcome, causing several particles to hit the fiber. Subsequently, the particle trajectories look very similar again, apart from a broader distribution. With further decreasing values for the charge density ratio ($\theta = -4$), an accumulation of particles occurs on all four fibers. The mechanical collection mechanism, i.e., inertia and interception, predominate over the electrostatic repulsion in this case. In the completely neutral system of fibers, a more symmetrical collection of particles on all fibers is achieved in x-direction. Due to the air flow conditions, most particles are still collected at the second fiber.

If particles and fibers are oppositely charged ($\theta > 0$), the number of separated particles significantly increases with θ. Hence, all injected particles are collected for $\theta = 60$ and $\theta = 80$. In all four attractive charge scenarios, the particle movements around the first two fiber layers differ substantially from those around the rear two fiber layers of the respective array. This is due to the fact that charged particles experience different forces when they linger between fiber layers or in the outflow area. In the middle of the fiber array, the particles are attracted equally from different sides. The additional force of the air flow in z-direction causes the particles to drift to the front side of the rear fibers. However, when the particles have already passed the fiber array, they can only adhere to the back of the rear fibers. In the case of $\theta = 20$ and $\theta = 40$, the attractive forces are partially not yet sufficient to

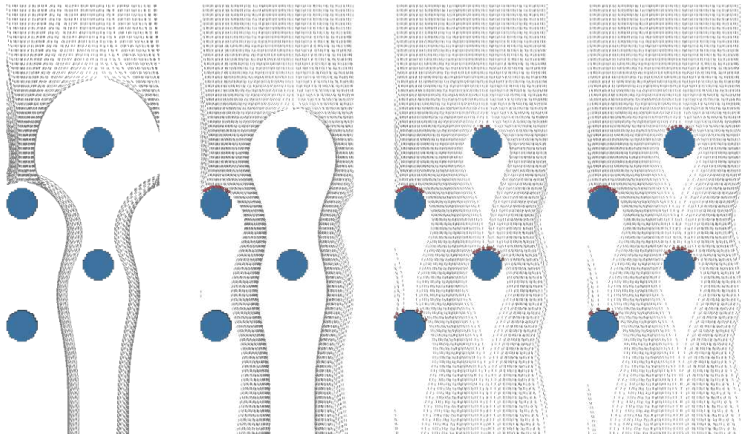

(a) $\theta = -40$ (b) $\theta = -20$ (c) $\theta = -4$ (d) $\theta = 0$

(e) $\theta = 20$ (f) $\theta = 40$ (g) $\theta = 60$ (h) $\theta = 80$

Figure 4.19: Particle trajectories around unipolarly charged fiber arrays simulated with the uni-directional coupling implemented in the software package GeoDict. Particles collided with a fiber surface are indicated in red. The charge density ratio is varied between $\theta = -40$, i.e., strongly repelling forces, and $\theta = 80$, i.e., highly attractive forces. For better visualization, only 100 particle trajectories are plotted for each illustration (10.000 particles are tracked to determine the collection efficiency).

achieve a full deposition. The particle deposition for the first two fibers is still restricted to the side of the fiber which is facing the incoming flow.

The effects outlined are also reflected in the measured collection efficiency of the fiber arrays η_{FA} plotted in Fig. 4.20. In contrast to previously discussed single fiber efficiencies, the collection efficiency of fiber arrays can no longer be calculated from a limiting trajectory. Therefore, the efficiency η_{FA} is obtained conventionally by dividing the number of collected particles ($N_{\mathrm{outlet}} - N_{\mathrm{inlet}}$) by the number of added particles at the inlet N_{inlet} according to Eq. (2.3). This calculation method results in a maximum collection efficiency $\eta_{\mathrm{FA,\,max}} = 1$.

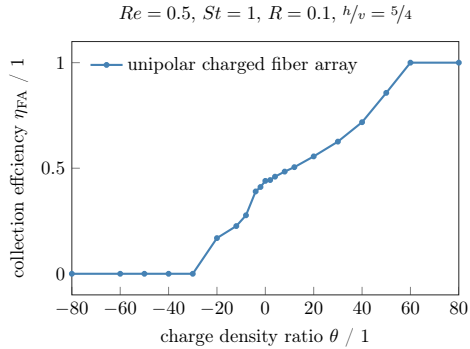

Figure 4.20: Collection efficiency η_{FA} for unipolarly charged fiber arrays depending on the applied charge density ratio θ. Both, particle size ($d_{\mathrm{P}} = 2\,\mu\mathrm{m}$) and particle charge density ($\xi_{\mathrm{P}} = -1 \cdot 10^{-6}\,\mathrm{C/m^2}$), are identical in all simulation runs.

The graph shows a non-zero collection of particles for charge density ratios $\theta \geq -30$. The collection efficiency then rises in a strictly monotonous manner with increasing θ. Compared to the single fiber efficiencies plotted in Fig. 4.12, the curve of the collection efficiencies for $\theta < 0$ is not as smooth. In addition, the plot shows a bend in the measured collection efficiency during the transition to positive charge density ratios. Thereafter, the separation efficiency increases more evenly until all particles are finally trapped by the fiber array at $\theta = 60$.

In order to get a first impression of the dipole charged fiber arrays (see right-hand side of Fig. 4.17), the propagation of the emerging potentials is plotted in Fig. 4.21. The applied surface charge density $\xi_F = 4 \cdot 10^{-5}\,\mathrm{C/m^2}$ is constant for all presented scenarios, only the rotation angle α of the dipoles is varied. The four planes of the fibers within one array are each rotated to the same degree.

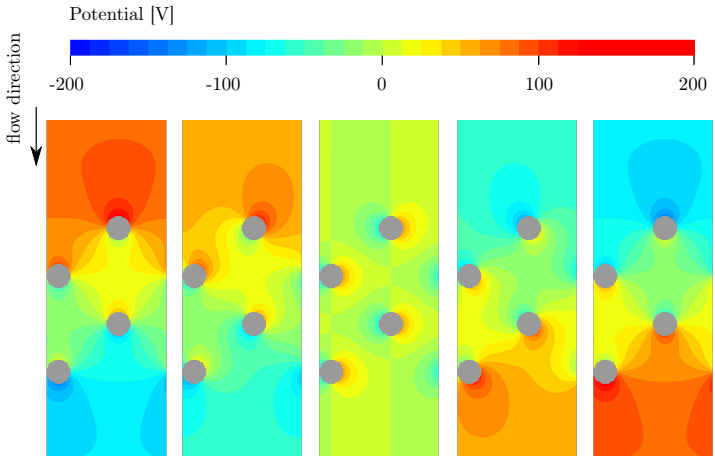

Figure 4.21: Electrostatic potential Φ induced by fiber arrays with different electrostatic charge configurations. All fibers in one setup are charged with dipoles rotated by the same amount. The surface charge density of all depicted fibers is $\xi_F = 4 \cdot 10^{-5}\,\mathrm{C/m^2}$.

Apparently, the dipole planes arranged perpendicular to the incoming inflow, i.e., $\alpha = 0°$ and $\alpha = 180°$, are rather exploiting the extremes of the potential scale. In contrast, the superposition of the electrostatic potentials induced by vertically aligned dipoles ($\alpha = 90°$) leads to a mutual compensation such that the total potential is in a narrow range around $\Phi = 0\,\mathrm{V}$ for the complete area around the fiber array. Therefore, the vertical arrangement is bound to result in a more constant particle collection efficiency for varying charge density ratios, whereas the horizontal alignment will tend to higher discrepancies between small and large values for θ.

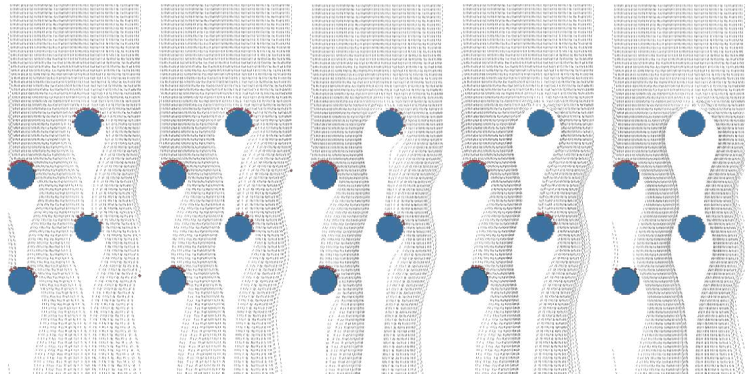

(a) $\alpha = 0°$ (b) $\alpha = 45°$ (c) $\alpha = 90°$ (d) $\alpha = 135°$ (e) $\alpha = 180°$

Figure 4.22: Particle trajectories around dipole charged fiber arrays simulated with the uni-directional coupling implemented in the software package GeoDict. Particles collided with a fiber surface are indicated in red. The angles of all dipole planes in one setup are varied between $\alpha = 0°$ and $\alpha = 180°$ with respect to the flow direction. The charge density ratio $\theta = 80$ is kept constant for all simulation runs. For better visualization, only 100 particle trajectories are plotted for each illustration (10.000 particles are tracked to determine the collection efficiency).

Consequences of the different dipole orientation are explained more specifically by means of the particle trajectories presented in Fig. 4.22. The more directly the attractive halves of the fibers point towards the incoming particulate flow, the more particle trajectories end at a fiber (deposited particles are marked in red). Thus, most particles are separated for $\alpha = 0°$. However, even for $\alpha = 180°$, i.e., when the repulsive potential is directly facing the inlet, several particles hit the fibers. Contrary to conjecture, these particles deposit on the front side of the fiber despite the rejecting potential. Due to the intense repulsion through the first fiber layer, the particles have no chance to escape from the second fiber as well. The combination of air flow and electrostatic field causes particles to come into contact only with the two fibers arranged on the left-hand side. At the middle rotation angles, the lateral deposition of particles on the fibers is clearly noticeable. The rejection of the particles on the opposed face is also visible.

Finally, Fig. 4.23 provides the resulting collection efficiencies of the equally aligned dipole charged fiber arrays for negative as well as positive charge density ratios.

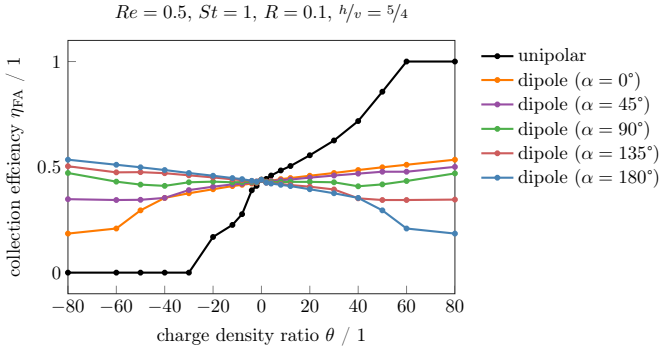

Figure 4.23: Collection efficiency η_{FA} for dipole charged fiber arrays depending on the applied charge density ratio θ. All fibers in one setup have the same respective orientation. Both, particle size ($d_P = 2\,\mu m$) and particle charge density ($\xi_P = -1 \cdot 10^{-6}\,C/m^2$), are identical in all simulation runs.

In principle, the curves for different rotation angles show the same, symmetrical behavior as for the single fiber analysis plotted in Fig. 4.15. However, the dispersion of collection efficiencies between the different angles is much smaller. For the extreme charge conditions ($\theta = \pm 80$), the maximum and minimum collection efficiencies are approaching from both sides.

As mentioned above, various dipole rotations are combined with each other in the final step. Referring to the experimental setups presented in Fig. 4.18, the spread of the arising potentials is plotted in Fig. 4.24. In the visual comparison of the diagrams, the cases 1, 2 and 8 stand out slightly. Relatively high potentials occur in the interspaces of the fibers for the cases 1 and 2. In case 8, by contrast, the high potential expands in the direction of the incoming particulate flow. With all other potentials, no distinct peaks occur, the potentials range around $\Phi = 0\,V$.

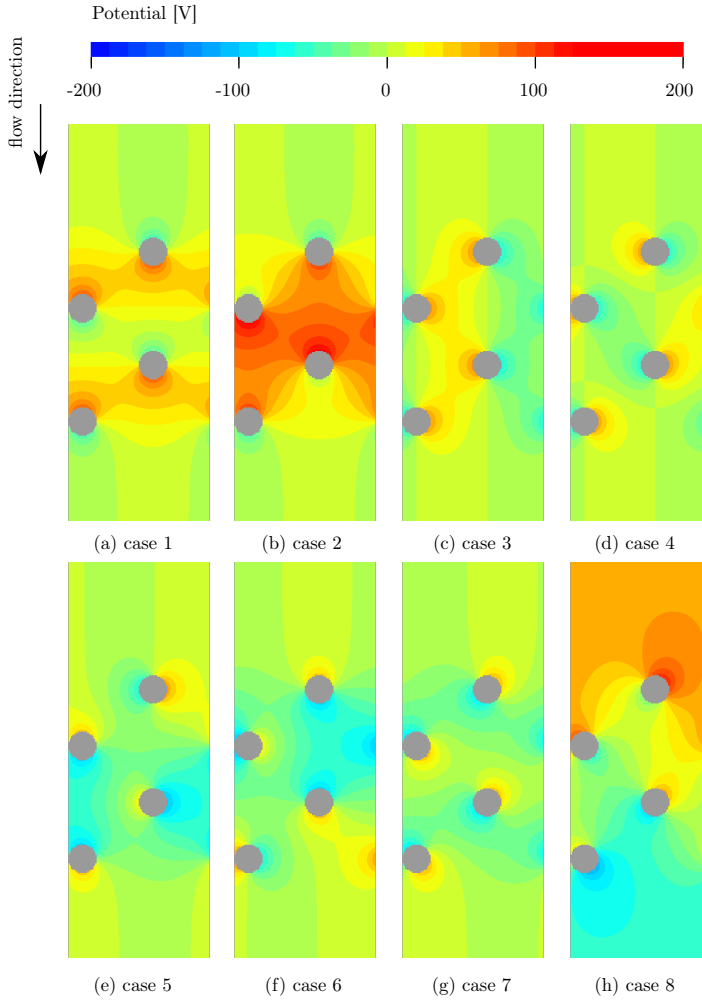

Figure 4.24: Electrostatic potential Φ induced by fiber arrays with mixed orientations for dipole charged fibers. The applied surface charge density to all depicted fibers is $\xi_F = 4 \cdot 10^{-5}\,\mathrm{C/m^2}$.

Analogous to the previous investigations, the corresponding particle trajectories around the fiber arrays are plotted in Fig. 4.26 at the end of this section. The illustrations show a relatively low separation for the first two scenarios. At the first fiber layers, no particles come into contact at all. By contrast, case 8 indicates a high degree of collection. All other plots, however, do not deviate excessively in terms of deposited particles.

Finally, the resulting collection efficiencies for fiber arrays with mixed dipole rotations are plotted in Fig. 4.25. As already deduced from the potentials and the trajectories, case 8 is most suitable for the collection of particles at charge density ratios $\theta > 0$. The cases 1 and 2 represent good filter models for negative charge density ratios.

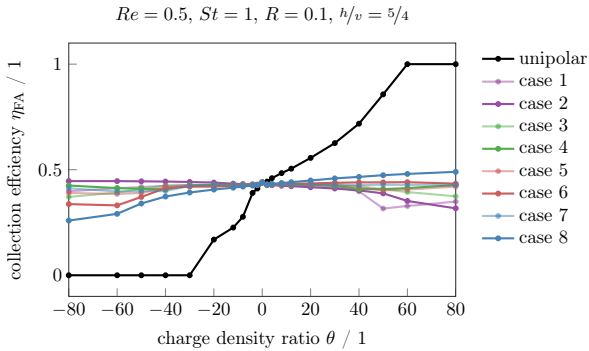

Figure 4.25: Collection efficiency η_{FA} for fiber arrays with combined dipole orientations depending on the applied charge density ratio θ. Both, particle size ($d_P = 2\,\mu m$) and particle charge density ($\xi_P = -1 \cdot 10^{-6}\,C/m^2$), are identical in all simulation runs.

What is also becoming apparent is that the collection efficiencies for mixed dipole rotations are even closer together. Therefore, it is concluded that the orientation of dipoles in fiber arrays plays only a minor role compared to that of single fibers. The additional fiber layers lead to an almost constant collection efficiency for all fiber charge intensities investigated. For even higher charge differences between fibers and particles, however, a more pronounced influence is expected.

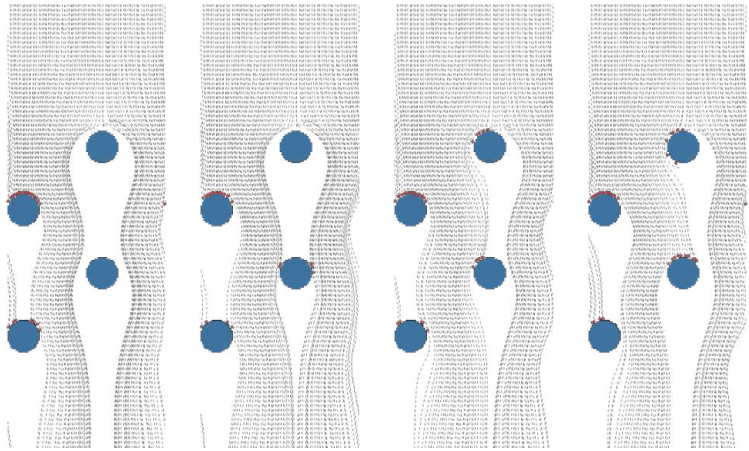

(a) case 1 (b) case 2 (c) case 3 (d) case 4

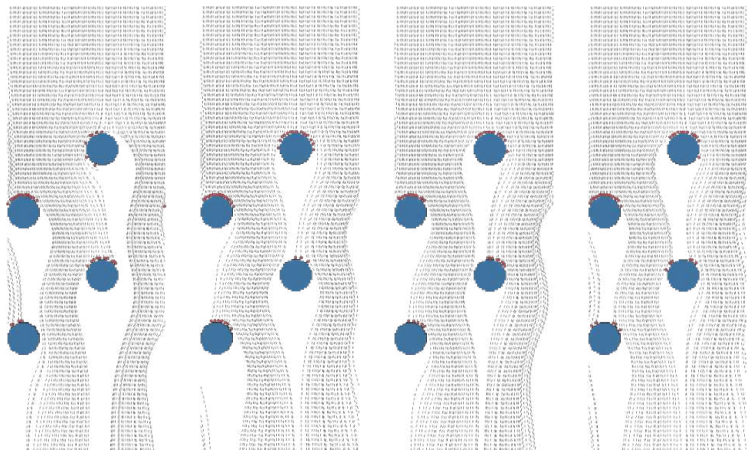

(e) case 5 (f) case 6 (g) case 7 (h) case 8

Figure 4.26: Particle trajectories around fiber arrays with mixed dipole orientations simulated with the uni-directionally coupled modeling approach implemented in the software package GeoDict. Particles collided with a fiber surface are indicated in red. The charge density ratio $\theta = 80$ is kept constant for all simulation runs. For better visualization, only 100 particle trajectories are plotted for each illustration (10.000 particles are tracked to determine the collection efficiency).

4.4 Summary

The common scenario of particle collision with a single fiber was used to verify the fundamentally new fully-coupled simulation approach in the field of air filtration. The corresponding simulation studies were limited to mechanical collection mechanisms, which can also be reproduced with the uni-directionally coupled status quo approach. Preliminary investigations demonstrated that the required inlet and outlet lengths differ for the one-way or four-way coupled simulation approaches. These deviations are explained by the different applied boundary conditions for the initialization of the air flow field. Based on the knowledge gained, good agreement ($\delta_{\mathrm{SF}} \leq 3.4\,\%$) was achieved for the simulated single fiber collision efficiencies with different coupling intensities. The comparison with published data resulted in a maximum relative error of only $\delta_{\mathrm{SF}} = 5\,\%$ over the complete investigated ranges of dimensionless fiber offset, Reynolds and Stokes numbers. The fully-coupled system can thus be employed to simulate further, more complex filtration scenarios.

In the second part of this chapter, the influence of pure Coulomb interactions between single fibers and particles was investigated. For this purpose, the standard uni-directionally coupled approach was ideally suited. The already implemented unipolar charge distribution on fiber surfaces has been extended to dipole charged fibers. Resulting simulations showed that by varying the fiber charge distribution and intensity, any single fiber collection efficiency can be achieved. The extension to a multifiber model demonstrated the complexity due to numerous possible combinations for the unknown electrostatic parameters. Already from the propagation of the electrostatic potential of fiber arrays it was possible to draw conclusions about the separation efficiency. The following simulation studies revealed that the charge distribution on fiber arrays leads to smaller scattering widths of the collection efficiency compared to single fibers.

The simulation studies provide indications as to which charge distributions are well suited to achieve reasonable filtration performances. How to specifically apply the electrostatic charges to the fibers or the filter medium, however, remains an open question. Even how to measure charge intensities and distributions in the three-dimensional fibrous structures can not be answered. Computer-aided simulation is, therefore, the only tool to determine such detailed influences of electrostatics on the filtration efficiency.

Chapter 5

Numerical & Experimental Analysis of Particle Dynamics

So far, the fundamentally new fully-coupled simulation has only been used to reproduce the known mechanical filtration mechanisms, which can also be modeled with the status quo uni-directional coupling approach. The simulation results obtained in Chapter 4 verified the new modeling approach with regard to its application to filtration processes. In this chapter, the major advantages of the four-way coupled simulation, involving the underlying physical models presented in Chapter 3, are fully exploited for the first time.

Complex particle-particle interactions in the inflow area of filter media are taken into account in Sec. 5.1. The aim of this fully-coupled simulation is to reveal the extent of electrostatic particle-particle agglomeration and its subsequent impact on the overall filtration efficiency. The extremely low particle concentration from laboratory experiments requires a significant enlargement of the simulation domain compared to the single fiber model presented in Fig. 4.1. Otherwise, the number of particles in the simulation domain is not representative. At the same time, a high resolution of the LBM mesh is necessary to precisely calculate the background air flow field around filter fibers. However, the computationally intensive four-way coupled simulation does not allow the combination of a large domain and a high resolution. For this reason, the filter medium is omitted in a first step such that the focus is completely shifted to the particulate inflow area.

The most important and challenging element of the simulation studies is the dust specification. This pre-processing step includes the declaration of a realistic particle

size and charge distribution. The variation of both distributions over simulation time is one point of emphasis in the subsequent evaluation.

In Sec. 5.2, the influence of the air flow field in the test facility (described in Sec. 2.2.1) on particle dynamics is investigated. On the one hand, the aim of this simulation study is to find out whether a homogeneous mixing of all particle size classes at the inlet of the test channel is ensured. If the mixing is not sufficient, an unevenly dispersed particle distribution will hit the particle measuring instruments as well as the filter medium itself and, thus, affect the measured collection efficiency. On the other hand, particle extraction for the determination of particle size distributions takes place centrally in the test channel. It is to be examined whether the sampling position has an impact on the measured collection efficiencies due to flow characteristics. Since the analysis is concerned exclusively with fluid flow effects, a uni-directionally coupled simulation is sufficient at this point. Due to the complexity of the test channel geometry, the commercial CFD software tool ANSYS Fluent is applied.

Experimental investigations complement the simulation studies of this chapter. Section 5.3 contains the experimental analysis of particle dynamics in the empty test channel, i.e., with no filter medium inserted. Different variations of the modular filter test rig introduced in Sec. 2.2 provide information about various factors influencing the measured collection efficiency. Analogous to the simulation studies of this chapter, particular focus is on the influence of electrostatic particle charges.

5.1 Fully-Coupled Simulation of Electrostatic Particle-Particle Interactions

To take full advantage of the four-way coupled simulation approach, the interconnection of three components is required: short-range particle interactions, long-range electrostatics and hydrodynamics. Simulating the particulate flow through cabin air filter media requires exactly this combination of subsystems. Modeling molecular dynamics potentials and the bi-directional coupling with the background air flow field have already been introduced in Sec. 3.4. This section, by contrast, focuses on applying the implemented models to particle dynamics of realistic filter test dust. The associated simulation experiment setup, including the choice of boundary con-

ditions and simulation input parameters, is outlined first. Subsequently, numerical results of emerging agglomeration processes are discussed in detail.

5.1.1 Simulation Experiment Setup

As mentioned above, the complex filter structure and the resulting computationally elaborate particle deposition process are omitted in the first instance. Instead, the focus of the simulation study is on electrostatically induced particle dynamics in the inflow area only. In a prior publication [42], this simulation setup was already used to measure simulation runtimes and perform scaling experiments. The simulation domain and the related boundary conditions are presented first. Thereafter, the procedure for the selection of appropriate simulation input parameters is described.

5.1.1.1 Simulation Domain & Discretization

Figure 5.1 visualizes the general restriction of the simulation domain to the inflow area of filter media. The left part shows the simulated air flow field through a rather simple and open-pored cabin air filter medium. In addition, domain dimensions that are typically used for the uni-directionally coupled simulation approach implemented in the software package GeoDict are given.
These dimensions result in an inflow volume element of $V_{\text{inflow}} \approx (1024 \times 1024 \times 540)\,\mu\text{m}^3$. With the dust concentration $c_{\text{P}} = 7.5 \cdot 10^{-5}\,\text{kg/m}^3$ used in laboratory experiments, only a single particle with $d_{\text{P}} = 3.1\,\mu\text{m}$ fits into this domain. However, particles do not interact with each other in the uni-directionally coupled modeling approach. Hence, the particle concentration can be arbitrarily increased in order to simulate the collection efficiency with a meaningful amount of particles (and covering the majority of possible starting positions).

The right-hand side of Fig. 5.1 illustrates the three different domain sizes deployed in the fully-coupled simulation approach implemented in the software package ESPResSo. The largest domain used in this work is a cube with an edge length of $l_{\text{domain}} = 6400\,\mu\text{m}$. The corresponding volume is thus more than 450 times bigger than V_{inflow} mentioned above. Using a realistic particle size distribution, which will be dealt with in more detail in Sec. 5.1.1.3, enables a capacity of more than 2000 particles for the simulation with the fully-coupled modeling approach. The simulation of such large systems is only possible at a coarse resolution, which is

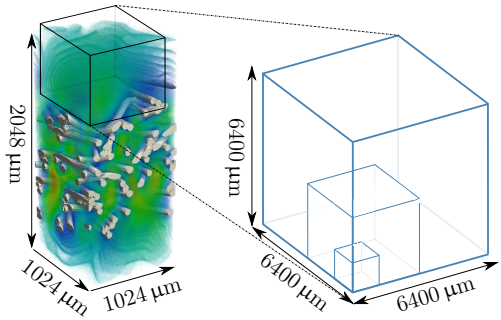

Figure 5.1: Air flow through an xCT-based model of an excerpt from a open-pored cabin air filter medium (left). The plotted flow field is calculated with the software package GeoDict using standard dimensions, which allow a feasible runtime. In comparison, the volume of the largest of three selected simulation domains for the software package ESPResSo (right) is more than 450 times bigger than the inflow area applied in GeoDict. The image is adapted from work published prior to this thesis [42].

sufficient as geometrically complex fiber structures are neglected. In the following simulation studies, a grid spacing of $a = 20\,\mu\text{m}$ for LBM is applied to the cubic simulation domains.

5.1.1.2 Simulation Procedure & Boundary Conditions

In a first, preparatory step, a uniform flow field with periodic boundary conditions is generated in the cubic simulation domain. To initialize the flow, a defined force is applied to each Lattice-Boltzmann cell in the direction of flow. This way, the velocity of the air flow field steadily increases. As soon as the target velocity of $v_{\text{air}} = 4.2\,\text{cm/s}$ (from laboratory testing) is reached, the external forces are withdrawn. In the next step, particles are randomly added to the initial flow field. When distributing the particles, there is a minimum distance between particles. Particles in contact ($|\mathbf{r}| = \sigma_{\text{Hz}}$) would result in direct a adhesion due to the harmonic bond potential becoming effective (see Sec. 3.2.1). Thus, the corresponding particles would directly form an agglomerate regardless of their charge polarities. An overlapping of particles during their addition to the flow field would lead to disproportionally strong repulsive forces through the Hertzian potential.

Depending on the applied time step size, the resulting particle acceleration could lead to instabilities in the simulation.

After proper particle addition, the flow field is only influenced by interaction with the particles. With this final experimental setup, particle dynamics are simulated for ten (real) microseconds. Periodic boundary conditions in each direction are also applied for both short-range and long-range particle-particle interactions. In addition to the force-driven initial flow field generation, the influence of applying Dirichlet boundary conditions with the air velocity v_{air} at the inlet and outlet is analyzed.

5.1.1.3 Simulation Input Parameters for Particle Sampling

The simulation of realistic dust particle dynamics requires the specification of accurate input distributions. To begin with, the particle size distribution, which also determines the number of particles (at a given particle concentration), must be defined. Each particle must then be assigned a size-dependent electrostatic charge. Since no exact data are available for the ISO fine test dust used in this work, the influence of different parameter variations is analyzed at this point. Finally, the particles are randomly added to the simulation domain. The procedure for particle sampling described in this section follows the work published prior to this thesis [90].

Particle Size Distribution. The particle size distribution specified in the ISO standard [44] serves as a basis for these simulation runs. The probability density function q_0 plotted truncated in Fig. 5.2 (red) contains particles with diameters up to $d_{\mathrm{P}} = 176\,\mu\mathrm{m}$. For reasonable simulations, however, minor adaptions for very small and large particles are necessary. Required restrictions result from the combination of a limited domain size and a low dust concentration prescribed from laboratory test conditions. In order to nevertheless achieve a meaningful number of particles in the system, the focus is set on the most frequently occurring particle size classes. First of all, uniformly distributed discrete particle sizes are selected. Since heavy particles would fill the simulation domain too quickly, particles larger than $d_{\mathrm{P}} = 5.73\,\mu\mathrm{m}$ are omitted. For instance, a single particle with $d_{\mathrm{P}} = 25\,\mu\mathrm{m}$ in a simulation domain measuring $(6400 \times 6400 \times 6400)\,\mu\mathrm{m}^3$

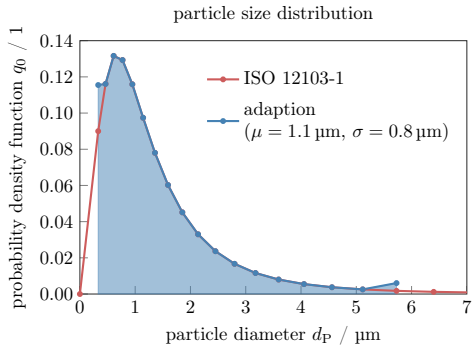

Figure 5.2: The plotted probability density function q_0 is the basis for the particle size distributions used in this work. It is based on the ISO standard [44] of the corresponding A2 fine dust. Particle smaller than $d_P = 0.33\,\mu m$ and larger than $d_P = 5.73\,\mu m$ are omitted and their probabilities are added to the two outer particle diameters to preserve $\sum q_0(d_P) = 1$. The blue dots represent the discrete diameters that the particles can take in the simulation.

would already lead to a particle concentration of $c_P = 8.3 \cdot 10^{-5}\,kg/m^3$, which is already above the target concentration $c_P = 7.5 \cdot 10^{-5}\,kg/m^3$ of this work. In order to keep the overall probability at $\sum q_0(d_P) = 1$, the individual probabilities of the discarded particle sizes $d_P > 5.73\,\mu m$ are added to the largest considered particle diameter. Since discrete particle diameters are needed as input parameters, particles smaller than $d_P = 0.33\,\mu m$ are also omitted. Again, the probability of this smallest considered particle size ($d_P = 0.33\,\mu m$) is increased accordingly. The final particle size distribution applied to the fully-coupled simulation is also plotted in Fig. 5.2 (blue). The distribution yields a mean particle diameter $\mu = 1.1\,\mu m$ with a standard deviation of $\sigma = 0.8\,\mu m$.

Particle Charge Distribution. In contrast to the particle size distribution, choosing appropriate electrostatic charge parameters for each particle is significantly more complex. For one thing, the electrostatic particle charge can hardly be determined experimentally, and, secondly, it depends on various environmental factors such as temperature and humidity. Therefore, published data are referred to

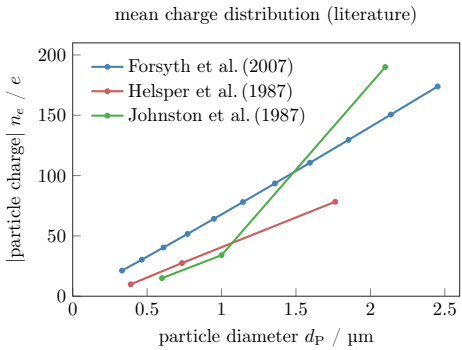

Figure 5.3: Published data for particle mean charge distributions over different particle size classes. Forsyth et al. [34] use a fluidized bed generator to disperse the Arizona test dust. Helsper and Mölter [39] use the right, rotating brush generator (RBG), but determine the charge distribution of pure quartz. Johnston et al. [46] use the combination of the fluidized bed generator with pure quartz.

as a general basis in this work. Figure 5.3 summarizes empirical and semi-empirical data for the mean particle charge within different particle size classes collected from literature. The three data sets differ in the applied dispersion method as well as in the test dust of interest. However, all three curves show a characteristic sharp increase of the particle charge intensity n_e (number of elementary charges) with rising particle diameters. The measured data from Johnston et al. [46] is the only curve showing a change in the gradient over the displayed particle size range. Amongst other mechanical dispersers, they used a fluidized bed generator and measured the resulting mean particle charge of pure quartz (only 69 % to 77 % of ISO fine dust consist of quartz [44]). The curves by Helsper and Mölter [39] and Forsyth et al. [34] both rise approximately linearly, but with different gradients. Helsper and Mölter [39] are the only reference using a rotating brush generator (RBG 1000) equivalent to the experimental investigations in this work. However, they also determined the mean charge distribution of pure quartz and not ISO fine dust. Forsyth et al. [34] used Arizona road dust, but dispersed the particles with a fluidized bed generator. Since no suitable published data are available for

the combination of the RBG disperser and ISO fine dust, the influence of different charge parameters is analyzed at this point. The selected parameter sets are based on the only semi-empirical formula, provided by Forsyth et al. [34]. They propose a correlation between the median number n_e of elementary charges and particle diameter in µm

$$n_\mathrm{e} = a\, d_\mathrm{P}^{b} \tag{5.1}$$

for a particle size range of $d_\mathrm{P} = 0.26\,\mu\mathrm{m}$ to $2.6\,\mu\mathrm{m}$ with the gradient $a = 67.8\,[\pm 3.85]$ and the exponent $b = 1.05\,[\pm 0.05]$. In this work, the expression is extended to larger particles as no other data is available. Furthermore, the influence of the gradient a on particle dynamics and the resulting degree of agglomeration is analyzed. Deviating from their formula, however, lower gradients are selected in order to better approximate the measured values from Helsper and Mölter [39] using a RBG disperser. Figure 5.4 finally shows the three mean particle charge distributions applied in this work.

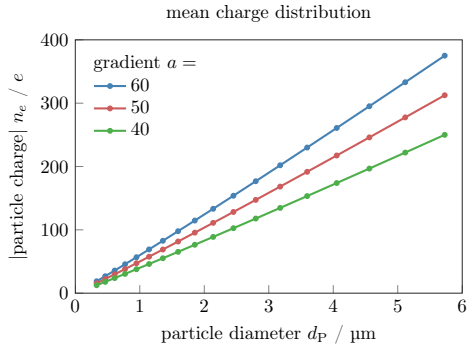

Figure 5.4: Particle mean charge distributions over different particle size classes applied in this work. All three distributions are based on the semi-empirical formula proposed by Forsyth et al. [34], but are extended to larger particle diameters and differ in the selected gradient a. The adapted charge distributions have already been presented prior to this thesis [90].

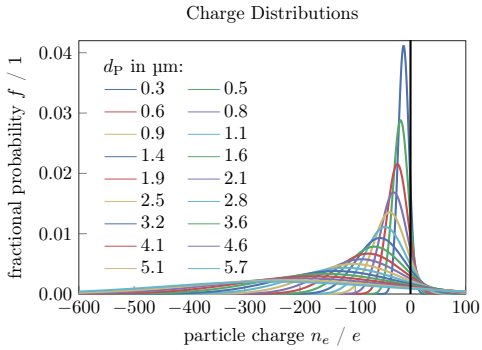

Figure 5.5: Calculated particle charge distributions within each discrete particle size class depicted in Fig. 5.2. The plotted Gaussian distributions follow the respective expected values from Fig. 5.4. The standard deviations are chosen such that 10 % of each particle size are positively charged. The image is adapted from Schober et al. [90].

In addition to the mean charge distributions, the electrostatic charge variation within each particle size must be dealt with. Since no exact information is available, Gaussian distributions are simplistically assumed at this point. The expected values μ_{charge} for the respective particle sizes correspond to the mean particle charges shown in Fig. 5.4. Based on the findings of Forsyth et al. [34] (for the dispersion of quartz with a fluidized bed generator), about 10 % of the dust particles in the system are positively charged. The standard deviation σ_{charge} for the Gaussian distributions is chosen such that this finding is replicated. The resulting curve for each discrete particle size is plotted in Fig. 5.5. Since the specified percentage of positively charged particles was determined for another system of disperser and test dust, the value is not necessarily transferable. Therefore, the influence of different imbalances, i.e., 5 %, 10 % and 20 % of the particles having a positive charge, is additionally examined.

Particle Sampling. The final configuration of simulation input parameters consists of two consecutive steps, in which discrete values are drawn randomly out of the distributions (Fig. 5.2, Fig. 5.4 and Fig. 5.5) introduced above. In the

first step, particle sizes are drawn from the adapted size distribution plotted in Fig. 5.2 until the target concentration of $c_\mathrm{P} = 75\,\mu\mathrm{g/m^3}$ for a defined simulation domain size is reached. By repeating the drawing several times, different numbers of particles are generated for the same system. For each simulation study in this section, three different particle size distributions are drawn in order to achieve a certain statistical soundness. This is intended to simulate any unsteadiness that may occur during the dispersion of particles in experimental testings. Exemplary, the three distributions drawn for a domain size of $(3200 \times 3200 \times 3200)\,\mu\mathrm{m^3}$ are plotted in Fig. 5.6. As soon as several large (heavy) particles are drawn, such as in the third distribution plotted, the total number of particles is considerably reduced. The amount of particles for the given domain size varies between 234 particles and 623 particles in the three presented distributions.

In the second step, an electrostatic charge has to be assigned to each particle drawn from the size distributions. The charge intensity for each particle is again randomly drawn from the corresponding Gaussian distributions plotted in Fig. 5.5. For each particle size distribution drawn so far, three different charge distributions are determined. This way, the statistical scattering from dispersing the test dust in the experiments is replicated again. The randomly drawn particle charge distributions according to the three size distributions from Fig. 5.6 with 10 % positively charged particles are presented in Fig. 5.7. In total, the sampling procedure results in nine different particle sets for one simulation setup. The initial positions of all particles of a set are randomly distributed in the simulation domain. If a particle set is used a second time, the identical particle positions from the first draw are reused.

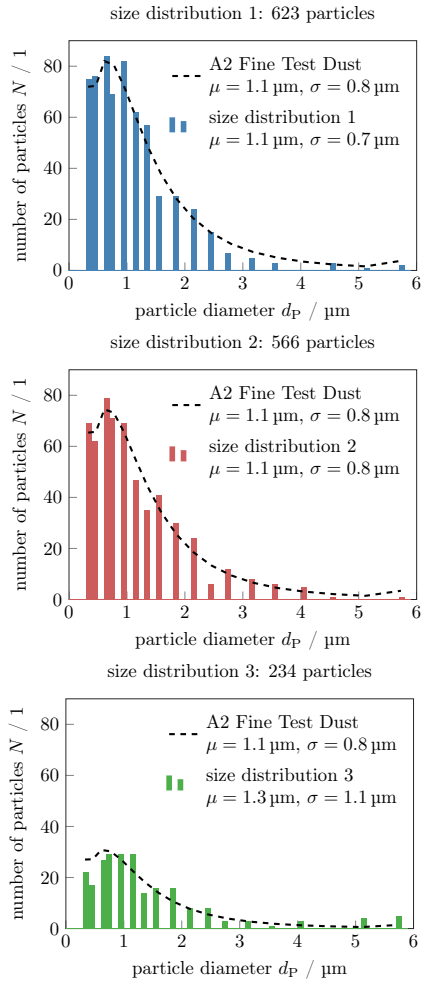

Figure 5.6: Three randomly drawn particle size distributions based on the ISO fine dust distribution plotted in Fig. 5.2. An equal bar width is assigned to each discrete particle diameter available. The domain size of $(3200 \times 3200 \times 3200)\,\mu m^3$ and the particle concentration of $75\,mg/m^3$ are prescribed for the particle sampling. The dashed lines correspond to the reference distribution for the respective total number of particles.

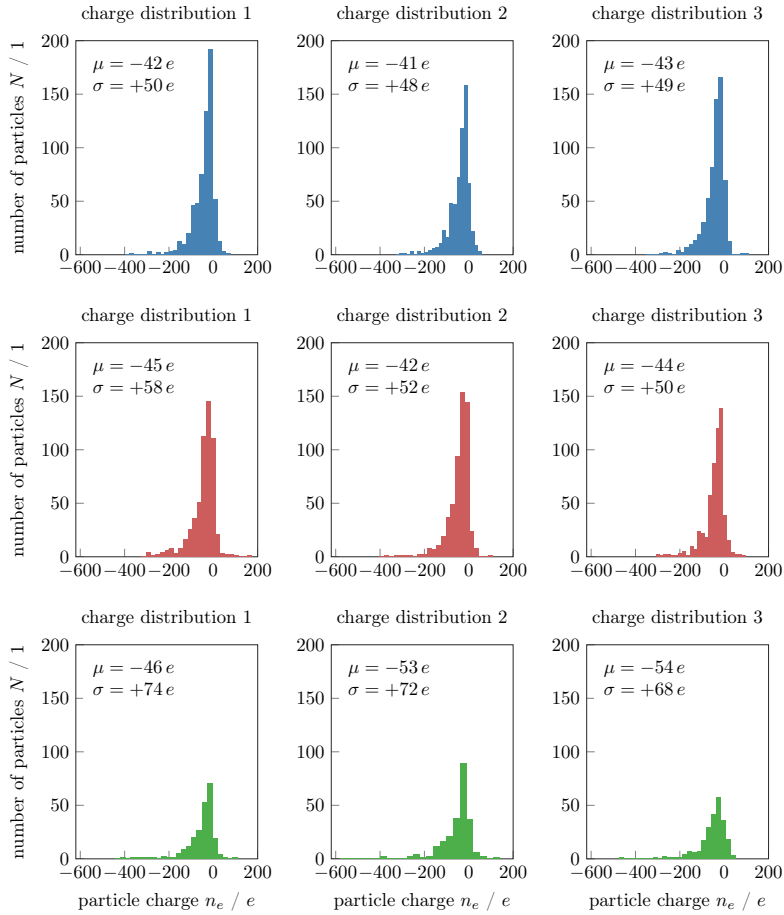

Figure 5.7: Three randomly drawn particle charge distributions for each of the three particle size distributions (blue, red, green) presented in Fig. 5.6. In total, this results in nine different particle sets for the simulation runs with the domain size $(3200 \times 3200 \times 3200)\,\mu\mathrm{m}^3$ and the particle concentration $c_\mathrm{P} = 75\,\mathrm{mg/m}^3$. In the plots, μ and σ denote the mean particle charges and the associated standard deviations. The values drawn from the continuous Gaussian distributions are divided into bars of equal width.

5.1.2 Numerical Results

Based on the simulation domain measuring $(3200 \times 3200 \times 3200)\,\mu m^3$ and the dust particle sets specified in Fig. 5.6 and Fig. 5.7, some general numerical results are presented at first. The snapshots in Fig. 5.8 give a first insight into the simulation of electrostatic particle-particle interactions. They show the randomly distributed particles (in tenfold magnification) at the beginning of the simulation and the evolved distribution after $t = 10\,\mu s$.

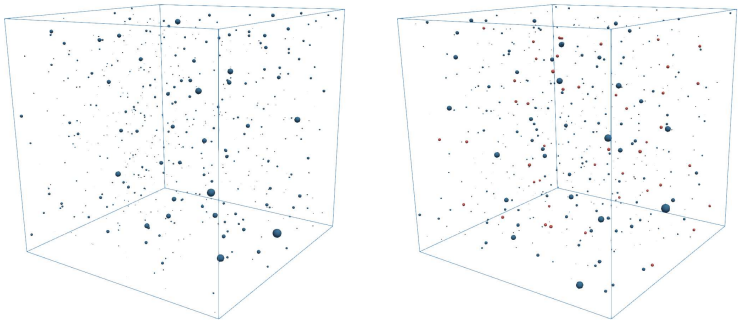

(a) $t = 0\,\mu s$ (b) $t = 10\,\mu s$

Figure 5.8: Simulation snapshots at the beginning (left) and the end (right) of the simulation run using the first drawn size and charge distribution (623 particles). The dust particles (blue) are shown in tenfold magnification. Since agglomerated particles can not be detected with the naked eye, they are highlighted in red.

At the first glance, no visual changes in the particle pattern are observable. Nevertheless, at the end of the simulation, many agglomerated particles (highlighted in red) are present. The distribution of the virtual sites over the entire domain indicates that many, presumably small agglomerates are formed. A precise analysis of the agglomeration process on the basis of numbers and facts is given below.

Figure 5.9 demonstrates how the merging of several particles due to electrostatic attraction changes the number of dust particles. The relative particle number N_{rel} is obtained by dividing the current number of particles by the initial number of particles. For each size distribution, the averaged value over the three simulation

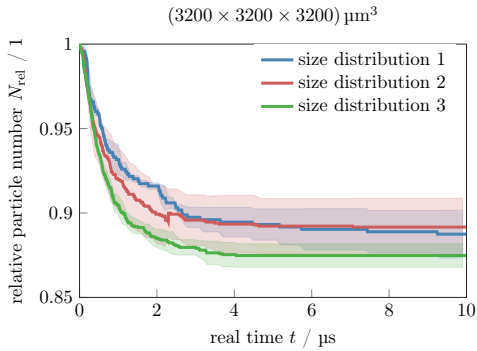

Figure 5.9: Relative particle number N_{rel} (current number of particles / initial number of particles) over simulation time. The solid lines indicate the average values over three simulation runs (corresponding to three particle charge samples) per size distribution sample, the light areas the respective standard deviations. This evolution of the relative particle number has already been presented prior to this thesis [90].

runs with different charge configurations is plotted over time. The plot reveals a high degree of agglomeration and, thus, very strong particle-particle interactions within the first two microseconds. In this very short time, the total number of particles is on average reduced by 11.6 % for the nine simulation runs. The percentage is comparable to the proportion of positively charged particles (10.1 %) originally added to the system. In conclusion, it is assumed that oppositely charged particles collide with each other and form larger agglomerates until only one polarity is left. Therefore, some positively charged particles have several negatively charged particles attached to them. The rapid decrease in the overall number of particles implies that Coulomb forces clearly dominate over the drag forces induced by the fluid for the assumed simulation input parameters. As the simulation progresses, the system stabilizes and the number of particles reaches a plateau. The unipolarly charged (agglomerated) particles are distributed in such a way that a stable equilibrium is achieved. As a result, there are no further collisions, which means that particle size and charge distribution also remain constant. Transferring the findings to the filter testing with the experimental setup introduced in 2.2.1, this

means that the agglomeration phenomenon is already completed before the particles reach the first, upstream sample collection point. Thus, no direct influence of the electrostatic agglomeration on experimentally determined filtration performances is expected. However, the exact knowledge about the resulting particle size and charge distribution forms the basis for further simulations. They constitute the input parameters for simulation studies of the particle behavior in filter media. Thus, they have a substantial impact on the simulated collection efficiency.

Evolution of Particle Charge and Size Distribution. Figure 5.10 demonstrates the change in particle charge distribution due to the strong electrostatic particle-particle interactions. The evolving output distribution after $t = 10\,\mu s$ is directly contrasted to the predetermined input distribution. In order to analyze the behavior of all simulated particles at the same time, the charged particles from all nine simulation runs are summed up in this plot.

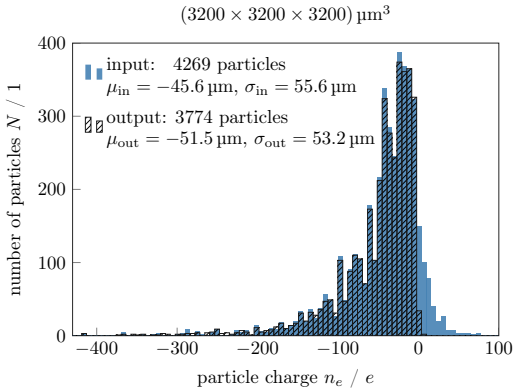

Figure 5.10: Change of particle charge distribution averaged over all nine simulation runs with the domain size $(3200 \times 3200 \times 3200)\,\mu m^3$, the mean charge prefactor $a = 40$ and 10 % positively charged particles. The input distribution corresponds to the average of the plots presented in Fig. 5.7. The mean particle charge of both distributions is given by μ and σ denotes the standard deviation. Input and output distribution differ at this point because the total number of particles changes. The plot is adapted from Schober et al. [90].

The calculation of the electrostatic charge of an agglomerate is carried out by summing up the individual charges of all associated particles. The diagram confirms the previous statement that all positively charged particles in the system adhere to negative ones. Nonetheless, some very weakly charged positive particles remain in the system. They are the result of an agglomeration of a highly positively charged particle with a negatively charged particle of lower intensity such that $\sum n_e > 0$. The resulting agglomerate is charged (positively) so weakly that the interaction with other particles is very low. For longer simulation times, a further collision with other particles is possible. The number of negatively charged particles in the system remains virtually unchanged by the accumulation of positively charged particles. As can be seen from the values given in the legend, though, the overall mean charge drops slightly from $\mu_{\text{in}} = -45.6\,e$ to $\mu_{\text{out}} = -51.5\,e$. This is due to the fact, that the sum of all charges is divided by a different number of particles for the input and output distribution. The slightly reduced standard deviation (from $\sigma_{\text{in}} = 55.6\,e$ to $\sigma_{\text{out}} = 53.2\,e$) reflects the narrowed width of the charge distribution.

In addition to charge distribution, agglomeration due to electrostatic particle-particle interactions alters the particle size distribution in the system. The particle sizes are of particular interest as they are decisive for the degree of the respective mechanical collection mechanisms in subsequent filtration processes. This way, agglomeration can promote inertial particle separation. Since agglomerated particles do not form spherical clusters, mass-equivalent diameters are assumed in the following evaluation for particles sticking together in an agglomerate. Analogous to Fig. 5.10, the predetermined input and emerging output size distributions are provided in Fig. 5.11. Again, the number of the respective particle classes is summed up from all nine simulation runs. On the left-hand side of Fig. 5.11, the particle distributions are plotted over size classes. This allows focusing on the frequently occurring small particles ($d_{\text{P}} < 2\,\mu\text{m}$). It is obvious that the number of particles in this size range clearly decreases during the agglomeration process. In exchange, new (agglomerated) particles are formed especially in the medium size range $d_{\text{P}} = 1.8\,\mu\text{m}$ to $3\,\mu\text{m}$. However, note that very small (lightweight) particles adhering to large particles do not change the larger particles' mass noticeably. The respective mass for a given particle size class instead of number distributions are

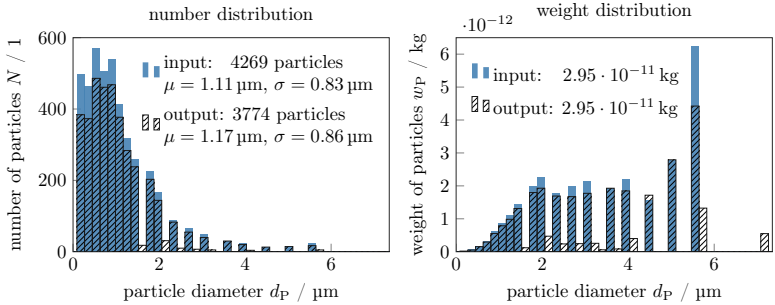

Figure 5.11: Change of discrete particle distribution averaged over all nine simulation runs using the domain size $(3200 \times 3200 \times 3200)\,\mu m^3$. The number distribution (left) as well as the mass distributions (right) of the emerging (agglomerated) particles are compared to the predetermined simulation input parameters. For both plots, the complete output particle spectrum is divided into bars of equal width. In these bars, particles from both, input and output, distributions are classified. The plots are adapted from Schober et al. [90].

plotted on the right-hand side of Fig. 5.11 to point out the impact of agglomeration on the larger particles in the system.

This shift towards larger and heavier particles already indicates a non-negligible influence on the subsequent filtration process. The contribution of the 'artificial filtration' efficiency by the agglomeration phenomenon to the overall filtration efficiency is analyzed below. In addition to the particle size distribution, the fact that only one charge polarity remains in the system is also essential. For instance, a uniformly oppositely charged fiber as evaluated in Sec. 4.2 would thus attract all particles.

'Artificial Filtration' Efficiencies. The agglomeration of particles can be interpreted as an 'artificial filtration' process, where small particles are 'filtered' by means of attaching to larger particles. Analogous to the known calculation of usual filtration efficiencies from the ratio of the number of collected particles $(N_{inlet}(d_P) - N_{outlet}(d_P))$ to the number of particles at the inlet $(N_{inlet}(d_P))$ according to Eq. (2.3), the 'artificial filtration' efficiency η_a is quantified. In this specific case,

$N_{\text{inlet}}(d_{\text{P}})$ and $N_{\text{outlet}}(d_{\text{P}})$ correspond to the number of particles of the size class d_{P} before and after the agglomeration process.

The 'artificial filtration' efficiencies resulting from the simulation studies presented so far are plotted in Fig. 5.12. Again, the mean value and the standard deviation are plotted for each of the three particle size distributions shown in Fig. 5.6.

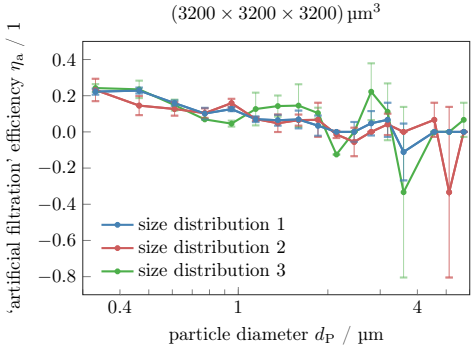

Figure 5.12: 'Artificial filtration' efficiency η_{a} for the three randomly drawn particle size distributions presented in Fig. 5.6. The error bars are derived from the three charge distributions (see Fig. 5.7) associated to each particle size distribution.

As already apparent from the change in the distribution of particles over size classes (see Fig. 5.11), especially small/lightweight particles are strongly attracted by others and, thus, adhere to them. Hence, very high 'artificial filtration' efficiencies up to $\eta_{\text{a}} = 25\,\%$ are obtained for the smallest particle size class with the specified simulation input parameters. For larger particles, the 'artificial filtration' efficiency decreases, but the scattering increases at the same time. Since the number of large particles is limited, changing the size of a few particles by attaching oppositely charged particles already has a major impact. Occasionally, the agglomeration process even yields strongly negative 'artificial filtration' efficiencies ($\eta_{\text{a}} = -33\,\%$) for particles with $d_{\text{P}} > 2\,\mu\text{m}$. In the corresponding particle size classes, more particles are present after the agglomeration process than before. This is due to new particles generated by the agglomeration of smaller ones. The

high scattering would diminish by a high quantity of repetitions of the simulation experiment with further input parameter sets.

As mentioned in Sec. 5.1.1.1, Dirichlet boundary conditions at the inlet and outlet of the simulation domain are analyzed in addition to the force-driven flow field. In contrast to the previously applied flow field initiated by forces, which only alters due to particle movements, the Dirichlet boundaries conditions are effective over the entire simulation time. Hence, the fluid flow in vertical direction is maintained. The resulting permanently acting drag forces on the particles are expected to reduce the degree of particle agglomeration. Furthermore, particles crossing the periodic MD boundaries are accelerated or decelerated by the Dirichlet boundary conditions. Figure 5.13 compares the 'artificial filtration' efficiencies on the basis of the two different fluid flow conditions. For this purpose, the 'artificial filtration' efficiency η_a is averaged over all nine simulation runs.

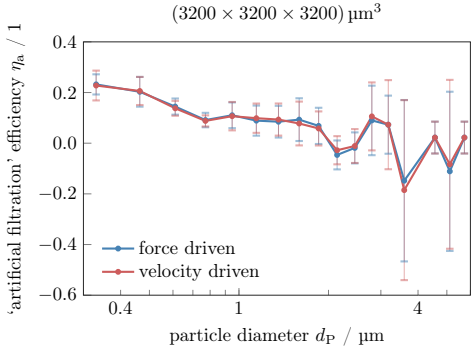

Figure 5.13: Simulated 'artificial filtration' efficiencies based on a force-driven and a velocity-driven flow field. All nine simulation runs for $(3200 \times 3200 \times 3200)\,\mu m^3$ are averaged for each curve. The error bars indicate the resulting standard deviations.

The simulated 'artificial filtration' efficiencies and the particle dynamics due to electrostatic interactions do not differ at all. This observation intensifies the assertion of strong dominance of electrostatic forces between charged particles over drag forces. All following simulations are based on the force-driven flow field.

In the next step, the influence of the applied domain size and the associated initial number of particles on the degree of agglomeration is investigated. Besides the already presented results for a domain size of $(3200 \times 3200 \times 3200)\,\mu m^3$, the dimensions $(1280 \times 1280 \times 1280)\,\mu m^3$ and $(6400 \times 6400 \times 6400)\,\mu m^3$ are considered for the cubic simulation domain. Another particle sampling results in an average (over three randomly drawn size distributions in each case) of 48, 474 and 3171 particles for the respective domain sizes. For the largest domain size, the basic particle size distribution plotted in Fig. 5.2 is extended to larger particles up to $d_P = 10\,\mu m$. As above, the resulting 'artificial filtration' efficiencies of interest are compared with each other. In Fig. 5.14, each curve is again based on nine simulation runs, with three particle size distributions and three charge distributions for each of them.

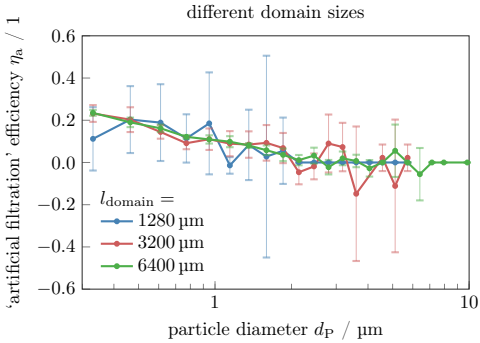

Figure 5.14: Simulated 'artificial filtration' efficiencies using different domain sizes and consequently (at constant particle concentration) different numbers of particles. In each case, the mean values from nine simulation runs with various randomly drawn particle size and charge parameters are shown. The error bars display the associated standard deviations.

All curves mainly show the same, already stated characteristics, i.e., high efficiencies for small particles decreasing with increasing particle diameters. They only differ in their smoothness and their extent of scattering. The fewer particles exist in the system, the higher the scattering due to statistical effects as, e.g., the formation of individual agglomerates has a greater impact. For the smallest domain size with

$l_{\mathrm{domain}} = 1280\,\mu\mathrm{m}$, therefore, the largest oscillations and standard deviations are observed. Particles in the size classes larger than $d_{\mathrm{P}} = 2\,\mu\mathrm{m}$ are drawn only once or not at all and, hence, yield an efficiency of $\eta_{\mathrm{a}} = 0$ without any scattering. The medium domain size with $l_{\mathrm{domain}} = 3200\,\mu\mathrm{m}$ in contrast, reveals very large standard deviations in this particle size range. With more than 3000 particles in the largest domain, the scattering is drastically reduced and the curve of the 'artificial filtration' efficiency becomes very smooth. However, the simulation runtime significantly increases with increasing number of Lattice-Boltzmann cells. Each simulation for the largest domain with $(6400 \times 6400 \times 6400)\,\mu\mathrm{m}^3$ takes about eight days on Intel Xeon Gold 6148 processors using 32 CPU cores. Nevertheless, the following simulation studies concerning different particle charge conditions, which are of particular interest in this work, are performed using the largest simulation domain.

As mentioned in the introduction of simulation input parameters (see Sec. 5.1.1.3), the analysis of different particle charge conditions focuses on the selected gradient a to generate the mean charge distribution as well as the percentage of positively charged particles in the system. The latter defines the standard deviation for the Gaussian distribution within each particle size class. To begin with, the left-hand side of Fig. 5.15 shows the effect of different gradients a on the 'artificial filtration' efficiency, i.e., the degree of agglomeration. As in the previous plots, the mean value and standard deviation from nine simulation runs are presented in each case.

Independently of the particle mean charge gradient a (in the examined range), the 'artificial filtration' efficiencies show the same characteristics as in the previous plots. Thus, the resulting degree of agglomeration is independent of the particle charge intensity for the investigated parameter range.

In contrast to charge intensity, the percentage of positively charged particles in the simulation system significantly changes the 'artificial filtration' efficiency. The associated simulation results are presented on the right-hand side of Fig. 5.15 for 5 %, 10 % and 20 % positively charged particles. If there is a strong imbalance of charge polarities at the beginning, e.g., 5 % positively charged and 95 % negatively charged, the degree of 'artificial filtration' efficiency is very low. The strong electrostatic particle-particle interactions only occur until all particles of less

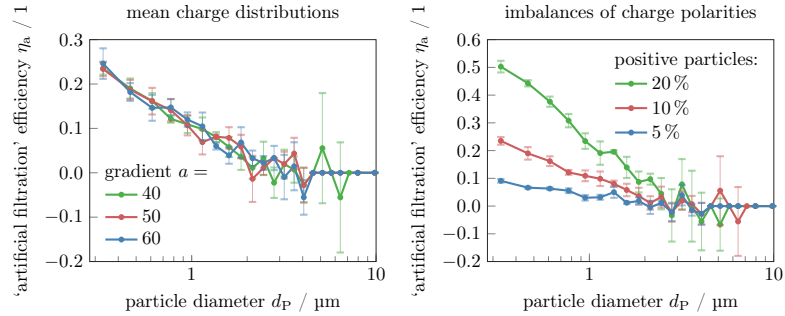

Figure 5.15: Simulated 'artificial filtration' efficiencies for the different values of a in the mean charge distribution plotted in Fig. 5.4 (left) and different percentages of positively charged particles in the simulation system (right). In each case, the mean values from nine simulation runs with various randomly drawn particle size and charge parameters are shown. The error bars display the associated standard deviations. The results have already been published prior to this thesis [90].

frequently occurring polarity are bounded. As already concluded from Fig. 5.9, an equilibrium of unipolarly charged (agglomerated) particles emerges afterwards. With an increase in the number of positively charged particles in the system (lower imbalance), the degree of electrostatic agglomeration increases. When looking at the smallest particles, the 'artificial filtration' efficiency rises from just under $\eta_a = 10\,\%$ (blue) to $\eta_a = 25\,\%$ (red) by doubling the number of positively charged particles. If 20 % (green) of all particles are positively charged, approximately half of all particles with $d_P = 0.3\,\mu m$ adhere to larger ones and are, thus, considered 'filtered'. Furthermore, it is noticeable that oscillations and standard deviations also increase significantly when more particle-particle interactions occur. Due to the strongly pronounced effect of the particle charge composition, the consideration of electrostatic agglomeration is of major importance in simulation studies.

5.2 Uni-Directional Simulation of Particle Dynamics in the Test Facility

In this section, particle dynamics in the entire test channel is analyzed. The focus is on complex flow patterns induced by the test channel geometry and their impact on particle distributions at the measurement locations. Due to the observations above, in particular the very fast particle-particle agglomeration, a uni-directional flow-particle coupling is sufficient here. The commercial simulation tool ANSYS Fluent allows simulating the particulate flow through the complex test channel geometry with feasible computational effort. The focus of the investigations in this section is the influence of the fluid flow on the trajectories of different particle sizes. The simulations serve to provide insights into the processes in the (non-visible) interior of the test rig. The employed simulation experiment setup and the obtained results are presented in detail below.

5.2.1 Simulation Experiment Setup

The simulation experiment setup directly arises from the modular filter media test rig (MFP 3000, see Sec. 2.2.1) used for the experimental measurements in this work. All dimensions of the test channel are determined manually and are directly used as reference points for the CAD model. The resulting geometry of the channel walls is shown on the left-hand side of Fig. 5.16. Even though no filter media are considered in this chapter, their virtual position in the model is marked for reference. Furthermore, the critical points concerning the simulation boundary conditions are zoomed in and a schematic representation is provided in each case. The simulation parameters introduced below (and in Fig. 5.16) correspond to the values of the experimental analysis in the following section.

Dust particles are blown off the rotating brush (RBG 1000) with a predefined dispersion volume flow rate of $\dot{V}_{\text{main}} = 28\,\text{l/min}$ and are subsequently injected to the test channel via a connecting tube (indicated in red). The applied particle concentration $c_{\text{P}} = 75\,\mu\text{g/m}^3$ is prescribed by laboratory experiments. Further volume flow rates given in Fig. 5.16 are controlled by a suction flow at the lower end of the test channel. The volume flow rate $\dot{V}_{\text{outlet}} = 70\,\text{l/min}$ at the outlet is adjusted such that a specified flow velocity ($v = 11.1\,\text{cm/s}$) is achieved at the height

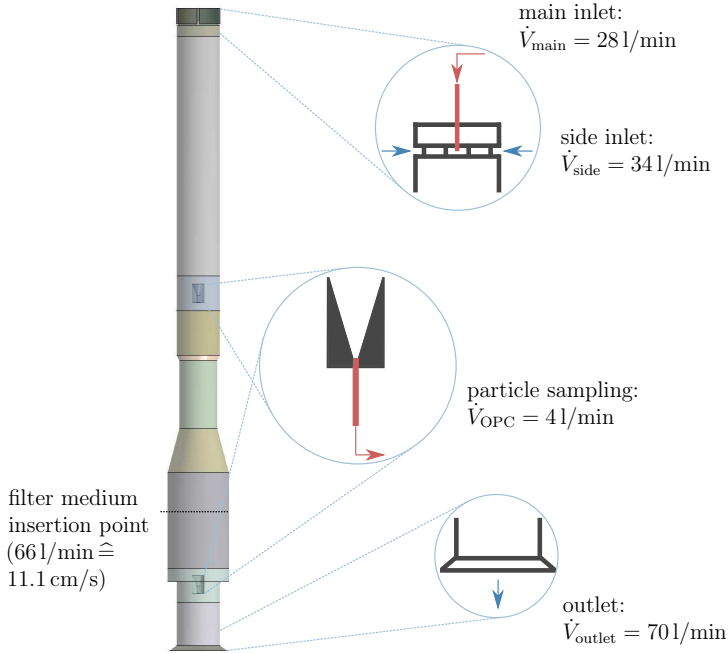

Figure 5.16: CAD model of the MFP test channel schematically sketched in Fig. 2.6 (left). The most important details in relation to the simulation boundary conditions are additionally outlined in cross section (right): inlet, particle sampling and outlet.

of the hypothetical filter medium. Since the downstream sample collection point (to measure the particle size distribution with an OPC) is located between the filter medium insertion point and the channel outlet, the two volume flows differ by $\dot{V}_{\text{OPC}} = 4\,\text{l/min}$. Particle sampling also takes place upstream the (virtual) filter medium via the same conical geometry, which likewise requires a volume flow rate of $\dot{V}_{\text{OPC}} = 4\,\text{l/min}$. Since higher volume flows are needed for the measurements than the provided dispersion volume flow, the main inlet is supplemented by a side inlet ($\dot{V}_{\text{side}} = 34\,\text{l/min}$). This volume flow is not specified in the simulation experiment, but is achieved by Neumann boundary conditions with the ambient air pressure

Parameter		Value
Main inlet flow rate	$\dot{V}_{\text{main}}$	28 l/min
Side inlet flow rate	$\dot{V}_{\text{side}}$	34 l/min
Volume flow for OPC	$\dot{V}_{\text{OPC}}$	4 l/min
Suction flow rate	$\dot{V}_{\text{outlet}}$	70 l/min
Media velocity	v	11.1 cm/s
Dynamic viscosity (air)	η_{air}	$1.79 \cdot 10^{-5}$ kg/(m s)
Density (air)	ρ_{air}	1.225 kg/m^3

Table 5.1: Overview of the parameters used for the uni-directionally coupled simulation of particle dynamics in the test facility with ANSYS Fluent.

$p_\infty = 1013$ mbar. Air is supplied to the test channel through a narrow gap, which is supported by four struts. All simulation parameters used for the uni-directionally coupled simulation of particle dynamics are summarized in Tab. 5.1.

The following numerical results of the uni-directionally coupled simulation consist of two parts. In the first part, the air flow field through the test channel geometry is calculated based on the presented boundary conditions. In the second part, particle parcels (groups of particles with the same diameter) are added over the entire cross section of the main inlet and their trajectories are finally simulated.

5.2.2 Numerical Results

Firstly, the simulated flow profile in the test channel is analyzed. The left-hand side of Fig. 5.17 shows a 2D plot of the absolute flow velocity in the test channel under the specified boundary conditions. The narrow cross section of the main inlet causes an air jet flow in this area. The high fluid velocities spread conically across the domain width, but decrease in flow direction. In the area upstream the first sample collection point, a homogeneous flow field over the complete channel diameter is formed. Additionally, the air velocity is constant over the remaining test channel (virtual filter media insertion point, second sample collection point).

Beside the inlet flow, the fluid properties before the two measuring points are of particular interest. The flow field can influence the particle distribution at the sample collection points due to Brownian motion and inertia effects. In order to examine the flow pattern upstream both measuring points more closely, the same

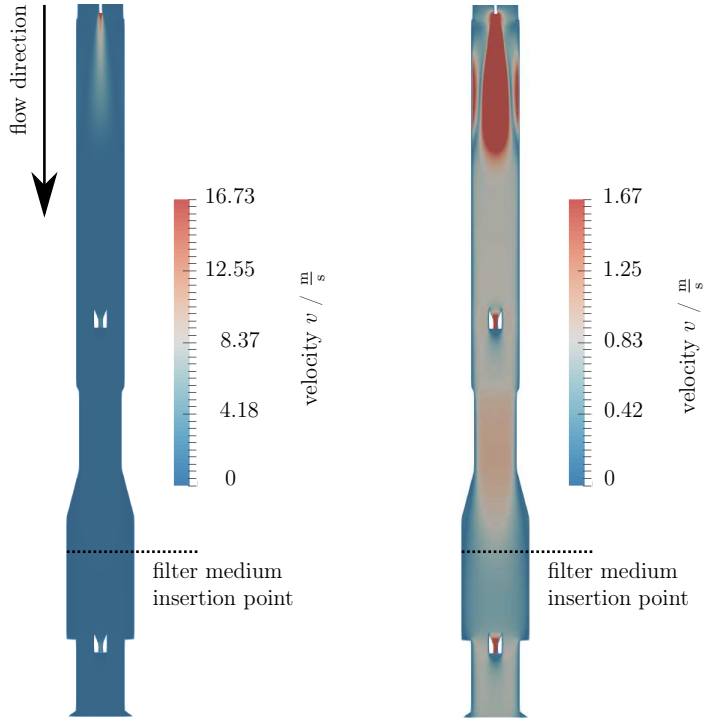

Figure 5.17: Air flow field in the test channel simulated with ANSYS Fluent applying the boundary conditions introduced in Fig. 5.16.

plot is shown using a different color scaling for a smaller velocity range on the right-hand side of Fig. 5.16. To begin with, the defined target velocity $v = 1.11\,\mathrm{m/s}$ can be seen at the height of the filter medium insertion point. However, there is a clear difference between the magnitude velocity upstream the first and second sample collection point. The air velocity is higher at the upper sample collection point due to the smaller channel cross section in this area. In both cases, there is a homogeneous flow distribution over the channel width (apart from the channel walls with $v = 0\,\mathrm{m/s}$).

Secondly, particle trajectories are simulated based on the presented fluid flow field. The results for different particle sizes are shown in Fig. 5.18. For better visibility, only a small portion of the simulated parcels is plotted. Due to the nature of the flow (multiple inlets), particles tend to recirculate at the top end of the test channel. On the one hand, this leads to a proper mixing of the dispersed particles such that a homogeneous distribution is ensured. On the other hand, recirculation substantially increases the residence time of dust particles in this area of the test channel. Transferring the findings about the strong electrostatic particle-particle interactions from Sec. 5.1.2, agglomeration should be completed after this recirculation section of the test channel. Thus, the agglomerates are formed well before the first sample collection point. Besides plotting the trajectories in the complete test channel, the most interesting parts are enlarged. The inlet area shows that all analyzed particle sizes (differently colored) are involved in the recirculation. There is no noticeable difference between the trajectories of individual particle diameters. Trajectories at the height of the two sample collection points also do not allow any statement about significantly different particle dynamics depending on the particle diameters. Most parcels follow the air flow towards the channel outlet. Individual bends in the particle trajectories can not be clearly assigned to specifically small or large particles.

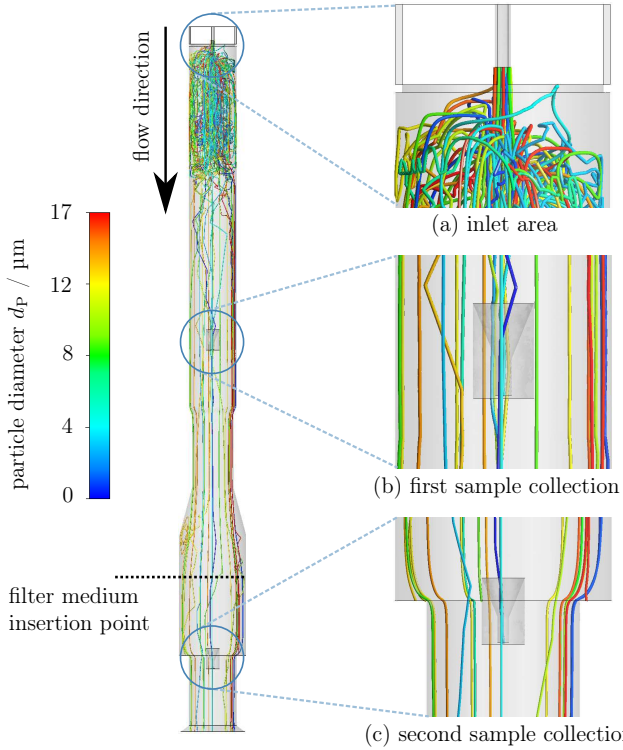

Figure 5.18: Trajectories of particle parcels simulated with the uni-directionally coupled approach implemented in ANSYS Fluent. The colors of the trajectories indicate the particle diameters. In addition to the complete test channel, enlargements of the most critical areas are plotted: (a) inlet area, (b) first sample collection point and (c) second sample collection point.

Based on the ratio of particles at the first and second sample collection point, an 'artificial filtration' efficiency can be calculated for the empty test channel. In this case, $N_{\mathrm{inlet}}(d_{\mathrm{P}})$ and $N_{\mathrm{outlet}}(d_{\mathrm{P}})$ from Eq. (2.3) corresponds to the number of particles at the first and second sample collection point. Due to their movements based in the underlying flow field, different particle distributions at both measuring points are possible. The resulting 'artificial filtration' efficiency from the particle trajectories from Fig. 5.18 is plotted in Fig. 5.19. The scattering is very high due to the small number of particles (maximum 180 particles per size class) that are detected in the area of the conical particle removal points. Nevertheless, a clearly negative 'artificial filtration' efficiency for most investigated particle diameters is visible, i.e., more particles of a specific size class are determined at the second sample collection point than at the first. The influence of the test channel geometry and the resulting fluid flow field on particle dynamics and, thus, on the separation behavior is not negligible.

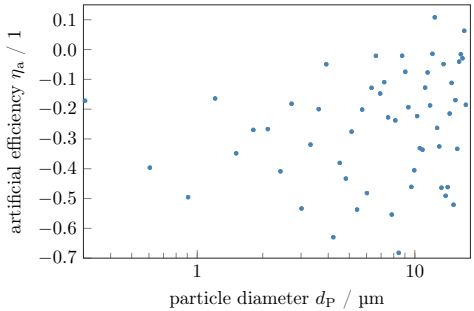

Figure 5.19: 'Artificial filtration' efficiency calculated from the number of particles at the first and second sample collection point of the test channel. The results are based on the uni-directional coupled simulation approach implemented in the software ANSYS Fluent.

5.3 Experimental Analysis

In this section, simulation studies on the particulate flow through an empty test channel are supplemented by experimental measurements. In contrast to simulation, however, individual effects such as fluid flow effects or electrostatic agglomeration, can not be analyzed completely independently of each other. By appropriate choice of the experimental testing setup, the focus can still be placed on different possible influencing factors. Various applied setups are introduced below. The investigation of the influence of dust particle charges is of particular interest in this thesis. As in the simulation studies in Sec. 5.1 and Sec. 5.2, the 'artificial filtration' efficiency is the basis for the subsequent evaluation.

5.3.1 Experimental Testing Setup

All experimental measurements in this chapter are performed using the modular filter media test rig (MFP 3000) introduced in Sec. 2.2.1. The configurations presented below fully exploit the potential of this modularity. In all cases, the fractional 'artificial filtration' efficiency η_a is calculated according to Eq. (2.3). By contrast, flow and measuring influences are evaluated instead of electrostatic agglomeration processes at this point. As for the simulation of the test channel, $N_\mathrm{inlet}(d_\mathrm{P})$ and $N_\mathrm{outlet}(d_\mathrm{P})$ correspond to the number of particles in a specific size class at the upstream and downstream sample collection point. For filter tests, the terms 'raw' and 'clean' gas are established. Although no filter medium is inserted in this chapter, the terms are used synonymously for the gas distributions at the upstream and downstream measurement points. The objective of the measurements is to find out whether the background air flow field also leads to an 'artificial filtration' efficiency in reality. In addition, the experimental analysis aims at showing whether further effects occur, which have not yet been taken into account in the simulation. The test conditions for the particulate flow through the empty test channel used in all measurements of this section are summarized in Tab. 5.2.

Parameter		Value
Test dust		ISO fine dust
Dust concentration	c	$75\,\mathrm{mg/m^3}$
Dispersion volume flow rate	$\dot{V}_{\mathrm{disperse}}$	$28\,\mathrm{l/min}$
Channel volume flow rate	$\dot{V}_{\mathrm{channel}}$	$66.6\,\mathrm{l/min}$
Volume flow for OPC	$\dot{V}_{\mathrm{OPC}}$	$4\,\mathrm{l/min}$
Media velocity	v	$11.1\,\mathrm{cm/s}$

Table 5.2: Constant test conditions used for measuring the 'artificial filtration' efficiencies in the empty test channel. The channel volume flow rate and media velocity correspond to the flow conditions between the two measuring positions, i.e., at the height of the hypothetical filter medium insertion point. Due to the continuous particle removal at both measuring points, the flow conditions upstream the first and downstream the second sampling point deviate from that.

The following setups are used to determine the influence of the sensor position and the electrostatic particle charge. In order to determine the influence of each parameter, only one component is varied at a time.

Sensor Positions. The first experiments focus on the arrangement of the aerosol sensors equipped with a light-scattering spectrometer in the test facility. Two positions along the test channel are intended for particle sampling, i.e., one upstream and one downstream of the virtual filter medium insertion point (see Fig. 2.6). Based on these restrictions, the following two approaches are used to measure the particle size distribution in the raw and the clean gas:

The **upstream & downstream setup** represents the design exactly as depicted on the left-hand side of Fig. 2.6. Raw and clean gas size distributions are measured quasi-simultaneously upstream and downstream the virtual filter medium. The method thus enables a direct determination of the fractional 'artificial filtration' efficiency during the measurement. Alternating measurements of the raw and clean gas distribution are carried out for 50 s each. A total of four measurements, which are averaged afterwards, are carried out in each case. Between each measurement is a 10 s break in order to avoid errors due to the sensor switching at the optical particle counter.

The **exchanged sensors setup** involves a modification of the test facility between raw and clean gas measurement. In a first step, the above introduced upstream & downstream setup is used to determine the raw gas distribution. The associated clean gas distribution, however, is disregarded and redetermined in a subsequent step in which the two sensors are swapped. Thus, the clean gas distribution is determined downstream the filter medium using the actual raw gas sensor. In this second step, the raw gas distribution in turn is omitted. To calculate the fractional collection efficiency, the clean gas distribution from the second measurement is related to the raw gas distribution from the first step.

The aim of the upstream & downstream setup is to find out whether the particle distribution is constant along the test channel. A fluctuation over the height of the test rig would have a direct effect on the measured 'artificial filtration' efficiency. Furthermore, the measurements are intended to ensure that the different volume flow rates at the two measuring points do not affect the measured 'artificial filtration' efficiency. Usually, measured collection efficiencies would, therefore, not only reflect the actual particle deposition on the filter medium. The second setup with exchanged sensors is used to exclude an influence of the two (ideally identical) sensors.

Particle Charging States. Finally, the impact of discharging particles on the filtration behavior is investigated. The position of the corona-discharge module, which can be connected to the test rig on demand, is also illustrated in Fig. 2.6. Two distinct cases are investigated experimentally:

Untreated (charged) particles are commonly used to determine air filter performances. The particles are usually triboelectrically charged during dispersion and their further way towards the filter medium. These sometimes very strongly charged particles are already used in the previous scenarios (for sensor positions) presented so far. The measurements of the upstream & downstream setup are thus used again for the comparison with discharged particles.

Discharged particles refer to particles after treatment by the corona-discharge unit, which is described in detail in Sec. 2.2.3. The method does

not ensure the complete neutralization of the dust particles, but leads to a substantial charge reduction.

The measurements with different charging states for the particles are intended to reveal different particle dynamics in the test channel. According to the fully-coupled simulation studies in Sec. 5.1, electrostatic agglomeration is completed before the first sample collection point and should therefore not affect the measurement results. However, the electrostatic charge of dust particles could also lead to increased attachment on the channel walls. A detailed evaluation of all experimental results follows.

5.3.2 Experimental Testing Results

Based on the testing setups introduced above, particle dynamics in the empty (without filter medium) test channel are discussed in this section. The experimental testing results consist of two parts: Firstly, the impact of two particle sensors on the 'artificial filtration' efficiency is analyzed, and secondly, the influence of discharging particles at the test channel inlet is presented. All following experimental testing results show uncorrected collection efficiencies in the empty test channel. In actual filtration measurements, the collection efficiencies are corrected with factors determined daily in a preceding calibration measurement step.

Influence of the Sensor Positions. The measurement results obtained with the upstream & downstream arrangement of raw and clean gas sensors are contrasted to the exchanged sensor setup in Fig. 5.20. In the latter case, only the measurements from the clean gas sensor (connected downstream first, upstream second) are used for evaluation. This way, the influence of the two different sensors used in the upstream & downstream setup can be eliminated. The mean value of four measurement series and the associated standard deviation are plotted in each case.

When analyzing the results obtained by using the upstream & downstream setup, substantial differences of the 'artificial filtration' efficiency over the particle diameter are observable. The number of particles smaller than $d_\mathrm{P} = 4\,\mu\mathrm{m}$ remains almost constant between the two measuring points resulting in a maximal 'artificial filtration' efficiency of $\eta_\mathrm{a} = 6.7\,\%$. Compared to common collection efficiencies for cabin air filter media of well above $\eta_\mathrm{CAF} = 90\,\%$, this 'artificial filtration' efficiency

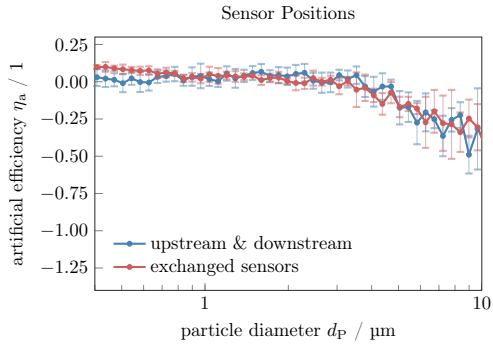

Figure 5.20: Experimentally determined fractional 'artificial filtration' efficiencies η_a in the empty test channel. The particle size distributions in raw and clean gas required for calculating the efficiency are determined with the upstream & downstream setup and the exchanged sensor setups. In both measurements (consisting of four individual measurement series), an optical particle counter is applied.

is negligible. Thus, two different conceivable influences in the test channel can be excluded: Firstly, dust particles do not attach or detach to the inner walls of the test channel at a substantial rate (compared to the actual filter efficiency). A thorough cleaning of the test channel after each measurement also contributes to keeping the wall influences to a minimum. Secondly, the different volume flow rates at the upstream and downstream measuring points have no influence on the measured particle distribution. Considering the complexity of the testing procedure with the continuous particle dispersion, the scattering in this particle range is reasonable. Larger particles, however, yield clearly negative 'artificial filtration' efficiencies up to $\eta_a = -49\,\%$. In other words, negative filtration efficiencies mean that more particles are measured downstream than upstream the virtual filter medium insertion point. The highly negative efficiencies can be explained by the small number of present particles in the respective size classes. Since large particles do not occur very frequently, the scattering in this area is also very high. Doing a much larger number of experiments in order to also get representative statistics for the rare larger particles might eliminate the negative efficiencies but would induce very high cost.

The comparison with the results obtained by the exchanged sensors setup leads to a very good agreement, although the test procedure is very sensitive and an intervention in the test facility is usually critical. Both, the mean values and the intensities of the scattering are very similar. With this result, it can be excluded that the measured 'artificial filtration' efficiencies from the upstream & downstream setup are caused by using two 'different' sensors.

Influence of Particle Discharging. Using the upstream & downstream arrangement of particle sensors on the filter test rig, the influence of corona-discharged particles on the 'artificial filtration' efficiency is analyzed. For this purpose, Fig. 5.21 compares the measurement results using untreated (charged) and discharged dust particles.

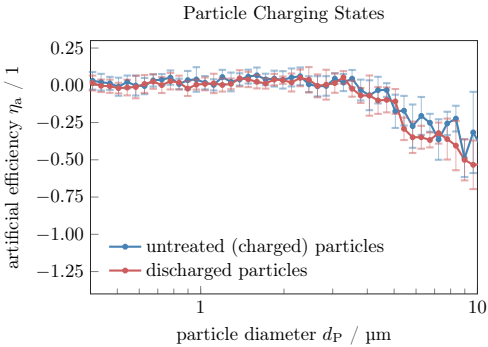

Figure 5.21: Experimentally determined fractional 'artificial filtration' efficiencies η_a in the empty test channel with untreated (charged) particles and corona-discharged particles. The particle size distributions in raw and clean gas required for calculating the efficiency are determined using the upstream & downstream setup with an optical particle counter. Both measurements consist of four individual measurement series.

The two particle charging states show exactly the same efficiency behavior. As above, the amount of small particles with $d_P < 4\,\mu m$ remains constant over the length of the test channel, whereas larger particles yield negative 'artificial filtration' efficiencies. As already seen in the fully-coupled simulation studies, electrostatic

agglomeration does not occur between the two sample collection points of the test channel, but is completed well before. Thus, the 'artificial filtration' efficiency resulting from particle-particle interactions does not influence in the measurement results.

5.4 Summary

The high potential of the fundamentally new fully-coupled simulation approach was exploited for the first time with regard to filtration processes. The focus was on the complex particle-particle interactions in the inflow area of cabin air filter media which have been neglected so far. Due to the highly bipolar charge distribution, dust particles strongly attract each other electrostatically and form agglomerates. Thereby, the degree of electrostatic agglomeration does not depend on the particle charge intensities, but to a large extent on the imbalance between the two charge polarities. For small particle sizes, 'artificial filtration' efficiencies up to $\eta_a = 50\,\%$ were calculated for an initial system of 80 % negatively and 20 % positively charged particles. As a result, the dust particles are only negatively charged when reaching the height of the filter medium. If the filter fibers also carry an electrostatic charge, the unipolar particle charge distribution affects the resulting overall filtration efficiency as seen in Chapter 4.

The second simulation study of this chapter provided valuable insights into the particle behavior in the empty channel of the applied filter test facility in this work. Simulations with a uni-directionally coupled approach revealed a variation of the particle distribution between both sample collection points, which are arranged upstream and downstream the virtual filter medium. Due to the nature of flow, more particles of specific size classes emerged at the downstream than at the upstream measuring point resulting in negative 'artificial filtration' efficiencies. Furthermore, the simulation of parcel trajectories revealed a strong recirculation of particles in the upper area of the test channel induced by the flow conditions. The recirculation results in a good mixing of the particles at the channel inlet. The influence of the resulting particle distribution on measurement results of filter media needs to be clarified in future research studies.

Experimental analyses of the particle behavior in the empty test channel completed this chapter. Several similarities to the simulation results are found. First of all, negative 'artificial filtration' efficiencies also occurred in the experimental testings for large particle classes. As shown by the results of the four-way coupled simulations, electrostatic agglomeration is already completed within a few microseconds. Therefore, these strong interactions occur upstream the first sample collection point and, thus, do not affect the measured filtration efficiency. However, the resulting particle size and charge distributions are of particular interest as they are the key for the simulation of further filtration mechanisms such as mirror charge effects.

Both analysis methods used in this chapter demonstrated the complexity of particle dynamics in the test facility. Electrostatics, hydrodynamics and the sensitive testing procedure are the main responsible factors. The findings of this chapter contributed to a better understanding of the underlying physical processes and enable further simulations of the particulate flow through cabin air filter media.

Chapter 6

Numerical & Experimental Analysis of Wired Weaves

As discussed in Chapter 4, the fully-coupled modeling approach is well-suited for the simulation of particle deposition on single fibers. Since a wired weave forms a network of individual fibers braided together, it is excellently suited for studying further filtration effects. Compared to the theoretical model of fiber arrays analyzed in Sec. 4.3, wired weaves distinguish themselves by being machine-producible. Moreover, they can be purchased ready for use from manufacturers such as Spörl KG [93]. The physical samples allow supplementing the simulation studies with experimental investigations and, thus, provide an additional perspective on relevant filtration effects. Furthermore, the structure of wired weaves is more uniformly reproducible compared to commonly applied filter media. Hence, they represent an intermediate stage between individual fibers and real filter media in terms of complexity.

The metallic filter media are characterized by their stability and resistance against physical influences. Therefore, they are primarily applied in the fields of high-temperature filtration, high-viscosity filtration or particle filtration of chemically aggressive liquids [37]. In this work, however, they are used to gain new insights into the deposition behavior of airborne particles. Compared to common complex filter media made of cellulose or synthetics, wired weaves offer a decisive advantage: Their conductive material allows the filter substitute to be easily discharged in the test facility by grounding. For the digital reproduction of the experiments, this means that a lot of unknown parameters causing difficulties in real filters

become irrelevant. For instance, the charge intensity and distribution in the filter medium, which are difficult to access experimentally, can simply be neglected for grounded wired weaves. The fiber-particle interactions by Coulomb forces and induced dipole effects are thus omitted. This way, wired weaves offer the exclusive possibility to focus on the influence of dust particle charges on the filtration behavior – in addition to the permanently acting mechanical collection mechanisms.

The objective of this chapter is to quantify the influence of particle charges on the fractional collection efficiencies of wired weaves. Section 6.2 presents the experimental testing setups used for this purpose, followed by the respective measurement results. Various experiments serve to make a contribution to a better understanding of the underlying physical processes. The aim is to show which additional effects occur in the test facility and which role these effects play with regard to separation efficiencies.

To study the details of the dust particle behavior, simulations are necessary. At this point, in Sec. 6.3, the difference between the uni-directional coupling and the novel fully-coupled system is of particular interest. The trajectories are investigated for neutral particles as well as electrostatically bipolarly charged particles, where a strong interaction is expected. Finally, experimental and simulation results are contrasted in Sec. 6.4. The aim of this comparison is to verify the comparability of simulations using spherically modeled particles with experimental measurements of optical or aerodynamic particle diameters. First of all, however, an overview of the wired weaves used in this work for both, simulations and experimental analysis, is outlined in Sec. 6.1 including a detailed description of their characteristic properties.

6.1 Specification of Wired Weaves

All experiments in this chapter are carried out with the three different weave geometries illustrated in Fig. 6.1. The wires consist of stainless steel according to DIN 1.4401/1.4404 and DIN 1.4301/1.4306 and are produced by Spörl KG [93]. All of them represent very dense weaves with square meshes, but differ in their characteristic sizes, i.e., mesh width w and wire diameter d. The finest weave (a) available from Spörl KG has a mesh width and a wire diameter of $w = d = 20\,\mu\text{m}$.

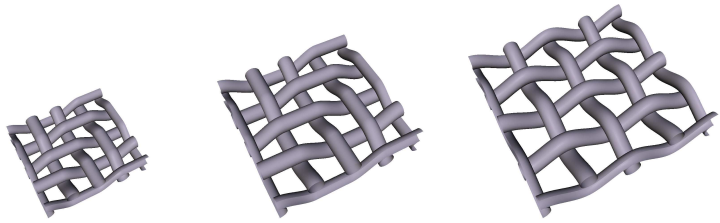

(a) small twill weave (b) large twill weave (c) plain weave

Figure 6.1: Three different wired square weaves are used in this work: (a) small twill weave with $w = 20\,\mu m$ and $d = 20\,\mu m$; (b) large twill weave with $w = 36\,\mu m$ and $d = 28\,\mu m$; (c) plain weave with $w = 50\,\mu m$ and $d = 30\,\mu m$. The images are adapted from Schober et al. [90].

It forms a so-called twill weave, which is characterized by its diagonal pattern resulting from the over-over-under-under braiding. The second weave (b) used in this work is also a twill weave, but with different geometric parameters $w = 36\,\mu m$ and $d = 28\,\mu m$. The most open-pored sample (c) is referred to as a plain weave with $w = 50\,\mu m$ and $d = 30\,\mu m$. Plain weaves represent the most basic types of weaves and are characterized by their simple crisscross pattern (over-under-over-under).

In principle, wired weaves offer great advantages with regard to the analyses of this work in comparison to real filter media. These are attributable to the simple design on the one hand and to the conductive material on the other. Both are clarified in more detail below.

Simple and regular design. The single-layer regular structure of wired square weaves facilitates the modeling and reduces the simulation effort. Due to the uniform pore sizes and the repeating structure, the required representative volume elements are much smaller compared to complex cabin air filter media. Wired weaves and real filter media additionally differ considerably in thickness. For these two reasons, the domain sizes for wired weaves can be chosen significantly smaller, resulting directly in lower memory requirements and reduced simulation runtimes. Furthermore, the modeling of wired weaves is cheap. No expensive xCT-scans are required, but the structures can easily be digitized by stringing piecewise defined

polynomial functions together. Fluctuating thicknesses, packing density or fiber diameter gradients due to the manufacturing process of filter media do not occur with wired weaves. This way, both simulations and experiments can be reproduced more easily. Since there are no deviations in the structure, two different samples should lead to very similar results.

Conductive material. So far, the superimposed acting of electrostatic separation mechanisms introduced in Sec. 2.1 have prevented the validation of individual contributions in the simulation. As briefly motivated above, the wired weaves can be grounded in the test facility. The resulting completely discharged filter media offer new possibilities in terms of studying electrostatic deposition mechanisms. The wired weaves, which no longer carry electrostatic charges, eliminate the usually important fiber-particle interactions, i.e., Coulomb and induced dipole effects, in experimental measurements. If the particles remain untreated at the same time and, thus, are electrostatically charged, only two electrostatic effects are left to support the mechanical particle collection: Firstly, the mirror charge effects proposed in literature and, secondly, the effects by mutual interactions of electrostatically charged particles in the inflow area, which are the main focus of this thesis. Thus, wired weaves are well-suited for verification purposes of separate filtration mechanisms. The influence of both effects on the filtration behavior are revealed in the remainder of this chapter. Another benefit of wired weaves is that, in addition to discharge, a controlled electrostatic charging is conceivable. This would allow validating the simulation methods with regard to further mechanisms not examined in this work.

6.2 Experimental Analysis

Experimental measurements of wired weaves are readily accessible as the existing, reliable filter media test rig described in Sec. 2.2.1 can be utilized. In contrast to the analysis of the particle behavior in an empty test channel carried out in Chapter 5, the collection efficiency of an installed filter medium or a wired weave as a filter substitute is evaluated in this section. The complexity caused by flow influences, particle deposition on and detachment from the channel walls thus remains and is further increased by additional fiber-particle and fiber-flow interactions. The

choice of the sample section is assumed to be of subordinate significance since irregularities and fuzziness (known from real filter media) do not occur with wired weaves. Hence, the simple structures are bound to provide a better reproducibility compared to complex cabin air filter media.

The aim of the experimental analysis is to identify physical as well as methodological effects which occur during the measurement of filtration performances. In addition, the impact of the identified effects on the collection efficiency of wired weaves is to be determined. The three different geometries illustrated in Fig. 6.1 serve to show the influence of fiber diameters and pore sizes. In order to characterize the methodological effects, some fundamental investigations concerning sensor positions (see Sec. 2.2.1) and particle measurement techniques (see Sec. 2.2.4) are conducted. Furthermore, the electrostatic charges carried by dust particles are of particular interest. Their influence on the filtration efficiency is analyzed by connecting the corona discharge module. These electrostatic effects have not been part of previous studies on metallic filters by Warth [105]. The characteristics of the analyzed scenarios as well as the corresponding results achieved are presented in detail below.

6.2.1 Experimental Testing Setups

As already in Chapter 5, the modular filter media test rig (MFP 3000) is used for all experimental measurements with wired weaves. The fractional collection efficiency η_{ww} of the respective wired weave is calculated according to Eq. (2.3) from the ratio of the number of collected particles $(N_{\mathrm{inlet}}(d_{\mathrm{P}}) - N_{\mathrm{outlet}}(d_{\mathrm{P}}))$ of the size class d_{P} to the respective number of particles in the inlet distribution $(N_{\mathrm{inlet}}(d_{\mathrm{P}}))$. In this case, the variables $N_{\mathrm{inlet}}(d_{\mathrm{P}})$ and $N_{\mathrm{outlet}}(d_{\mathrm{P}})$ refer conventionally to the respective number of particles in the raw and the clean gas. The test conditions for analyzing the filtration performance of wired weaves are summarized in Tab. 6.1.

The different variations of the modular testing units used to analyze the influence of the sensor position, the particle measurement technique and the electrostatic particle charge are introduced below.

Parameter		Value
Test dust		ISO fine dust
Dust concentration	c	$75\,\mathrm{mg/m^3}$
Volume flow rate	$\dot{V}$	$25.2\,\mathrm{l/min}$
Media velocity	v	$4.2\,\mathrm{cm/s}$

Table 6.1: Constant test conditions used for measuring the filtration efficiencies of wired weaves. The volume flow rate and media velocity correspond to the flow conditions between the two measuring positions, i.e., at the height of the wired weave. Due to the continuous particle removal at both measuring points, the flow conditions upstream the first and downstream the second sampling point deviate from the mean flow.

Sensor Positions. Analogous to the empty test channel examined in Sec. 5.3, the effect of different aerosol sensor arrangements is first investigated. Since the measurement results using the exchanged sensor setup have already excluded an influence of the two (ideally identical) sensors, the focus with regard to wired weaves is on the measuring position of the raw gas particle distribution. The following two configurations are used for this purpose:

The **upstream & downstream setup** introduced in Sec. 2.2.1 was already used for the analysis of particle dynamics in the empty test channel in Sec. 5.3.1. Therefore, only reference is made to those two sections at this point. The fractional separation efficiency of wired weaves can directly calculated from the quasi-simultaneous measurement of raw and clean gas distribution. Since no substantial increase in pressure is expected in the case of the open-pored weaves, stepwise measurements during dust loading are carried out. This means that the filter medium is continuously loaded with dust over a period of time (20 min) and the fractional efficiency is determined after every minute. This loading measurement is performed twice for each weave geometry, using a new, clean sample each time.

In the **downstream-only setup**, the particle size distributions of raw and clean gas are carried out at the same sample collection point, i.e., downstream the filter medium, with the same sensor. This requires an intervention in the test facility between the two measurements according to the following

procedure: The raw gas distribution is determined in a pre-measurement in the empty test channel. Afterwards the filter medium or wired weave is inserted into the test bench and the clean gas distribution is subsequently measured in a second operation. For raw and clean gas distributions, three measurements are consecutively carried out. In each measurement, the particles arriving in the measuring volume during one minute are accumulated.

The clean gas distribution is measured at the same position, i.e., downstream the wired weave, in both setups. The intention of using the two different setups is to verify a potential influence of the raw gas sensor position on the separation efficiency. For an empty test channel, the measurements in Sec. 5.3 revealed a similar particle size distributions at both measuring points. However, since an inserted wired weave changes the flow conditions, the results may not be transferable. Therefore, the influence of the sensor position is examined again in this chapter under the modified conditions.

Particle Measurement Techniques. In addition to the sensor configurations, the effects of different particle measurement techniques on the collection efficiency are examined in this section. Two particle sizing instruments, which are already introduced in Sec. 2.2.4, are applied:

In the case of the **optical particle counter (OPC)**, the results obtained from the sensor position analysis (downstream-only setup) are reused. As mentioned above, the optical diameter of particles is measured using a light-scattering spectrometer.

The **aerodynamic particle sizer (APS)** is also used in combination with the downstream-only setup as only one measuring device is available. In this case, the aerodynamic diameter of particles is determined.

Due to the non-spherical shape of the dust particles, certain differences are expected between optically and aerodynamically measured particle size distributions. An approximate conversion formula proposed in the standard DIN 71460-1 [27] is given in Eq. (2.5). This equation is applied to the measured diameters of this section and the obtained results are additionally evaluated. The investigations with different particle measurement techniques are mainly motivated by the fact that spherical

particles are modeled in both simulation approaches. Therefore, the question arises whether one of the measurement methods is better suited for comparison with simulation results. For direct comparability of the measuring instruments, the same, downstream-only setup is used in both cases.

Particle Charging States. Finally, the influence of electrostatically charged particles on the separation behavior of wired weaves is analyzed. The corona-discharge unit already applied to particles in the empty test channel in Sec. 5.3.2, is used to obtain modified charging states. Again, the behavior of untreated (charged) particles and discharged particles is examined.

> **Untreated (charged) particles** have already been used for the above mentioned analysis of sensor positions and particle measurement techniques. The respective measurement results are reused to determine the influence of the particle charging state.
>
> **Discharged particles** are examined with the same sensor setups for this purpose. For the basic principles of discharging particles, reference is made to Sec. 2.2.3 at this point.

The measurements with different charging states for particles are carried out using the optical particle counter in combination with the upstream & downstream setup and using the aerodynamic particle sizer in combination with the downstream-only setup. Since the wired weaves are grounded in the test facility, as described in Sec. 6.1, any differences in the experimental results can directly be attributed to the particle charging state. The aim of the experiments is to quantify the influence of electrostatic effects such as mirror charges on the collection efficiency.

In order to additionally take the influence of different pore sizes and fiber diameters into account, all experiments in this chapter are carried out for the three wired weave geometries depicted in Fig. 6.1. A detailed evaluation of the experimental results is provided below.

6.2.2 Experimental Testing Results

In this section, the results obtained by the various experimental processes described above are presented. This includes the measured fractional collection efficiencies with different sensor positions, with different particle measurement devices and the analysis of corona discharged dust particles. The results are presented in the same order as the experimental setups were introduced.

Influence of the Sensor Position. In an initial step, the interplay between sensor position and weave geometries on the measured collection efficiency η_{ww} is investigated using the upstream & downstream setup with a light-scattering spectrometer (OPC). The left-hand side of Fig. 6.2 summarizes the experimental results depending on the measured particle diameters. The individual graphs for each wired weave show the mean values of all recorded data during two dust loading measurements over 20 minutes and the associated standard deviations.

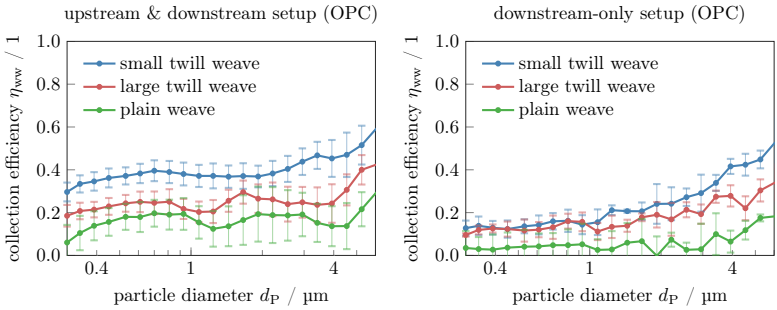

Figure 6.2: Experimentally determined fractional collection efficiencies η_{ww} for the three weave geometries presented in Fig. 6.1. The particle size distributions in raw and clean gas required for calculating the collection efficiencies are determined by an optical particle counter. The upstream & downstream setup (left) refers to the arrangement of two particle sensors upstream and downstream the wired weave. The downstream-only setup (right) consists of only one sensor, which is located downstream the filter medium. The measured differences using the two setups only refer to the very open-pored wired weaves.

In comparison to the collection efficiencies of electrostatically charged cabin air filter media, which are usually well above 90 %, the single-layer and open-pored wired weaves are naturally inferior. Nevertheless, the simple filter substitutes are well suited for the basic investigations in this work. The plots indicate that the enlargement of the pore size, which is also accompanied by an increase in the fiber diameter, virtually leads to a parallel shift towards lower collection efficiencies. For all weave geometries, non-smooth curves as well as fairly high fluctuations are observed. These are caused by the combination of the operating principle of the optical particle counter with the highly, non-spherical shape of dust particles. The larger the shape factor (non-sphericity), the greater the influence of the particle orientation on the scattered light and, thus, the measured particle diameter. Due to the low separation efficiencies compared to real filter media, the collection depends very much on the steadiness of aerosol provision, which further contributes to the large scatters.

The influence of continuous dust loading on the results is displayed on the left-hand side of Fig. 6.3, where the collection efficiencies are plotted for the finest weave ($w = d = 20\,\mu\text{m}$) after different loading times t. Again, the mean values from both loading measurements are used. For a clearer presentation, the standard deviations are omitted in this case. The plot shows large differences between the measured collection efficiencies at different times, which are the reason for the large scattering in the previous plot. However, a clear trend with increasing loading time is not observable. Particle accumulation on the wired fibers is, therefore, low enough within the measuring period such that subsequent dust particles are not affected. Hence, averaging over all measurement (after different loading times) series is justified.

The right-hand side of Fig. 6.3 shows the associated collection efficiency of specific particle diameters over time. Again, there is no significant change (relative to the scattering magnitude) with continuous dust loading. The graph further indicates that the scattering strongly increases for the largest displayed particle size. This effect is also reflected by the vanishing smoothness of the collection efficiency for particles with $d_\text{P} = 8.1\,\mu\text{m}$. The reason for this is the small number of large particles in the system according to the ISO fine dust distribution plotted

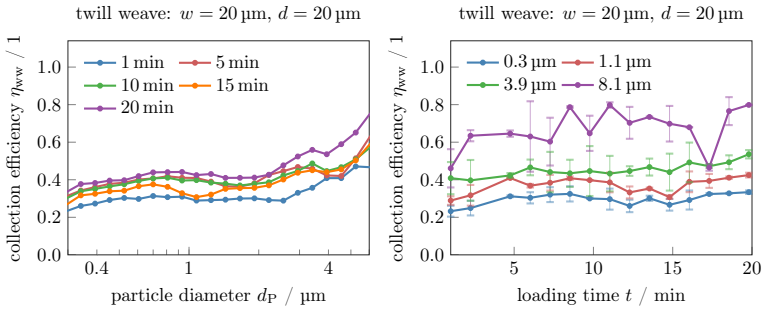

Figure 6.3: Mean collection efficiencies of the finest wired weave determined by two dust loading measurements using the upstream & downstream setup with an OPC. The fractional collection efficiencies are plotted after different loading times (left). For the sake of clarity, the standard deviations are omitted in this case. Furthermore, particle size specific collection efficiencies are shown with increasing dust load (right).

in Fig. 5.2. With a number of less than $N_{raw}(8.1\,\mu m) = 100$ particles in the measuring volume, even a few particles have a high influence on the resulting collection efficiency. The observations from both plots in Fig. 6.3 also apply to the particle collection of the two coarser wired weaves, which are therefore omitted at this point.

After the analysis of the collection efficiencies with the upstream & downstream setup, the results obtained by the downstream-only setup are analyzed in comparison. The right-hand side of Fig. 6.2 shows the associated measured fractional collection efficiencies. The mean values and the standard deviations from three measurement series carried out for each wired weave are presented. Again, the finest weave tends to collect the most particles. However, the differences between the individual wired weaves do not reflect a parallel shift, but depend on the particle size in this case. For instance, the collection efficiencies of the two twill weaves hardly differ for submicron particles. For larger particles, however, clear differences are observable. When comparing the two different sensor arrangements, the upstream & downstream setup provides significantly higher collection efficiencies over the entire particle spectrum for all wired weaves. Since the actual deposition of particles on the wired weave is independent of the sensor positions, the differences

indicate that further effects occur between the two measurement points. However, several possible effects, which could have also been relevant in this context, have already been discarded in Chapter 5. The particle behavior in the empty test channel has been thoroughly investigated with the following conclusions:

Electrostatic agglomeration. The particle size distribution does not change between upstream and downstream particle sampling points. Although electrostatic agglomeration takes place, it is already completed before the first measuring position.

Different sensors. In order to measure the particle size distribution in the raw and the clean gas quasi-simultaneously, two different (identical in construction) sensors must be applied. Both sensors provide the same results.

Wall influences. A deposition of dust particles on and detachment from the inner test channel walls takes place to a small extent, but does not lead to a measurable influence on the collection efficiency.

Volume flow rate. Due to the continuous removal of particles at the first measuring point, the volume flow rate at the second measuring point is theoretically diminished. However, the volume flow rate difference is too small to have a measurable influence on the particle size distribution.

An influence of these factors on the (artificial) filtration efficiency in the test channel is thus excluded. Therefore, the difference in the measured fractional efficiencies of wired weaves can neither be directly attributed to the particle dynamics in the flow field nor to the actual particle deposition at the filter medium. One possible explanation is the combination of both factors. In an empty test channel, no differences depending on the sensor position (upstream & downstream or exchanged sensors) can be detected for most particle size classes. The differences only occur as soon as a wired weave is inserted into the test channel. Complex flow pattern caused by this wired weave may be a possible but unlikely reason for non-uniform particle distributions in cross-sectional and longitudinal direction of the test channel. However, the differences detected at this point only refer to the very open-pored wired weaves. For highly efficient cabin air filter media, these differences are not necessarily transferable. The deviations between the different sensor setups are not examined any further at this point as they are not the focus of this thesis.

Influence of the Particle Measurement Technique. The measurement results on the left-hand side of Fig. 6.4 obtained by the optical particle counter have already been presented above (see Fig. 6.2). The plot on the right-hand side, by contrast, shows the fractional collection efficiency achieved with the aerodynamic particle sizer using the same, downstream-only setup.

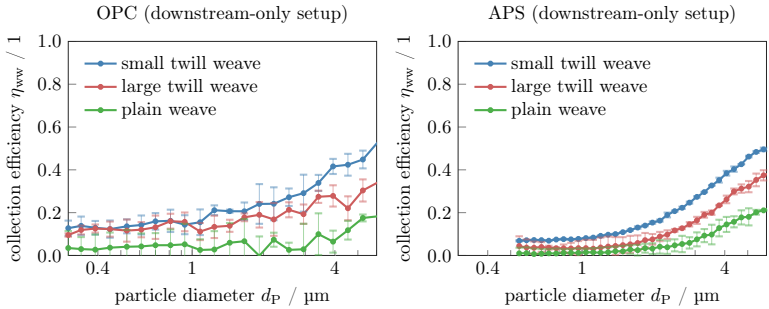

Figure 6.4: Fractional collection efficiencies obtained using the identical (downstream-only) experimental setup, but with different particle measurement techniques. Raw and clean gas distributions are measured with an optical particle counter (left) or with an aerodynamic particle sizer (right).

For all three wired weaves, the curves are much smoother compared to the OPC based fractional collection efficiencies. Thereby, the transition from diffusion to inertial separation is more pronounced. This variation of the effective collection mechanism is evident from the clearly recognizable change of the gradient in the range of $d_P \approx 2\,\mu m$. Furthermore, the scattering of results for the aerodynamic particle sizer is comparatively low and sometimes not visible at all. As already mentioned above, one plausible explanation for the high scattering with the OPC device is the light reflection from non-spherical particles. A rod-shaped particle, for example, can be assigned to completely different particle size classes depending on its orientation to the radiation source. The aerodynamic movement of the particle by contrast does not depend on the particle shape to such an extent resulting in reproducible smooth measurement results.

The direct comparison of the measuring instruments is given in Fig. 6.5 specifically for each wired weave. When using an identical experimental setup (downstream-only), the two measurement techniques result in relatively well matching fractional collection efficiencies. The agreement becomes even better if the conversion between optical particle diameters d_{OPC} and aerodynamic particle diameters d_{APS} according to Eq. (2.5) is taken into account. These converted results for the optically determined collection efficiencies are included in the respective plots. If the measuring accuracy through scatters is taken into account, the remaining deviations are highly satisfactory. Basically, the APS measurements result in smoother curves with less scattering. This effect has already been attributed to the particle measurement techniques used. However, note that only two measurement series are used to calculate the standard deviations (compared to three series with the OPC).

Influence of Particle Discharging. The influence of discharging the particles is investigated separately for both measuring instruments. Firstly, the effect of electrostatic particle charges in combination with the upstream & downstream setup and the optical particle counter is shown in Fig. 6.6.

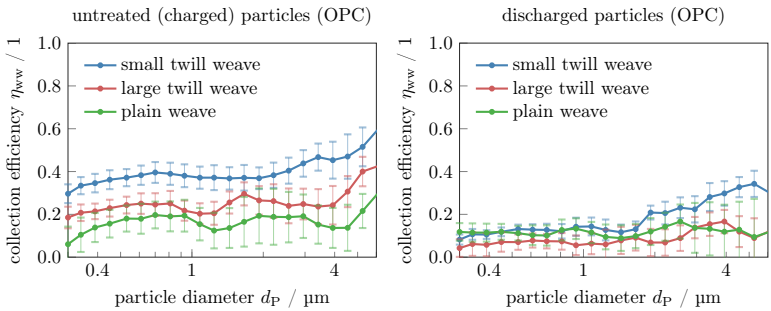

Figure 6.6: Fractional collection efficiencies obtained with untreated (left) and corona discharged (right) particles for all three wired weave geometries. All measurements are carried out using the light-scattering spectrometer (OPC) and the corresponding upstream & downstream setup.

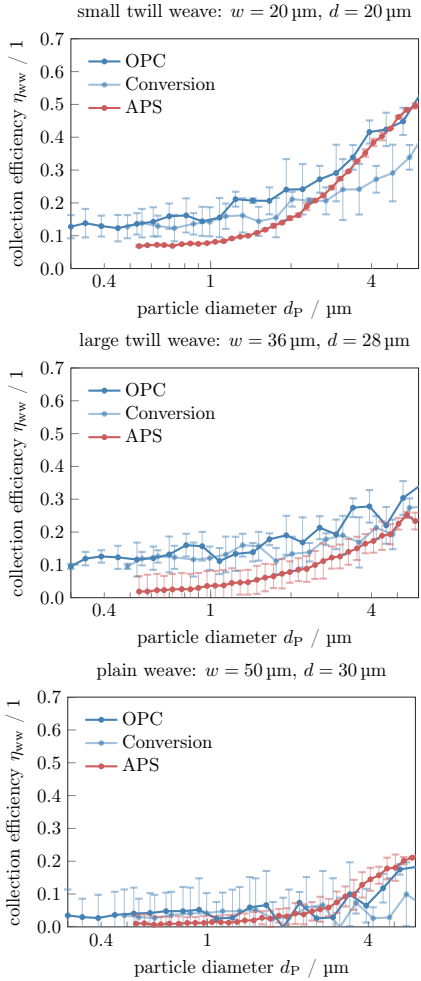

Figure 6.5: Initial fractional collection efficiencies η_{ww} for three different wired weaves measured with different particle measurement techniques. The results obtained by an aerodynamic particle sizer (APS) are compared to those obtained by an optical particle counter (OPC). For a better comparability of the measurement techniques, the downstream-only setup is used in both cases.

On the left-hand side, the already known collection efficiencies for untreated (charged) particles (see Fig. 6.2) are plotted, whereas, on the right-hand side, the collection efficiencies for corona discharged particles are shown. The high scattering resulting from the OPC device is observed for both plots. Thus, the scattering is not ascribed to the strong fluctuations of the particle charges. The explanation given by the shape factor of dust particles, however, is reinforced by the repeated scattering with discharged particles.

Discharging the particles during the insertion into the test channel leads to a significant decrease in the measured separation efficiency for all investigated wired weaves. Furthermore, the order of the fractional collection efficiencies for the individual weaves changes: The finest twill weave still displays the highest collection efficiency for almost each particle diameter. The two coarser weaves change their order for most particle size classes such that the plain weave no longer leads to the lowest performance. Due to the still very similar collection efficiency in connection with the high scatters, however, this rearrangement is not significant.

The same examination is carried out using the aerodynamic particle sizer. Figure 6.7 shows the respective plots for untreated (left) and discharged (right) particles. In combination with the APS device, the downstream-only setup is used again to determine the respective particle size distributions.

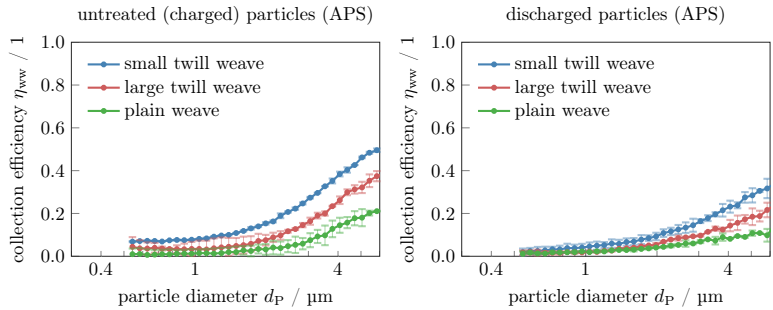

Figure 6.7: Fractional collection efficiencies obtained with untreated (left) and corona discharged (right) particles for all three weave geometries. All measurements are carried out with the aerodynamic particle sizer (APS) and the corresponding downstream-only setup.

In this case, the differences between untreated (charged) and discharged particles are also present, but less pronounced. One reason for this minor effect is the already very low collection efficiency measured for untreated (charged) particles. With the measuring technique of aerodynamic particle diameters, the ranking of the three weave geometries remains the same. For small particles, however, there is almost no difference between the collection efficiencies of the individual weaves. All wired weaves show a negligible low particle collection in this area.

The two final diagrams of this section display the influence of particle charges on the collection efficiency specifically for each wired weave. The comparison between untreated (charged) and discharged particles is shown for the OPC in Fig. 6.8 and for the APS in Fig. 6.9. The quasi-simultaneous measurement with the optical particle counter leads to very clear differences in the collection efficiency of untreated (charged) compared to discharged particles. Especially for the two twill weaves, separation is extremely reduced if the particles are discharged beforehand. As the coarseness of the weave geometry increases, the difference decreases steadily. This effect is attributed to mirror charges, which occur when electrostatically charged particles move in the vicinity of a fiber. The resulting attractive forces lead to an increased collection efficiency as described in Sec. 2.1.1. For smaller pore sizes, particles get closer to the fibers and the mirror charge effects increase. In addition, the potential surface area for mirror charges increases with smaller wire diameters. These findings have already been published prior to this thesis [90].

The same experiment using the APS device and the downstream-only setup results in the same trend, but the differences are less pronounced. Since particle size distributions are only measured downstream the wired weave, the plots show the actual difference of the deposition on the filter medium, whereas the OPC based measurements potentially involve further effects due to the different sensor positions and flow conditions. The results indicate that the particle charge strongly influences the separation of large particles. For these particles, the mirror charge effects are more pronounced as they feature a broader charge distribution (see Fig. 5.5) and, thus, are partially highly charged. In contrast to the empty test channel, where the particle charges had no impact at all, the electrostatic particle charges have a significant influence in combination with the conductive weaves.

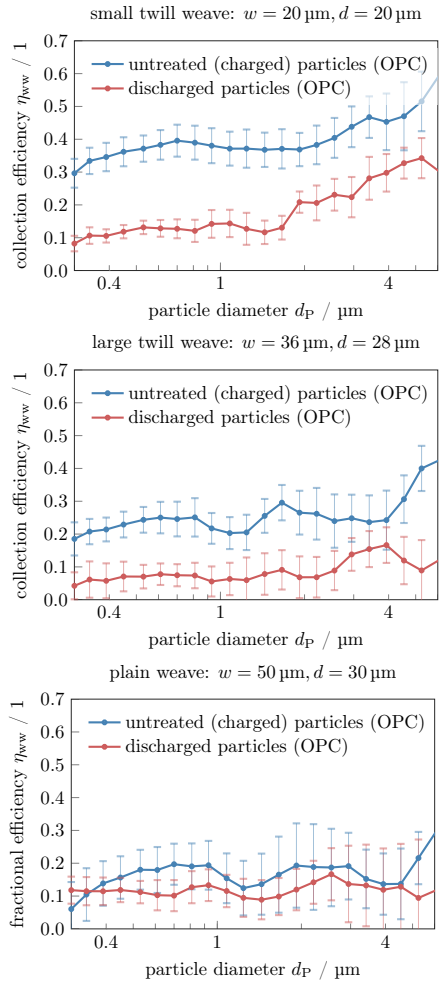

Figure 6.8: Initial fractional efficiencies for the three different wired weaves using untreated (charged) particles in comparison to corona discharged particles. The results are obtained by measuring optical particle diameters with the light-scattering spectrometer in the upstream & downstream setup.

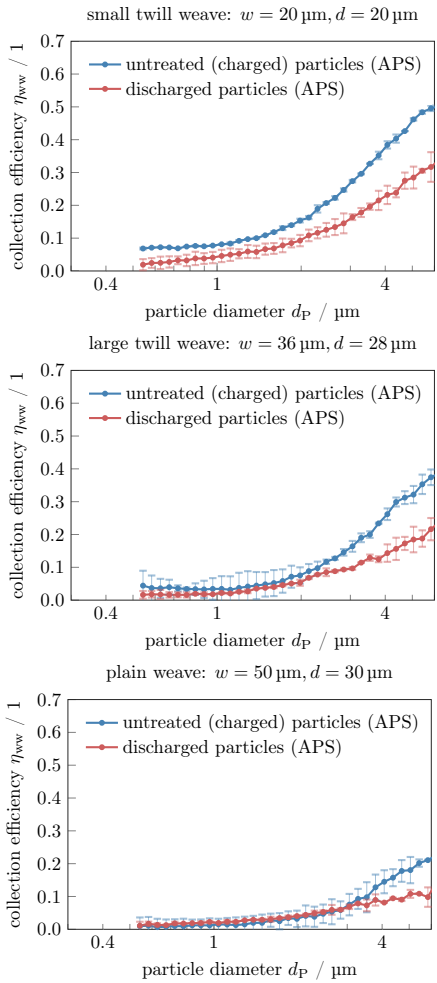

Figure 6.9: Initial fractional efficiencies for the three different wired weaves using untreated (charged) particles in comparison to corona discharged particles. The results are obtained by measuring aerodynamic particle diameters with the APS device in the downstream-only setup.

6.3 Simulation Study

The simulation studies in this chapter directly build on the single fiber simulations in Sec. 4.1. The single fiber model served to simulate already familiar mechanical collection mechanisms with the novel fully-coupled simulation approach. The achieved collection efficiency η_{SF} showed excellent agreement with the simulation results obtained with the well-established uni-directional coupling approach as well as with latest published data. However, exploiting the full potential of the fundamentally new four-way coupled simulation approach was not possible by means of the single fiber. The modeled setup was too small to include the particle-particle interactions of interest in the inflow area. The extension to a network of individual fibers, i.e., a wired weave, finally allows exploiting the advantages of the new simulation method. The aim of the simulation studies is to determine the influence of electrostatic particle-particle interactions on the particle deposition on wired weaves. Therefore, the results from the uni-directional coupling method, i.e., neglecting particle-particle interactions, are compared with the four-way coupled method for neutral and electrostatically charged particles. The detailed simulation setups and the associated results are presented in the remainder of this section. The presentation follows the work published prior to this thesis [91].

6.3.1 Simulation Experiment Setup

In a first step, the trajectories of completely neutral particles through a simplified fiber network are analyzed. The electrostatic neutrality of the entire system (the filter medium is considered grounded as in the experimental testing) means that strong long-range Coulomb forces are omitted in the newly deployed fully-coupled simulation approach. It is assumed that particles do not collide with each other, which in turn allows neglecting the short-range MD potentials, i.e., the Hertzian and the harmonic bond potential. This reduces the coupling degree from four-way to bi-directional. Particles can therefore only interfere with each other via the background flow field. The difference of applying the bi-directional and the established uni-directional simulation approach between particles and the air flow field is analyzed. For these preliminary investigations, a simplified model of the wired weaves is applied. The simple network of intersecting fibers is depicted

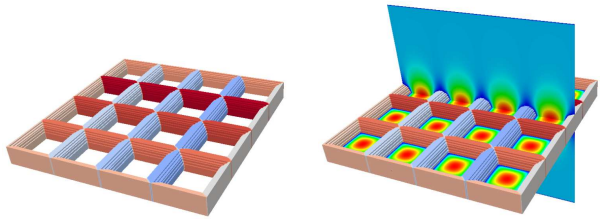

Figure 6.10: Experiment setup (left) consisting of uniformly aligned cylindrical fibers creating a mesh for the simulation of neutral particles. In addition, sliced plots of the velocity magnitude of the resulting flow field through the geometry are presented (right). The shown flow simulation shown is carried out using the Lattice-Boltzmann method implemented in the software package ESPResSo. The images are adapted from Schober et al. [91].

on the left-hand side of Fig. 6.10. The cylindrical fibers are uniformly aligned resulting in square shaped pores. As a first step of the simulation, the initial flow field is calculated with each of the two coupling approaches. For this purpose, a cubic domain is chosen, which is indicated on the right-hand side of Fig. 6.10. In addition to the fiber geometry, two-dimensional slices of the converged flow field are plotted. The simulation domain has a size of $(200 \times 200 \times 200)\,\mu\text{m}^3$ and is periodic in each direction for the flow field as well as for the particles. In order to obtain realistic results, the flow resolution around the fibers must be chosen sufficiently high. A grid spacing of $a = 1\,\mu\text{m}$ is therefore applied for the LIR solver implemented in the software package GeoDict as well as for the Lattice-Boltzmann method implemented in the software package ESPResSo. With these parameters, the calculation is already at the limit of what is possible in terms of memory for the used graphics processing unit NVIDIA Titan X (Maxwell).

Subsequently, 20 spherical monodisperse particles with a diameter of $d_\text{P} = 2\,\mu\text{m}$ are added at the top of the simulation domain. The particles are distributed statistically, but added to the flow fields with exactly the same starting positions for each simulation approach. As the simulation domain is relatively small, the resulting particle concentration $c_\text{P} = 2.8 \cdot 10^{-2}\,\text{kg/m}^3$ is excessively high compared to the values from experimental testing ($c_\text{P} = 7.5 \cdot 10^{-5}\,\text{kg/m}^3$). This way, a reasonable number of particles in the simulation domain is achieved. An overview

Parameter		Value
Interception parameter	R	0.1
Particle density	ρ_P	$2650\,\mathrm{kg/m^3}$
Particle concentration	c_P	$2.8 \cdot 10^{-2}\,\mathrm{kg/m^3}$
Mean velocity (Air)	u_air	$0.2\,\mathrm{m/s}$
Dynamic viscosity (Air)	η_air	$1.834 \cdot 10^{-5}\,\mathrm{kg/(m\,s)}$
Density (Air)	ρ_air	$1.204\,\mathrm{kg/m^3}$

Table 6.2: Overview of the parameters used for the simulation of trajectories of neutral particles through the simple mesh model depicted in Fig. 6.10.

of all simulation parameters used is given in Tab. 6.2.

In the second, main experiment, the focus is on the influence of electrostatic particle-particle interactions during particle motion. The structure of the simple plain weave is modeled more precisely for this purpose. The simulation procedure is the same as for neutral particles. However, the dust concentration is reduced by an order of magnitude to $c_\mathrm{P} = 2.8 \cdot 10^{-3}\,\mathrm{kg/m^3}$ such that only two particles are tracked. This is necessary due to the high forces between the electrostatic charge points. Since the particles are very close together, very low particle charge intensities $q_1 = +2\,e$ and $q_2 = -1\,e$ are used with e being the elementary charge $e = 1.602 \cdot 10^{-19}\,\mathrm{C}$. The parameters shown in Tab. 6.2 are used again except for the deviations mentioned above, i.e., dust concentration and particles charges.

6.3.2 Numerical Results

As mentioned above, the influence of the retroactive forces of the background flow field on the movement of electrostatically neutral particles is investigated first. After the precise analysis of the resulting trajectories through simplified filter designs, the fractional collection efficiency η_ww is simulated for the three wired weave geometries, which are also examined in the experimental investigations. Subsequently, the challenging influence of electrostatic charges on dust particles is investigated. For all simulation runs in this section, the calculation of the initial flow field through the filter media is necessary. The stand-alone flow field for the used mesh is plotted on the right-hand side of Fig. 6.10. At this point, ESPResSo and GeoDict provide no visible differences regardless of the used solver.

6.3.2.1 Electrostatically Neutral System

This section focuses on the simulation of the movement of uncharged particles. Since the meshes or wired weaves are also considered electrostatically neutral, there are no charges present in the entire system. Therefore, it represents the simplest of the investigated cases.

Particle trajectories. On the basis of three different flow solvers, i.e., Stokes (LIR) solver, Navier-Stokes (LIR) solver and Lattice-Boltzmann solver, the movement of neutral particles through the simple mesh geometry introduced in Fig. 6.10 is calculated. Refer to Sec. 2.3 and Sec. 3.4 for the fundamentals of the respective solvers implemented in the software packages GeoDict and ESPResSo. The cross-section of the simulated trajectories for 20 particles are plotted in Fig. 6.11. The starting positions of the particles are identical for all three simulation runs.

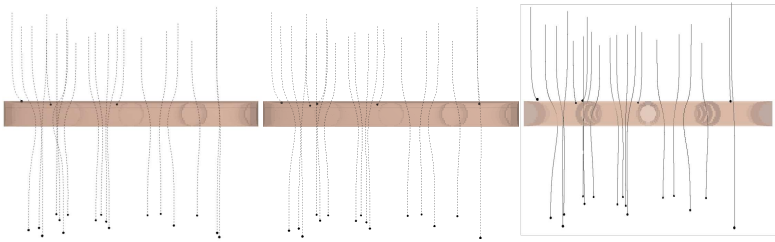

(a) Stokes (LIR) (uni-directional) (b) Navier-Stokes (LIR) (uni-directional) (c) Lattice-Boltzmann (bi-directional)

Figure 6.11: Particle trajectories of 20 electrostatically neutral particles through the mesh structure depicted in Fig. 6.10. The background flow fields are based on different flow solvers implemented in the software packages GeoDict and ESPResSo: (a) Stokes solver, (b) Navier-Stokes solver and (c) Lattice-Boltzmann solver. The two plots on the left-hand side result from the uni-directional coupling method implemented in GeoDict, the trajectories on the right-hand side are based on the bi-directional coupling between particles and background flow field implemented in the software package ESPResSo. The images are adapted from Schober et al. [91].

The two plots generated with the uni-directional coupling implemented in the software package GeoDict show minimal deviations in the simulated particle trajectories. These discrepancies lead to the fact that only three out of 20 particles collide with the fiber braid when using the Stokes solver, but five particles are collected based on the Navier-Stokes background flow field. As a consequence, different collection efficiencies are obtained for the small amount of simulated particles depending on whether inertia effects are taken into account or neglected. Thus, the simulation results point out that there is no Stokes regime for the given flow parameters. Therefore, the non-simplified Navier-Stokes equations are used for all further uni-directionally coupled simulations in this chapter.

The results from particle tracking using the bi-directional coupled simulation implemented in the software package ESPResSo are shown in the rightmost plot of Fig. 6.11. Using the Lattice-Boltzmann method for the background flow leads to the same particle deposition as with the Navier-Stokes solver. A quarter of the particles come into contact with the fiber surfaces at identical positions. The retroactive forces of particle motion on the fluid flow therefore do not affect neighboring particles in this simple scenario. As long as the filtration of uncharged particles in uncharged filter media is simulated, the uni-directional coupling approach leads to reasonable results. Since the particle concentration is already about three orders of magnitude higher than in the laboratory experiments, no influence for neutral particles is expected for larger simulation experiments.

Collection efficiencies. In order to simulate meaningful collection efficiencies, significantly more particles are required. Since the interaction between incoming particles via the fluid does not influence their trajectories, the simple and computationally efficient uni-directional coupling approach can be applied. In contrast to the bi-directional coupling method implemented in ESPResSo, the particle concentration can be increased arbitrarily without any effect on the particle movements. Thus, the applied simulation method allows simulating high particle counts with feasible memory and runtime effort. The resulting fractional collection efficiencies for the three weave geometries are plotted in Fig. 6.12.

All wired weaves show very low collection efficiencies for small particles with $d_P < 1\,\mu m$. Neither diffusion nor inertial collection mechanisms are effective in this

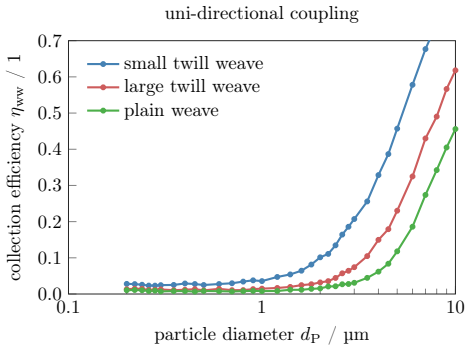

Figure 6.12: Fractional collection efficiencies η_{ww} for the three weave geometries (see Fig. 6.1) simulated with the uni-directional coupling method implemented in the software package GeoDict. Both, the wired weaves and the 10000 simulated particles for each particle diameter are considered electrostatically neutral.

particle size range. The finest twill weave still stands out minimally from the two others. For larger particles, a rather sharp increase in the collection efficiency is observed in all plots. In addition to the improved efficiency due to inertia, this sharp increase is also attributed to the applied caught-on-first-touch method for particle collisions. The gradient of the curves is the same for the three simulated weaves. Only the point at which the collection through interception and inertia becomes effective differs for the weaves. The transition takes place at particle diameters $d_P \approx 2\,\mu m$ for the finest wired weave compared to $d_P \approx 4\,\mu m$ for the coarse, plain weave. The pore size and fiber diameter thus determine this transition range. Due to the different activation points for additional mechanical deposition, the collection efficiency differs considerably for large particles.

6.3.2.2 Electrostatically Charged Particles

Tracking electrostatically charged particles requires the integration of long-range Coulomb forces as well as modeling particle collisions as described in Sec. 3.2.3 and Sec. 3.2.1. Hence, the potential of the four-way coupled system is fully exploited in the following simulation runs. The trajectories of two oppositely charged particles

are displayed in the picture series on the left-hand side of Fig. 6.13 according the setup described in Sec. 6.3.1. For an easier interpretation of the results, a simulation with the same particle starting positions is executed without taking electrostatic interactions into account. The resulting trajectories of two neutral particles are plotted on the right-hand side of Fig. 6.13 at the exact same times as for charged particles. All plots exemplify the movement of the particles in the inflow area of the plain square weave. For better visualization, the particles are magnified and their complete trajectories are plotted.

The two picture series show an extremely different behavior of the simulated particles: Omitting the Coulomb potential, the particles move individually through the coarse pores of the plain weave, whereas the charged particles strongly interact with each other. Although the charged particles only carry extremely low electrostatic charges ($q_1 = 2\,e$ and $q_2 = -1\,e$) compared to the expected distribution plotted in Fig. 5.5, a strong attraction is observed. The particles initially only move perpendicular to the flow direction and immediately collide. Consequently, they already stick together well before they reach the fiber network. Subsequently, the particles pass through one of the pores as an agglomerate. Already the simulation of only two particles with the fully-coupled model shows that particle trajectories change dramatically if particle-particle interactions are properly modeled. Since the resulting agglomerates are heavier and, thus, their movement is more strongly driven by inertia than the one of the individual particles, a higher filtration efficiency is assumed. Although this effect can not be demonstrated on the basis of a single agglomerate, it should not be neglected upon designing filter media exploiting electrostatic effects.

The behavior of charged particles in the inflow area of the wired weave confirms the findings about electrostatic agglomeration in Chapter 5: The particle-particle interactions due to electrostatic forces are tremendously strong leading to immediate agglomeration. In the laboratory experiments, the particles are added at much greater distances from the filter medium than in the presented simulation experiment. The agglomeration is thus already completed before the dust particles pass the first measurement point in the experiments. Nevertheless, the agglomeration process changes the charge distribution and particle shape and must therefore be taken into account as soon as charged particles are simulated.

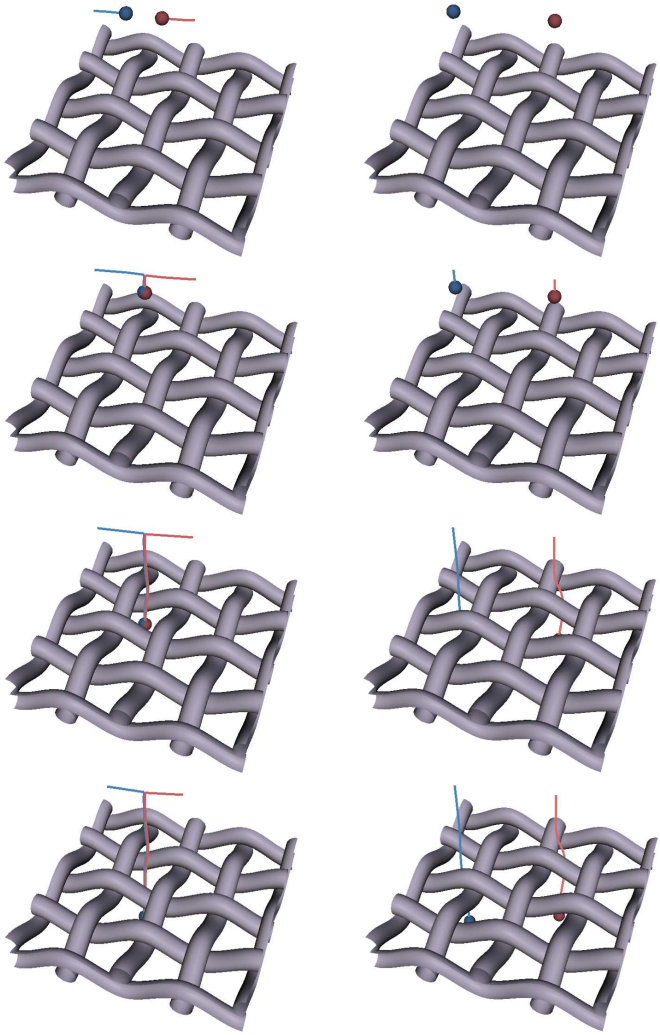

(a) charged particles (b) neutral particles

Figure 6.13: Particle trajectories of two electrostatically charged (left) or neutral (right) particles through the plain weave at different times. The simulation results are obtained using the fully-coupled approach implemented in the software package ESPResSo.

6.3.3 Remarks on Parallelization of the Simulations

The simulation studies presented above are computationally very intensive for two main reasons: Firstly, the number of Lattice-Boltzmann cells is very large due to the high resolution required around the filter fibers. The analyzed simulation domain in Fig. 6.13 measures $(320 \times 320 \times 320)\,\mu m^3$. A grid spacing of $a = 2\,\mu m$ yields $4.096 \cdot 10^6$ fluid cells. Secondly, the deposition of moving (dust) particles is realized by the formation of bonds with fixed, auxiliary particles placed in the filter structure (see Sec. 3.2.2). For a precise representation of the plain wired weave, 640 fixed particles are required. Therefore, parallelization of the simulation is essential in order to achieve results within reasonable runtimes. To evaluate the performance of the fully-coupled simulation approach and determine the optimal number of CPU cores to be used, a strong scaling experiment is performed. For this purpose, the runtime for 1000 time steps is measured using different numbers of CPU cores (with one MPI rank per core). The time step for the MD particles is chosen 1000 times smaller than the time step for the Lattice-Boltzmann method. One overall time step therefore consists of updating the individual physical subsystems (1000 short-range MD, 1000 long-range MD and one hydrodynamic time step) as well as a coupling step. In addition to the total runtimes, Fig. 6.14 shows their compositions of the individual components. The experiment is performed on Intel Xeon E7-8880v3 processors in a four-socket configuration (with 18 cores per socket).

At a first glance, an optimum of the total runtime with 16 CPU cores is apparent. With removal or further addition of processors, the runtime significantly increases. For the used simulation scenario (see left-hand side of Fig. 6.13) with 640 fixed particles, two moving (charged) particles and $4.096 \cdot 10^6$ Lattice-Boltzmann cells, the individual runtimes for short-range molecular dynamics (MD) and hydrodynamics (LB) naturally dominate. Since long-range interactions are only relevant for the very low number of dust particles, the runtime of electrostatics does make a large contribution. While the Lattice-Boltzmann method scales well up to 32 CPU cores, the MD runtime turns out to be more complex. Therefore, an additional distinction is made between the actual force calculation and the communication between adjacent processors to exchange particle information. When examining the split up MD runtime, the individual bars show that the underlying linked-cell algorithm (MD force calculation) also scales well, whereas the MD communication forms the

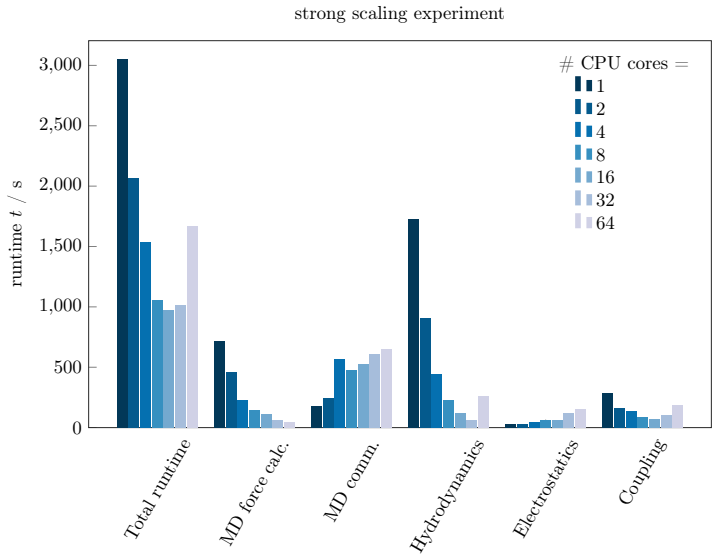

Figure 6.14: The runtime for 1000 overall time steps is measured in a strong scaling setup of the wired weave scenario. A single time step consists of updating the individual subsystems (1000 short-range MD, 1000 long-range MD, and one hydrodynamics time step) as well as a coupling step.

bottleneck. There is a substantial increase in the runtime for MD communication when using more than two cores. This longer runtime can be explained by the deployed simulation setup in combination with the decomposition of the simulation area into subdomains. The domain decomposition serves to distribute the computational load to the individual processors (one subdomain per processor). As shown on the left-hand side of Fig. 6.15, the filter structure is intersected vertically (blue plane) when dividing the domain into two subdomains. In this case, however, the plain weave is already cut along one filter fiber, which turns many of the (fixed) particles into so-called ghost particles. From four cores upwards, the wired weave is additionally cut horizontally (red plane). This significantly increases the number of particles in the ghost layers again and, thus, also extends the runtime for MD

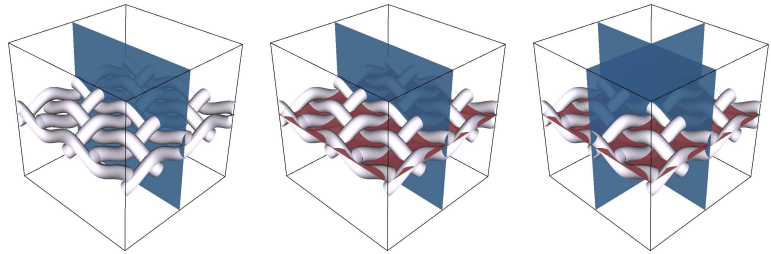

(a) 2 subdomains (b) 4 subdomains (c) 8 subdomains

Figure 6.15: Division of the simulation area into (a) 2, (b) 4 and (c) 8 subdomains, which are assigned to different processors. Each woven filter structure consists of 640 fixed MD particles in addition to the visible constraint in order to model particle deposition according to Sec. 3.2.2.

communication substantially. Moreover, Fig. 6.14 shows a very small contribution of the (generally very expensive) electrostatics to the total runtime. However, since there are only two charged particles in the simulation system, no further statements are possible at this point.

In addition to the runtimes on CPUs only, Tab. 6.3 summarizes the measured runtimes for the same experiment, but with outsourcing hydrodynamics to a GPU. The Lattice-Boltzmann runs on an NVIDIA Titan X (Maxwell) and molecular dynamics is simulated on an Intel Core i7-6700K processor. For comparison, the runtimes in which all components run on a single CPU core are listed. Note that different CPUs are applied in both experiments resulting in different runtimes for the MD components. Particularly remarkable is the runtime for the Lattice-Boltzmann method, which is reduced by a factor of 192 compared to a single CPU core. The runtime needed for the coupling, however, increases at this point. Nevertheless, combining the GPU with a CPU is the fastest analyzed system for the simulated filter scenario. For larger simulation setups, the GPU is, however, not suitable due to memory limitations. Hence, parallelizing the simulation of larger scenarios is very important in order to distribute the computational load among multiple processors (CPUs and GPUs) and ensure feasible runtimes.

System	1 GPU + 1 CPU core	1 CPU core
Total runtime	888 s	3052 s
MD force calculation	472 s	720 s
MD communication	48 s	178 s
Hydrodynamics	9 s	1726 s
Electrostatics	10 s	28 s
Coupling	316 s	287 s

Table 6.3: The runtime for 1000 fluid time steps is measured using a single GPU for hydrodynamics and a single CPU core for molecular dynamics. A single time step consists of updating the individual subsystems (1000 short-range MD, 1000 long-range MD, and one hydrodynamics time step) as well as a coupling step.

6.4 Comparison of Simulation Results with Experiments

Amongst others, the aim of this chapter is to evaluate the comparability of particles modeled as exact spheres with experimentally determined particle sizes. Hence, this section contrasts the experimental measurement and simulation results of fractional collection efficiencies. On the basis of the measurement results presented above, a better agreement is assumed for the aerodynamically determined particle size distributions. Therefore, the comparison of simulated collection efficiencies with experimental results is limited to this particle measurement technique.

6.4.1 Electrostatically Neutral System

Figure 6.16 shows the results for 'neutral' systems (the complete discharge is not ensured in experimental testings) of wired weaves and particles. For all three weaves, the aerodynamically determined measurement results show very good agreement with the simulated collection efficiencies. Thus, it can already be stated that the aerodynamic particle diameters of ISO fine dust fit well to the spherical particles of the simulation. Especially for small particles, an almost perfect agreement is observed. For large particles, the simulated filtration efficiencies increase much faster than the measurement results. This effect is caused by the caught-on-first-touch (coft) model applied in the uni-directional coupled simulation. All particles

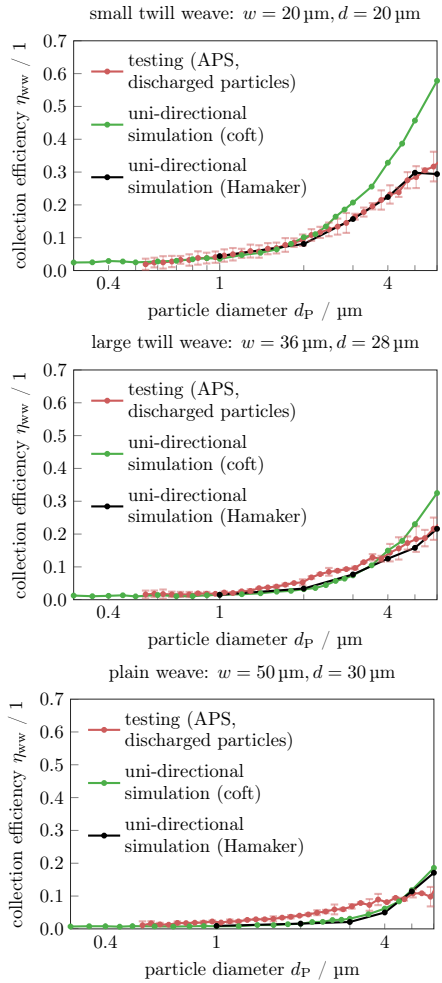

Figure 6.16: Comparison of the APS based testing results with simulated collection efficiencies for discharged particles. The uni-directional coupling approach implemented in the software package GeoDict is used to simulate the particle collection applying the caught-on-first-touch (coft) model (green) as well as the Hamaker model (black) for particle adhesion. The adhesion constant $H = 5 \cdot 10^{-20}$ J and restitution coefficient $R = 0.6$ are determined by fitting to the measured values.

which come into contact with a fiber surface invariably adhere to the filter medium.

In reality, however, particles with high velocities bounce off the filter medium as described in Sec. 2.1.1. Warth and Piesche [106] have already investigated this rebound behavior by means of metallic filters. According to Eq. (2.1), large particles rebound more likely. The adhesion constant H and the restitution coefficient R are the only unknown parameters of the equation. Via these two parameters, the simulated filtration efficiency can be fitted to the measurement results using the Hamaker model implemented in the software package GeoDict. For this purpose, the adhesion constants $H = \{1 \cdot 10^{-20},\ 5 \cdot 10^{-20},\ 1 \cdot 10^{-19}\}$ J are analyzed in combination with restitution parameters $R \in [0, 1]$. The results obtained for the best fitting parameter combination, i.e., $H = 5 \cdot 10^{-20}$ J and $R = 0.6$, are additionally plotted in Fig. 6.16. Especially for the two twill weaves, the curve of the APS based collection efficiencies can be reproduced very well. For the very low collection efficiencies of the plain weave, however, there is hardly any difference noticed compared to the original, caught-on-first-touch simulation.

6.4.2 Influence of Electrostatically Charged Particles

The influence of electrostatic particle charges (in combination with neutral filter media) is composed of two factors: the agglomeration of dust particles in the inflow area and mirror charge effects in the vicinity of fibers. The results from Chapter 5 have already revealed that electrostatic agglomeration does not play a role in the measurement results. For the comparison of the measurement results of untreated (charged) particles with the simulation, the modeling of mirror charge effects is particularly decisive. However, these were not the focus of this work and have not been implemented so far. Hence, Fig. 6.17 compares the measurement results using untreated (charged) particles with the simulation results in which no electrostatic interactions are taken into account. The difference between APS based experiments and the simulation results thus corresponds to the influence of the mirror charges.

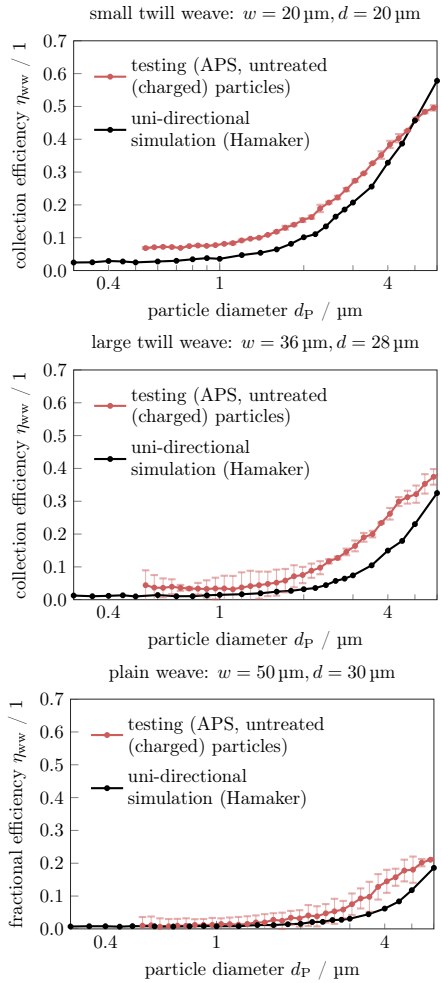

Figure 6.17: Comparison of the experimental measurement results for untreated (charged) particles with the simulation results obtained by using the Hamaker model of the uni-directional coupling method implemented in the software package GeoDict. The experimental measurement data consist of the results achieved with the optical particle counter and the aerodynamic particle sizer. All investigated wired weaves are grounded in the test facility.

6.5 Summary

Wired weaves are used to narrow the gap between experimental testing and simulation of filtration processes. Their simple structure and conductive material allow performing a specific analysis of different collection mechanisms. Basic preliminary experimental investigations revealed large differences in the measured fractional collection efficiencies when the particle sensors are placed in different positions. Significantly higher efficiencies are measured when the corresponding particle size distributions are determined upstream & downstream the filter medium compared to a downstream-only particle sampling. When an identical experimental setup is used, the results obtained with both examined particle measurement techniques, i.e., optical and aerodynamic, differ less. However, the measurements based on optical particle diameters strongly scattered during the analysis of irregularly shaped ISO fine dust particles. Discharging the dust particles at the inlet to the test channel leads to a reduction of the collection efficiencies with both measuring techniques. This is likely due to mirror charge effects which improve the separation of electrostatically charged particles.

A comparison of simulated collection efficiencies leads to good agreement with the APS based measurements. Exact spheres modeled in the simulation approaches are better comparable with aerodynamic than with optical particle diameters. Taking into account the Hamaker model for particle adhesion on fiber surfaces, a perfect match is achieved for discharged particles. At this point, the efficient uni-directionally coupled and the complex fully-coupled simulation approaches do not produce any differences. As soon as electrostatically charged particles are simulated with the four-way coupled method, extreme particle-particle interactions occur leading to instantaneous agglomeration. To simulate the behavior of charged particles, the four-way coupling between particles and the background flow field is therefore necessary. However, the electrostatic agglomeration takes place so rapidly that the effects are not taken into account in the experimental testings. In order to obtain better agreement with experimental measurements of untreated (charged) particles, the implementation of mirror charge effects is required.

The results of the combined experimental and numerical analysis of wired weaves provide a major contribution to further understanding of electrostatic filtration effects, but still leave some open issues. The transferability of the results obtained

using the grounded, conductive wired weaves to commonly applied, insulating cabin air filter media is investigated in the following chapter.

Chapter 7

Numerical & Experimental Analysis of Cabin Air Filter Media

The analysis based on simplified filter structures presented so far served to precisely examine individual separation mechanisms. With the single fiber model in Chapter 4, a strong influence of unipolar and bipolar fiber charge distributions has been pointed out in the simulations. Furthermore, the analysis of electrostatically induced particle dynamics in Chapter 5 revealed a rapid agglomeration process, which is, however, completed when the particles reach the filter medium. The use of wired weaves in Chapter 6 led to the assumption of a strong influence of mirror charge effects on the filtration efficiency. When looking at real cabin air filter media by contrast, all the above mentioned filtration effects occur simultaneously and interfere with each other. This way, the degree of complexity in the particle separation behavior significantly increases.

This chapter aims to uncover differences between the numerical and the experimental filtration analysis with regard to the big picture. In order to bring the respective filtration performance data closer together, a mutual approach is necessary. For this purpose, obvious setup differences between the experimental testing procedure and the status quo simulation approach are specifically examined. These obvious differences include the shape of aerosol particles and the unknown electrostatic charging states of filter fibers and dust particles. The influence of

these parameters is investigated by means of two distinct cabin air filter media, which are introduced in Sec. 7.1. In the experimental part in Sec. 7.2, diverse test aerosols are used to realize differently shaped particles. Furthermore, different electrostatic charging states of filter fibers and particles are analyzed in all possible combinations. The aim of these measurements is to determine the importance of individual electrostatic separation mechanisms for the overall filtration efficiency.

In the simulation studies in Sec. 7.3, the uni-directionally coupled approach implemented in the software package GeoDict is applied to simulate the filtration performance. This status quo approach enables the simulation of real, complex cabin air filter media. Since the approach only provides the simulation of ideally spherical particles, the comparison with the behavior of liquid droplets is of particular interest. In experiments, these liquid droplets offer the advantage of being spherical by nature. Another focus of the simulation studies is on different electrostatic charge conditions. Based on a comparison with the experimental results and on the findings gained so far in this thesis, requirements for future simulations are derived. The effects that need to be implemented in order to simulate the complex physical processes involved in cabin air filtration in a predictive way are identified.

7.1 Specification of Cabin Air Filter Media

Two fundamentally different cabin air filter media serve as a basis for the experimental and numerical analysis of filtration processes in this chapter. Figure 7.1 shows the digitized structures of both cabin air filter media. These digital twins of real filter media are derived from xCT-images of small samples. The same cross-sectional area of $(1024 \times 1024)\,\mu m^2$ is chosen for both filter models.

Both cabin air filter media consist of polypropylene, but differ in their manufacturing process and, thus, in their microstructure. The spunbond filter medium on the left-hand side is produced by the manufacturer Reifenhäuser Reicofil [81]. It is characterized by its very open structure with large and uniform fiber diameters $d_F \approx 35\,\mu m$. Furthermore, the filter medium thickness is relatively small with scarcely $900\,\mu m$. Due to its simple design, this spunbond nonwoven is ideally suited for basic research studies.

(a) open-pored spunbond medium (b) dense meltblown medium

Figure 7.1: Digital twins derived from xCT-images of samples from the two different cabin air filter media analyzed in this work. Both samples have a cross sectional area of $(1024 \times 1024)\,\mu m^2$. The height of each filter medium is shown completely. The open-pored spunbond medium (a) is produced by the manufacturer Reifenhäuser Reicofil [81]. The dense meltblown medium (b) is produced by the Sandler AG [87].

The meltblown medium on the right-hand side is produced by the manufacturer Sandler AG [87]. This filter medium has a thickness of approximately 1150 µm and a fiber size distribution with diameters between $d_F = 4\,\mu m$ and $d_F = 20\,\mu m$. Hence, the meltblown filter medium is denser and much more complex compared to the spunbond medium. The SEM images in Fig. 7.2 also demonstrate the different fiber compositions. Note that, different scales are applied for the two cabin air filter media.

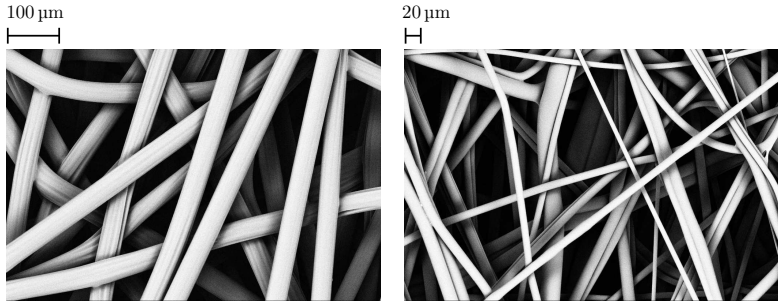

(a) open-pored spunbond medium (b) dense meltblown medium

Figure 7.2: SEM images of the two cabin air filter media presented in Fig. 7.1 from the point of view of the incoming particulate flow. The open-pored spunbond medium (a) is produced by the manufacturer Reifenhäuser Reicofil [81]. The dense meltblown medium (b) is produced by the manufacturer Sandler AG [87]. Note that different scales are applied for both SEM images.

7.2 Experimental Analysis

The experimental analysis in this chapter comprises the determination of the initial separation efficiency for both cabin air filter media presented above. The measurements comply with a standard test for cabin filter media according to DIN 71 460-1 [27]. However, individual parameters are varied in this work in order to characterize specific influencing factors. The use of different test aerosols aims at demonstrating the influence of the particle shape on the deposition behavior. For instance, oily droplets are used to imitate spherical particles as they are modeled in simulation. Besides the particle shape, the aerosols differ in further properties such as the electrostatic charge conditions or their aggregate state. Thus, measured effects can not directly be assigned to specific single particle properties, and challenges arise when interpreting the results. For this reason, the influence of electrostatic particle charging states as well as fiber charging states on the filtration behavior is investigated specifically in a second experimental study. The experimental setups as well as details about the different testing conditions are presented below.

7.2.1 Experimental Testing Setup

Two different test facilities are employed for the experimental measurements of cabin air filter media. Besides the MFP 3000 test rig already used in Chapter 5 and Chapter 6, the test rig PAF (PArticulate Filtration) 111 from Topas GmbH is used. Both test facilities represent well-established modular test systems for cabin air filter media. The main difference is the investigated filter medium area. While the MFP 3000 uses a round blank with a filter medium area of $A_{\mathrm{MFP}} = 100\,\mathrm{cm}^2$, the PAF 111 loads a rectangular area of $A_{\mathrm{PAF}} = (18.5 \times 57)\,\mathrm{cm}^2 = 1054.5\,\mathrm{cm}^2$ with the test aerosol.

In this work, the PAF 111 is used for the analysis of different test aerosols and the MFP 3000 for investigating the influence of different electrostatic charging conditions. Calculating the collection efficiency is carried out conventionally for both test rigs according to Eq. (2.3). When determining the collection efficiency η_{CAF} of cabin air filter media, $N_{\mathrm{inlet}}(d_{\mathrm{P}})$ and $N_{\mathrm{outlet}}(d_{\mathrm{P}})$ correspond to the number of particles of the size class d_{P} in raw and clean gas. For both test facilities, the 'upstream & downstream setup' described in Sec. 5.3.1 is used to measure the particle size distributions. In this setup, the particle sensors are located upstream (raw gas) and downstream (clean gas) the filter medium.

Test Aerosols. Three different test aerosols are used to determine the fractional separation efficiency η_{CAF} for both filter media: ISO fine dust, sodium chloride and DEHS particles. Among other properties, they differ in their particle size distribution, their particle shape and their aggregate state. All three are common test aerosols for measuring the performance of cabin air filter media and are already briefly introduced in Sec. 2.2.2. The requirement for a test aerosol is the stable and reproducible generation of a constant particle size distribution and particle concentration.

> **ISO fine dust** is the standard aerosol in this thesis as already mentioned in Sec. 2.2.2. The experimental analyses in Chapter 5 and Chapter 6 are also based on ISO fine dust. In contrast to modeled particles in simulation studies, however, ISO fine dust particles are strongly non-spherical. As stated in Sec. 5.1.1.3, the dust particles generated by an RBG 1000 disperser, moreover, carry very high electrostatic charges. These electrostatic charges are also

supposed to affect the filtration efficiency of real cabin air filter media in this section. The measurement of the number of ISO fine dust particles in the raw gas $N_{\mathrm{clean}}(d_{\mathrm{P}})$ and clean gas $N_{\mathrm{raw}}(d_{\mathrm{P}})$ is carried out using the optical particle counter (OPC) described in Sec. 2.2.4.

Sodium chloride (NaCl) represents a further solid material that is examined in the context of diverse aerosols. Compared to ISO fine dust particles, which are dispersed from a powder, NaCl particles are generated by atomizing a saline suspension. In this work, the aerosol generator AGK 2000 from Palas GmbH is applied to atomize a ten percent saline solution. The functional principle of the AGK 2000 is based on a two-substance nozzle [75]. Since the generated NaCl particles are smaller than ISO fine dust, a scanning mobility particle sizer (SMPS) measuring device is applied to determine the particle size distributions in this case. The underlying measuring principle is explained in Sec. 2.2.4.

Di-Ethyl-Hexyl-Sabacat (DEHS) represents a material for stable liquid aerosol particles. The Six-Jet Atomizer 9306 from TSI Incorporated is applied to atomize the DEHS fluid in this work. The resulting droplets provide the advantage of being inherently spherical. In addition, the oily droplets prevent the formation of dendrites through separated particles and, thus, a change of the particle deposition over the measuring time. The SMPS measuring device is used again for sizing DEHS particles.

The test conditions for measuring the filtration efficiencies with the different aerosols are summarized in Tab. 7.1. In addition to the collection efficiency, the measured particle size distributions of the raw gas are analyzed in Sec. 7.2.2.

Electrostatic Charging States. The influence of different electrostatic charging conditions on the filtration efficiency is investigated using the spunbond filter medium, only. The analysis includes both, the charging state of the filter medium and the ISO fine dust particles. Analogous to previous measurements in Sec. 5.3.2 and Sec. 6.2.2, dust particles are discharged using a corona discharge unit. The filter medium is discharged by immersion in isopropyl alcohol.

Parameter		Value
Face velocity	v	$0.2\,\mathrm{m/s}$
Volume flow rate	$\dot{V}$	$76\,\mathrm{m^3/h}$
ISO fine dust concentration	c_{ISO}	$3.5 \cdot 10^{-5}\,\mathrm{kg/m^3}$
NaCl salinity	s_{NaCl}	$10\,\%$
DEHS concentration	c_{DEHS}	$1 \cdot 10^{-4}\,\mathrm{kg/m^3}$

Table 7.1: Common test conditions used for measuring the filtration efficiencies of the two cabin air filter media presented in Fig. 7.1. The face velocity v and the volume flow rate $\dot{V}$ correspond to the flow conditions at the height of the filter media.

The following four combinations are used in order to quantify the contribution of different separation mechanisms to the overall filtration efficiency:

Charged filter medium & untreated (charged) particles represent the original system with regard to cabin air filter tests.

Charged filter medium & discharged particles allow analyzing the separated influence of fiber charges.

Discharged filter medium & untreated (charged) particles allow focusing on the influence of electrostatically charged particles.

Discharged filter medium & discharged particles omit all electrostatic separation mechanisms and provide the analysis of pure mechanical particle collection.

When evaluating the measurement results, it must be kept in mind that a complete discharge of the materials is not ensured. A small residual charge may remain on both, the filter medium and the dust particles. An optical particle counter is applied for all measurements as ISO fine dust particles are used. Further test conditions used for the investigation of the electrostatic charging states are listed in Tab. 7.2.

Parameter		Value
Face velocity	v	$0.2\,\mathrm{m/s}$
Volume flow rate	$\dot{V}$	$120\,\mathrm{l/min}$
ISO fine dust concentration	c_{ISO}	$7.5 \cdot 10^{-5}\,\mathrm{kg/m^3}$

Table 7.2: Common test conditions used for measuring the filtration efficiency of the spunbond filter medium presented on the left-hand side of Fig. 7.1 for different electrostatic charging states. The face velocity v and the volume flow rate $\dot{V}$ correspond to the flow conditions at the height of the filter media.

7.2.2 Experimental Testing Results

Analogous to the presentation of the experimental testing setups, the measurement results for different test aerosols are discussed first. The influence of the electrostatic charging state on the filtration efficiency is subsequently analyzed.

Influence of the Test Aerosol. Before the separation efficiency with different test aerosols is evaluated, the measured particle size distributions in the raw gas are compared with each other. Figure 7.3 shows the probability density function q_0 measured for NaCl, DEHS and ISO fine dust particles under the given test conditions. According to the respective particle sizes of the aerosols, an SMPS (left) or an OPC (right) is used to determine the particle diameters. The mean value from ten measurement series and the associated standard deviation are plotted in each case.

The three test aerosols cover different particle size ranges. While the ISO fine dust particles are relatively coarse with many particles being larger than $d_{\mathrm{P}} = 1\,\mu\mathrm{m}$, all NaCl and DEHS particles are in the submicron size range. Hence, NaCl and DEHS have a very small modal value at a particle diameter of $d_{\mathrm{P}} = 0.11\,\mu\mathrm{m}$ and $d_{\mathrm{P}} = 0.17\,\mu\mathrm{m}$, respectively. The most frequent particle size of ISO fine dust particles is $d_{\mathrm{P}} = 0.31\,\mu\mathrm{m}$. Since a minimum filter load is ensured, submicron particles are particularly well suited for the measurement of initial filtration efficiencies. Furthermore, the probability density function for DEHS particles exhibits very low scatters. This demonstrates that the generation of DEHS droplets is particularly uniform and stable.

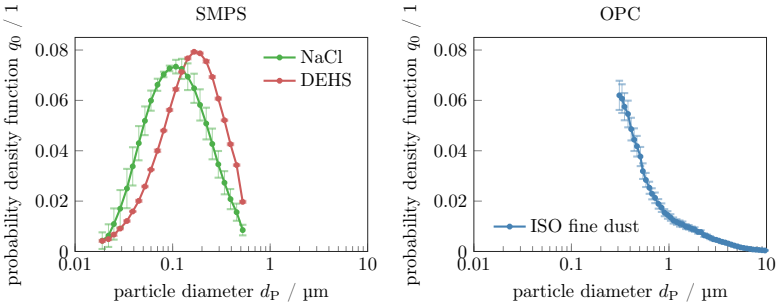

Figure 7.3: Experimentally determined probability density function q_0 for three different filter test aerosols. Besides the already familiar ISO fine dust, NaCl and DEHS particles are used in this work. Depending on the particle size spectrum, an SMPS (left) or OPC (right) measuring device (see Sec. 2.2.4 for details) is used to determine the particle diameters.

The result of exposing the two cabin air filter media presented in Fig. 7.1 to the three different aerosols is shown in Fig. 7.4. Depending on the respective particle diameter, the fractional collection efficiency η_{CAF} is based on measurements with an optical particle counter (OPC) or a scanning mobility particle sizer (SMPS) accordingly. Since the measuring devices are restricted to the specific size ranges, the efficiencies are plotted only for the particles in these size ranges. The mean value and the associated standard deviation of five measurement series are plotted in each case.

The measurement results reveal an enormous influence of the applied test aerosols on the resulting collection efficiency η_{CAF}. In principle, the same characteristics are observed for both cabin air filter media: very high collection efficiencies for ISO fine dust particles, a medium efficiency for NaCl particles and a very low collection of DEHS particles. However, all three collection efficiencies for the more complex meltblown filter medium are shifted towards a higher degree of particle deposition. Separation efficiencies of more than $\eta_{CAF} = 96\,\%$ are measured over the complete ISO fine dust particle range. In the case of the open-pored spunbond medium, the minimal collection efficiency is still $\eta_{CAF} = 78\,\%$. These high

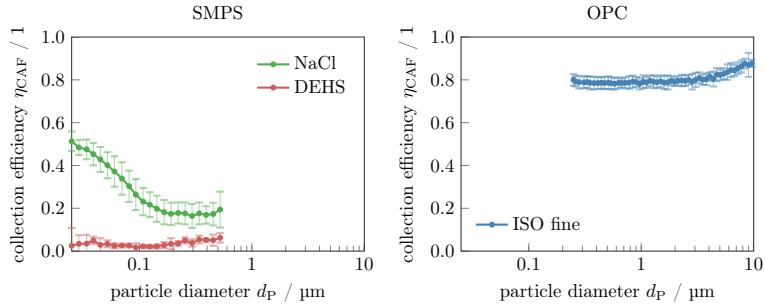

(a) spunbond filter medium

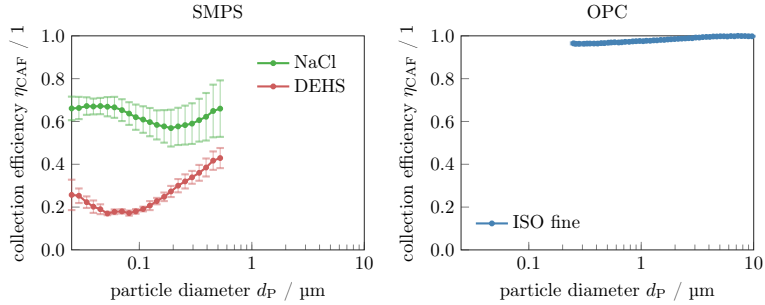

(b) meltblown filter medium

Figure 7.4: Experimentally determined fractional collection efficiencies η_{CAF} for the two cabin air filter media presented in Fig. 7.1: (a) spunbond filter medium and (b) meltblown filter medium. Besides the already familiar ISO fine dust, NaCl and DEHS were used as test aerosols. Depending on the particle size spectrum, an SMPS (left) or OPC (right) measuring device is used to determine the particle diameters.

separation efficiencies are achieved due to the strong electrostatic fiber-particle interactions of the dust particles dispersed by the RGB 1000. The separation of atomized NaCl particles is significantly less pronounced. In this case, a clearer dependence of the filtration efficiency on the particle diameter is observed. This curve for NaCl particles indicates that mechanical collection mechanisms play a more important role than for the highly charged ISO fine dust particles. Thus,

the so-called most penetrating particle size (MPPS) introduced in Sec. 2.1.1 is observable for both cabin air filter media. The MPPS is in the range of $d_P = 0.3\,\mu m$ to $0.4\,\mu m$ for the open-pored spunbond medium and shifts towards smaller particle diameters of $d_P = 0.2\,\mu m$ for the dense meltblown medium. Smaller particles than the MPPS have a high probability of colliding with filter fibers due to Brownian motion. Larger particles than the MPPS are separated due to interception and inertia. An increase in the separation efficiency can be clearly seen for the meltblown medium. For the spunbond medium, an increase for larger particles is also assumed by extrapolating the measured efficiency. However, larger NaCl particles than $d_P = 0.4\,\mu m$ rarely occur and are not detected with the applied SMPS.

The separation of liquid DEHS particles is in turn significantly lower than of NaCl particles for both investigated cabin air filter media. For the open-pored spunbond medium, the maximal separation efficiency is just $\eta_{CAF} = 6.2\,\%$. With the dense meltblown filter medium, by contrast, separation efficiencies of more than $\eta_{CAF} = 17\,\%$ are achieved, and the characteristic curve containing an MPPS is also pronounced. Compared to the deposition of NaCl particles, the MPPS further shifts in the direction of smaller particles with $d_P = 0.06\,\mu m$ to $0.07\,\mu m$.

The main reason for the significant difference in the separation of NaCl and DEHS particles is most probably the electrostatic fiber-particle interaction. In literature, NaCl particles are considered to have a low particle charge intensity between $n_e = -2\,e$ and $n_e = 2\,e$ [51], whereas the liquid DEHS particles are regarded as electrostatically neutral. The particle shape is assumed to have only a minor influence on this analysis. In order to better understand the influence of electrostatic effects, different charging states are examined below.

Influence of the Electrostatic Charging State. As mentioned in Sec. 7.2.1, four different combinations of charged/discharged filter media and untreated (charged)/discharged dust particles are examined. Figure 7.5 shows the corresponding measured separation efficiencies η_{CAF} for the spunbond filter medium exposed to ISO fine dust. Again, the mean value of five measurement series and the associated standard deviation are plotted in each case.

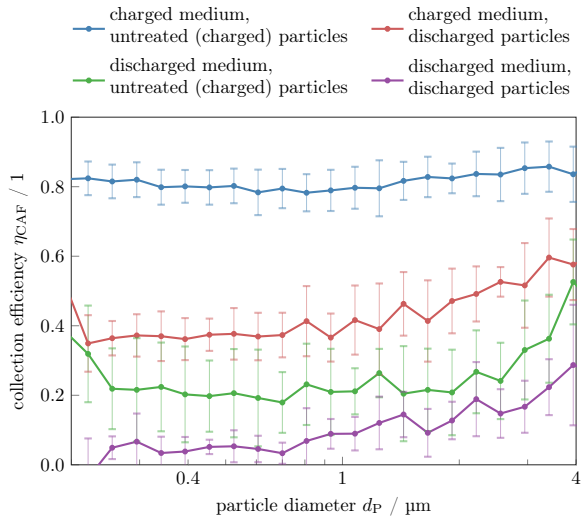

Figure 7.5: Experimentally determined fractional collection efficiencies η_{CAF} for the spunbond cabin air filter media presented on the left-hand side of Fig. 7.1. Different combinations of charged/discharged filter medium with untreated (charged)/discharged ISO fine dust particles are analyzed. Discharging the filter medium is carried out with vaporized isopropyl alcohol. The dust particles are discharged using the corona-discharge unit introduced in Sec. 2.2.1.

It is obvious that the charging state of the examined system is decisive for the resulting filtration efficiency. Depending on the electrostatic charge of the filter medium and the dust particles, the separation efficiency varies between $\eta_{CAF} = 9\,\%$ and $\eta_{CAF} = 80\,\%$ for a particle with $d_P = 1.1\,\mu m$. In all four curves, different separation mechanisms are effective causing these high variations. For a completely discharged system of filter medium and dust particles (violet), only mechanical collection mechanisms are effective. In the case of the examined open-pored spunbond medium, these purely mechanical collection effects are not very significant leading to low efficiencies. However, an increase in the separation efficiency for particles with $d_P > 1\,\mu m$ due to inertial effects is still evident.

If using untreated (charged) particles in the next step, while the filter medium remains discharged, a parallel shift of the separation efficiency occurs. Averaging over all particle size classes, the separation efficiency increases by 17 %. Mirror charges, which are generated on the surface of the insulating fiber material by charged particles, are assumed to be responsible for the improved separation. Since electrostatic particle-particle interactions in the test channel area of interest have already been excluded in Sec. 5.1, mirror charges are the only electrostatic effects occurring. Mechanical collection mechanisms are naturally still effective.

In the contrary case with a charged filter medium, but discharged dust particles, the mechanical collection mechanisms are supplemented by induced dipole effects. As explained in Sec. 2.1.1, the induced dipoles are formed in the particles in contrast to the mirror charges that refer to the filter medium. Compared to the purely mechanical collection of particles, the filtration efficiency is improved by an average of 32 percentage over all particle diameters. This fact leads to the conclusion that induced dipoles have almost twice the impact on the separation efficiency of the investigated spunbond medium as mirror charges.

The original combination of a charged cabin air filter medium with untreated (charged) particles leads to the full exploitation of all filtration mechanisms, i.e., mechanical and all electrostatic separation mechanisms. In addition to the already quantified impact of induced dipoles and mirror charge effects, strong Coulomb interactions between charged fibers and charged particles appear. Since all electrostatic effects interfere, no clear distinction can be made between individual separation mechanisms in this case. In order to simulate the complex electrostatic fiber-particle interactions, all three effects, i.e., induced dipoles, mirror charges and Coulomb attraction, must be modeled and validated individually. The following analysis reveals the possibilities and challenges of the status quo simulation approach.

7.3 Uni-Directional Simulation of Cabin Air Filter Media

Predictive simulations of the particle movement through real complex cabin air filter media require a high computational effort. Based on the findings on rapid electrostatic particle agglomeration from Sec. 5.1, the uni-directionally coupled simulation approach is sufficient if taking into account the respectively modified particle size and charge distribution after agglomeration. This simplification allows simulating the filtration performance of a representative volume element in a feasible runtime. In order to predict the dust holding capacity and the increasing pressure drop with dust loading, the simulation of correct fractional efficiencies must be ensured for each batch of added particles. Therefore, the initial fractional efficiencies, i.e., particle deposition in a new, clean filter medium must be determined in a first step. Taking into account all mechanical and electrostatic separation mechanisms involved in air filtration, the simulation of this fractional efficiency still poses a major challenge. The objective of the simulation studies in this section is to present the existing possibilities of the uni-directionally coupled status quo approach including the enhancements introduced in this work. In addition, further effects that have to be implemented for the precise simulation of cabin air filter media are to be pointed out. As in previous investigations in this thesis, the focus primarily is on electrostatic separation mechanisms.

7.3.1 Simulation Experiment Setup

As mentioned above, the status quo of the uni-directionally coupled approach implemented in the software GeoDict is applied to simulate the performance of cabin air filter media. The procedure and the underlying models have already been introduced comprehensively in Sec. 2.3. This procedure is applied to the xCT-based models of cabin air filter media presented in Fig. 7.1. Figure 7.6 shows the cross section of the basic simulation setup exemplary for the spunbond medium.

In a preparatory step, the fluid flow through the filter medium is calculated using the Navier-Stokes LIR solver described in Sec. 2.3.4. Besides the size of the simulation domain, Fig. 7.6 also shows the applied boundary conditions. Dirichlet boundary conditions with the face velocity $v_{\mathrm{in}} = 0.2\,\mathrm{m/s}$, equal to those applied

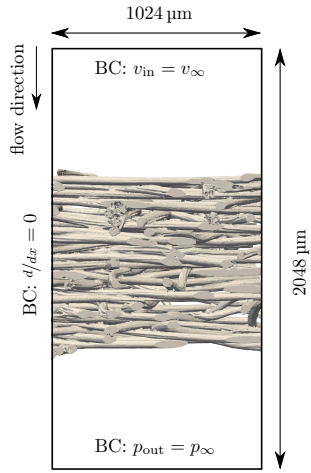

Figure 7.6: Two-dimensional representation of the simulation experiment setup used for the analysis of the two cabin air filter media presented in Fig. 7.1. The spunbond medium is exemplarily illustrated. In addition to the domain size, the applied boundary conditions are given.

in the laboratory experiments, are used at the domain inlet to initialize the air flow. At the outlet, Neumann boundary conditions with the ambient air pressure $p_{out} = 1013\,\text{mbar}$ are used. The simulation domain is periodic perpendicular to the direction of flow. After calculating the air flow field, particles are added to the inflow area. In order to cover a multitude of starting positions, 10.000 particles of each discrete particle size class are added. This high number ensures a smooth curve for the simulated fractional separation efficiency. Based on the previously calculated flow field, the particles are tracked and collisions with the filter medium are monitored.

To begin with, an electrostatically neutral system of filter medium and dust particles is simulated. Subsequently, the charge conditions are modified in order to take the Coulomb attraction between fibers and particles into account.

7.3.2 Numerical Results & Comparison with Experiments

Similar to the experimental results in Sec. 7.2.2, the simulation results for cabin air filter media are divided into two paragraphs: Firstly, the simulated filtration efficiency is compared to measurement results for different test aerosols. Since an electrostatically neutral system is analyzed in the simulation study, the highly charged ISO fine dust particles are omitted in this comparison. Secondly, the focus is on the influence of electrostatic charges on the simulated separation efficiencies. At this point, the results for the ISO fine dust particles are used for a comparison with measurements.

Influence of the Test Aerosol. The separation of electrostatically neutral particles by likewise neutral filter fibers represents the simplest case in the simulation studies. Figure 7.7 shows the simulation results for the purely mechanical filtration process. The simulated fractional separation efficiencies for both examined cabin air filter media are compared with the measurement results from Fig. 7.4. As mentioned above, only the results obtained by the SMPS measurement device, i.e., NaCl and DEHS measurements, are included in this comparison. Since ideally spherical particles are modeled, the material density is the only different parameter for the simulation of NaCl ($\rho_{\mathrm{NaCl}} = 2160\,\mathrm{kg/m^3}$) and DEHS ($\rho_{\mathrm{DEHS}} = 900\,\mathrm{kg/m^3}$) particles. However, the simulated efficiencies show no visible differences and, thus, only one curve for simulated efficiencies is displayed for each filter medium.

A good agreement between the simulation results and the experimentally determined separation efficiency for DEHS particles is observed for the spunbond filter medium. For the more complex meltblown filter medium, the simulated degree of separation is also in the order of magnitude of the experimental deposition of DEHS. However, the shape of the curves differs significantly in this case. The measured separation efficiency for NaCl particles strongly deviates for both analyzed filter media. This deviation is mainly attributed to the additionally effective electrostatic separation mechanisms for NaCl particles. The small amount of electrostatic charges carried by NaCl particles, i.e., $n_e = -2\,e$ to $+2\,e$ [51], already contributes significantly to increasing the separation efficiency. In addition, the non-spherical shape of NaCl particles may contribute to the increase of particle

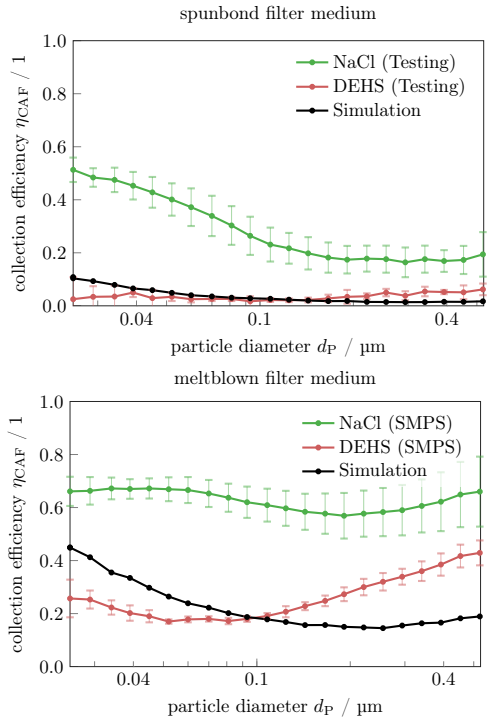

Figure 7.7: Comparison of the simulated fractional collection efficiency η_{CAF} with measurement results for NaCl and DEHS particles. The simulations are based on the xCT-models of the two cabin air filter media presented in Fig. 7.1. An electrostatically neutral system of filter medium and particles is used for the uni-directionally coupled simulation implemented in the software package GeoDict.

deposition. However, since the particle shape is supposed to mainly affect the interception mechanism, it is assumed that the influence is of minor importance for the small particle sizes.

Influence of the Electrostatic Charging State. As seen in Fig. 7.5, different charging states of the filter medium and of naturally highly bipolar charged ISO fine dust particles strongly affect the separation efficiency. For the comparison of the simulation results obtained by the uni-directionally coupled approach with the ISO fine dust measurements, a completely neutral system is initially considered again, i.e., discharged filter medium and discharged dust particles. Figure 7.8 demonstrates a good agreement of the status quo simulation approach for this case.

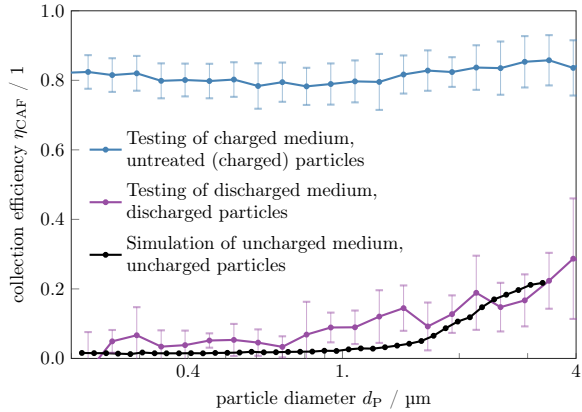

Figure 7.8: Comparison of the simulated collection efficiency η_{CAF} with experimental measurement results of a discharged system of filter medium and dust particles as well as the original state. The uni-directional coupling approach implemented in the software package GeoDict is applied for the simulation. The model of the open-pored spunbond medium presented in Fig. 7.1 is used as digital filter structure.

However, the objective is to simulate the original state of a charged filter medium loaded with untreated (charged) particles which is additionally plotted in blue. The uni-directionally coupled simulation tool allows including the electrostatic separation by Coulomb attraction between charged fibers and charged particles. Four unipolar particle charge distributions plotted in Fig. 7.9 are used in the subsequent numerical experiments.

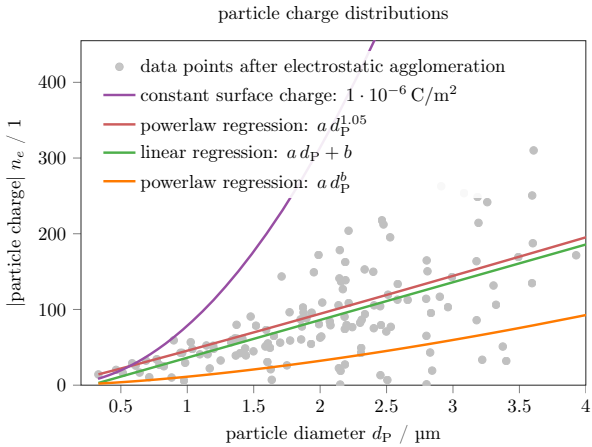

Figure 7.9: Four different particle charge distributions serve as input functions for the uni-directionally coupled simulation of cabin air filter media. Both power laws and the linear regression are based on the data points (gray dots) resulting from the fully-coupled simulation of electrostatic agglomeration in Sec. 5.1. A constant surface charge density $\xi_\mathrm{P} = 1 \cdot 10^{-6}\,\mathrm{C/m^2}$ represents an independent, simple quadratic function.

The first charge distribution (violet) assigns a constant surface charge to all particle sizes. The respective quadratic function of the particle diameter is the only one of the four distributions that is not derived from the simulation results of electrostatic agglomeration obtained in Sec. 5.1. The gray data points represent the average charge intensity for each particle size present after the agglomeration process. The data points are derived from nine simulation runs with the input particle size distribution and charge distributions plotted in Fig. 5.6 and Fig. 5.7. Applying these parameter sets yielded a unipolar negative charge distribution after agglomeration. Different regression types are applied to generate three further particle charge distributions: a linear regression with slope a and intercept b as fitting parameters, a power law regression fitting slope a and exponent b, and a power law regression with a fixed exponent $b = 1.05$. The latter is based on Forsyth's semi-empirical Eq. (5.1), which served as the input function for particle sampling for the agglomeration simulation.

In order to simulate the filtration efficiency taking Coulomb interactions into account, the cabin air filter medium must be assigned an electrostatic charge, too. This charge is simplistically assumed to be homogeneous on the entire surface of all filter fibers and has the opposite polarity to the one of the particles. Figure 7.10 shows the wide range of simulated collection efficiencies obtained with the given charge configurations. The target collection efficiency η_{CAF} of the experimental measurement using the original system of charged filter medium and untreated (charged) particles is additionally displayed. In order to fit the measured separation efficiency, the intensity of the fiber charge is varied in the simulation study.

It is obvious that both, the order of magnitude and the shape of the simulated collection efficiency curves, differ significantly for the four distinct particle charge distributions. The results indicate that a reproduction of the experimental results are possible when the particle charge distribution and the fiber charge intensity are chosen accordingly. However, many other parameters potentially also play a role in the measurements and ought to be taken into account when fitting the simulation results. As seen in the analysis by means of the single fiber model in Sec. 4.2, the charge distribution on the filter fibers has a considerable influence in addition to the charge intensity. For instance, a bipolar fiber charge distribution changes the curve of the simulated separation efficiency significantly. Besides the electrostatic parameters regarding particles and filter medium, the testing conditions and the characteristic structure of the filter medium may be relevant. Amongst others, relevant testing conditions include, e.g, the face velocity, the dust concentration and the relative humidity. With regard to the microstructure of the cabin air filter medium, the filter thickness, the fiber diameter and pore size distribution or the packing density are of particular interest. This enumeration already results in ten degrees of freedom for a parameter fitting. The existing database is much too small to solve this high-dimensional problem. Even if one accepts this challenge, the correct representation of underlying physical processes is not given in case of pure parameter fitting of the existing simulation setup. Therefore, a consecutive implementation of all three electrostatic separation effects, i.e., induced dipoles, mirror charges and Coulomb interaction, is proposed. Induced dipoles and mirror charges are supposed to be independent of each other and can be

validated separately using the experimental results plotted in Fig. 7.5. Afterwards, the already integrated Coulomb attraction can be added. With this procedure, the interference of all separation mechanisms is considered. The proper simulation of the physical effects then also ensures transferability to other cabin air filter media.

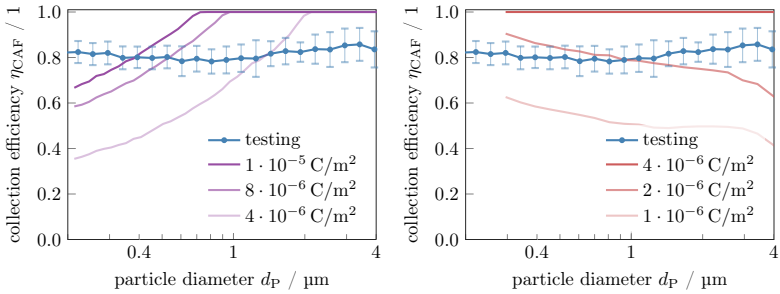

(a) constant surface charge: $1 \cdot 10^{-6}\,\mathrm{C/m^2}$

(b) powerlaw regression: $a\,d_P^{1.05}$

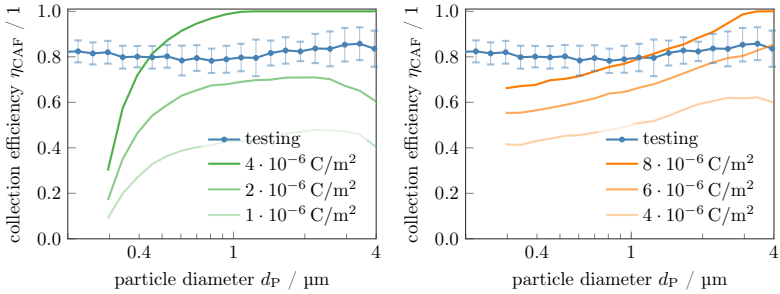

(c) linear regression: $a\,d_P + b$

(d) powerlaw regression: $a\,d_P^b$

Figure 7.10: Comparison of the simulated fractional collection efficiency η_{CAF} with the measurement results of the charged spunbond medium and untreated (charged) ISO fine dust particles. The uni-directionally coupled simulation runs are based on the four particle charge distributions presented in Fig. 7.9. The entire surface of the filter fibers is assumed to be uniformly charged with opposite polarity compared to the particle's polarity. The intensity of this surface charge is varied in each case in order to approximate the experimental results.

7.4 Summary

The overall picture of cabin air filtration comprises more than the composition of the individual separation effects analyzed in previous chapters. Since several mechanical and electrostatic separation effects act simultaneously and even interfere with each other, simulating the particulate flow through cabin air filter media still poses major challenges. In this chapter, two filter media with different degrees of complexity were used to analyze the filtration process by experiments as well as simulation studies. Exposing the cabin air filter media to three different test aerosols with differently shaped particles and with different electrostatic charge intensities revealed three entirely different separation efficiency curves. The liquid, presumed to be perfectly spherical DEHS particles led to a very low deposition particularly for the open-pored spunbond medium. As the comparison with the simulation of an electrostatically neutral system proved, these particles are purely filtered by mechanical collection mechanisms in this case. In contrast, the experimentally determined separation efficiency of NaCl particles was significantly higher. This effect was attributed to the fact that NaCl particles carry a small amount of electrostatic charges. The extremely efficient separation of ISO fine dust particles results from their high electrostatic charge intensity. Separately discharging individual components (filter fibers and dust particles) enabled the quantification of the contribution of specific electrostatic effects. Induced dipoles in neutral particles are assumed to be the reason for an improvement of the separation efficiency by an average of 32 % for all particle sizes under consideration. Mirror charge effects, which have already been reported in the context of wired weaves also seem to increase the separation efficiency by 17 % on average.

The simulation of real, complex cabin air filter media is enabled by the use of the uni-directionally coupled simulation. Based on digitized filter models, the particulate flow through both experimentally analyzed cabin air filter media was simulated. The combination of an electrostatically neutral filter medium with neutral ISO fine dust particles resulted in a good agreement with the corresponding experiments. Fitting the simulation results to the measurements for the original system of a charged filter medium and untreated (charged) dust particles is not promising. Too many degrees of freedom in combination with a too small database complicate this. Furthermore, the correct simulation of the underlying physical

principles can not be ensured by a parameter fitting. In order to simulate the behavior of highly charged ISO fine dust particles, the implementation of missing components is required. This includes the simulation of mirror charges and induced dipoles. Induced dipoles in dust particles can for instance be modeled via two superimposed particles with opposite polarities. By implementing the required physics, the transferability to further cabin air filter media can be provided. In order to further develop virtual filter media in the future, these adaptations to the simulation tool are required and should be validated in further simulation studies.

Chapter 8

Conclusions & Future Work

The overall objective of this thesis was to provide answers to the identified research question:

Which models for the microstructure simulation of fibrous structures are necessary to simulate cabin air filter media with regard to electrostatic charges?

In order to solve this overarching research issue, an enhanced fully-coupled modeling approach for the simulation of air filtration processes was devised. This novel modeling approach enables the numerical simulation of potentially effective fiber-particle and particle-particle interactions during the filtration process. The coupling of the required individual components, i.e., mechanical particle-particle and fiber-particle interactions, electrostatics and hydrodynamics, was modeled with the existing routines implemented in the software package ESPResSo. Enhancements primarily referred to the modeling of the specific interaction between ISO fine dust particles and their separation by filter fibers. Based on a single fiber model, this fundamentally new approach was thoroughly verified with respect to air filtration. Numerous simulation studies and supplementary experimental investigations were subsequently conducted to tackle the three aspects of the overall research issue.

How does electrostatic dust agglomeration caused by particle-particle interactions affect the filtration performance?

Fully exploiting the advantages of the novel modeling approach compared to the uni-directionally coupled status quo, particle-particle interactions between highly bipolar charged dust particles were simulated. The observed rapid electrostatic

agglomeration process leads to substantially modified particle size and charge distributions. Afterwards, all (agglomerated) particles are unipolar negatively charged. Since a stable equilibrium is reached within a few microseconds, however, the electrostatic agglomeration process is supposed to occur directly after particle dispersion in experimental investigations. Hence, the conclusion was drawn that particle-particle interactions do not play a major role in standard experiments, where the separation efficiency is derived from the ratio of the amount of particles in a specific size class in the upstream and downstream air flow. Due to the altered particle size and charge distributions, however, an indirect effect on the separation efficiency is expected.

To what extent does the accuracy of the simulated particle behavior depend on the coupling intensity between the individual components, i.e., electrostatically charged solid particles and the fluid flow field?

Further simulation studies were performed with a uni-directionally coupled modeling approach in order to analyze fluid-particle interactions in the complex test channel geometry. The simulation results revealed a strong recirculation at the inlet of the test channel leading to a good mixing of particles with different sizes. Supporting experimental analyses of particle dynamics in the empty test channel confirmed that both the electrostatic and the hydrodynamic effects occur before the upstream measurement point in standard experiments. Despite the intense particle dynamics in both simulation studies, a negligible 'artificial filtration' efficiency was measured in the empty test channel. Nevertheless, these preceding electrostatic and hydrodynamic effects must be taken into account in the simulation approach in order to properly model the further filtration process. Therefore, a two-step simulation procedure with different coupling intensities is proposed at this point: The first step involves the computationally complex fully-coupled simulation of the electrostatic agglomeration process. With highly charged particles, the high coupling intensity of the individual components has a significant effect on particle dynamics. Based on the resulting particle size and charge distribution, the movement of the (agglomerated) dust particles in the flow field can be calculated in a second step.

Which further electrostatic mechanisms need to be implemented in order to reliably predict the filtration performance of real cabin air filter media?

On the basis of real cabin air filter structures, further important electrostatic filtration effects were characterized addressing this third subordinate research question. Wired weaves served as simple filter substitutes and proved to be highly suitable for focusing on the individual electrostatic separation mechanisms by comparison between experiments and simulation. The conductive filter structures were grounded in the test facility and were thus electrostatically uncharged. However, experimental investigations with untreated (charged) dust particles showed significantly higher separation efficiencies compared to the simulation of an electrostatically completely neutral system. As electrostatic agglomeration was excluded by previous simulation studies and Coulomb attraction as well as induced dipole effects were omitted by grounding the wired weaves, these differences have been assigned to so-called mirror charge effects. Comparing the simulation to measurements using corona-discharged dust particles led to the expected good agreement. Since ideally spherical particles are modeled in the simulation, this observation only applies to the measured separation efficiencies based on aerodynamic particle sizes. In contrast, optically measured particle diameters lead to deviations due to the strongly non-spherical shape of ISO fine dust particles.

Using diverse test aerosols in experimental investigations of real cabin air filter media led to large differences in the resulting separation behavior. These differences have been assigned to different charging states of DEHS, sodium chloride and ISO fine dust particles. The subsequent analysis of different combinations of charged/discharged filter media with untreated (charged)/discharged ISO fine dust particles also showed a significant influence of different electrostatic separation mechanisms. In addition to the mirror charge effects detected for grounded wired weaves, the separation due to induced dipoles in neutral particles was observed.

Which directions are recommended for future research studies in the field of cabin air filtration?

In order to reliably predict the filtration performance of cabin air filters, future simulation studies must involve the following three electrostatic components in addition to the Coulomb forces already implemented in the status quo approach:

Firstly, the altered particle size and charge distribution resulting from the electrostatic agglomeration, secondly, the modeling of induced dipoles and, thirdly, the modeling of mirror charge effects. Validating the individual components is particularly challenging as testing results only provide macroscopic, indirect quantities such as the filtration efficiency. Therefore, the following procedure based on the wired weaves used in this work is proposed. The configuration of the grounded weaves in combination with untreated (charged) dust particles enables the verification of mirror charge effects. Furthermore, controlled electrostatic charging of the conductive wired weaves, i.e., applying a known fiber charge intensity and fiber charge distribution, offers the possibility to verify the influence of induced dipoles formed in neutral particles. Using the fully-coupled modeling approach, an induced dipole can be modeled, for instance, by two superimposed particles, which are oppositely charged and connected to each other. In the vicinity of electrostatically charged fibers, the two bonded particles can slightly shift against each other and, thus, model a dipole. Finally, the additionally effective Coulomb forces must be included. Using a controlled electrostatic charging of the wired weaves in combination with untreated (charged) dust particles this time and taking the previously verified mirror charge effects and induced dipole effects into account, the Coulomb forces can be validated. In order to simulate the big picture of cabin air filtration, it is essential to properly model all electrostatic effects discussed in this thesis in addition to conventional mechanical particle collection. This dissertation contributed to this target by providing model extensions, the definition of numerical and experimental test scenarios and extensive studies.

List of Figures

2.1 Performance metrics of particle filters. 25
2.2 Mechanical collection mechanisms. 26
2.3 Composition of total filtration efficiency. 26
2.4 Electrostatic separation mechanisms. 28
2.5 Corona charging of filter media. 30
2.6 Experimental test facility for filter media. 32
2.7 Uni-directionally coupled status quo modeling approach. 37

3.1 Fully-coupled modeling approach. 56
3.2 Lattice-Boltzmann populations in D3Q19 model. 57
3.3 Lattice-Boltzmann two-step algorithm. 58
3.4 Short-range Hertzian and harmonic bond potentials. 61
3.5 Dynamic particle bonding mechanisms. 62
3.6 Modeling particle deposition process. 63
3.7 Long-range Coulomb potential. 65
3.8 Linked-cell algorithm. 67

4.1 Single fiber model. 73
4.2 Influence of coupling intensity on single fiber efficiency. 78
4.3 Influence of inflow length for uni-directional coupling. 79
4.4 Influence of inflow length for fully-coupled approach. 80
4.5 Single fiber efficiencies for a varying fiber offset. 83
4.6 Single fiber efficiencies for varying Reynolds numbers. 84

4.7 Unipolar surface charge density in GeoDict. 87
4.8 Dipole surface charge density in GeoDict. 88
4.9 Electrostatic potential of a unipolarly charged single fiber. 89
4.10 Electrostatic potential of a unipolarly charged single fiber. 89
4.11 Particle trajectories around unipolarly charged single fibers. 90
4.12 Collection efficiency of unipolarly charged single fiber. 91
4.13 Electrostatic potentials for dipole charged fibers. 92
4.14 Particle trajectories around dipole charged fibers. 93
4.15 Collection efficiency of charged single fibers. 94
4.16 Single fiber collection efficiencies for different dipole rotation angles. 95
4.17 Unipolarly and dipole charged fiber arrays in GeoDict. 97
4.18 Dipole charged fiber arrays in GeoDict. 99
4.19 Particle trajectories around unipolarly charged fiber arrays. 101
4.20 Collection efficiency of unipolarly charged fiber arrays. 102
4.21 Electrostatic potential of charged fiber arrays. 103
4.22 Particle trajectories around dipole charged fiber arrays. 104
4.23 Collection efficiency of dipole charged fiber arrays. 105
4.24 Electrostatic potential of charged fiber arrays. 106
4.25 Collection efficiency of dipole charged fiber arrays. 107
4.26 Particle trajectories around charged fiber arrays. 108

5.1 Simulation dimensions for GeoDict and ESPResSo. 114
5.2 Particle size distribution of ISO fine dust. 116
5.3 Published data for particle mean charge distribution. 117
5.4 Particle mean charge distribution used in the simulation. 118
5.5 Gaussian charge distributions for different particle size classes. . . . 119
5.6 Discrete particle size distributions used for the simulation. 121
5.7 Discrete particle charge distributions used for the simulation. 122
5.8 Simulation of electrostatic particle dynamics. 123
5.9 Evolution of relative particle number. 124
5.10 Evolution of particle charge distribution. 125
5.11 Evolution of particle size distribution. 127
5.12 'Artificial filtration' efficiency. 128
5.13 Simulation results for different boundary conditions. 129

5.14 Simulation results for different domain sizes. 130
5.15 Simulation results for different mean particle charge distributions. . 132
5.16 CAD model of test channel. 134
5.17 Simulated air flow in the test channel. 136
5.18 Simulated particle trajectories in the test channel. 138
5.19 'Artificial filtration' efficiency in the test channel. 139
5.20 Experimentally determined 'artificial filtration' efficiency for charged particles. 144
5.21 Experimentally determined 'artificial filtration' efficiencies for discharged particles. 145

6.1 Specification of wired weaves. 151
6.2 Influence of sensor position. 157
6.3 Influence of dust loading. 159
6.4 Influence of particle measurement technique. 161
6.6 Influence of particle discharging (OPCS). 162
6.5 Detailed influence of particle measurement technique. 163
6.7 Influence of particle discharging (APS). 164
6.8 Detailed influence of particle discharging (OPC). 166
6.9 Detailed influence of particle discharging (APS). 167
6.10 Simplified structure of a plain weave. 169
6.11 Inlfuence of different flow solvers on neutral particle trajectories. . . 171
6.12 Simulated collection efficiencies of wired weaves. 173
6.13 Influence of electrostatic particle charges on trajectories. 175
6.14 Strong scaling experiment. 177
6.15 Domain decomposition for strong scaling experiment. 178
6.16 Comparison of simulation results with experiments using discharged particles. 180
6.17 Comparison of simulation results with experiments using untreated (charged) particles. 182

7.1 Three-dimensional digital models for CAF media. 187
7.2 SEM images of CAF media. 188
7.3 Size distribution of different test aerosols. 193

7.4 Separation efficiencies with different test aerosols. 194
7.5 Separation efficiencies for different electrostatic charging states. . . 196
7.6 Simulation experiment setup for CAF media. 199
7.7 Simulated separation efficiencies for different test aerosols. 201
7.8 Comparison of simulation results with experiments. 202
7.9 Fit functions for mean particle charge distribution. 203
7.10 Simulation results for different particle charge distributions. 205

List of Tables

3.1 Specification of reduced units. 66

4.1 Parameters used for the simulation of single fibers. 76

5.1 Parameters used for the simulation of the test facility. 135
5.2 Testing conditions for 'artificial filtration' efficiency. 141

6.1 Testing conditions for wired weaves. 154
6.2 Parameters for the simulation of wired weaves. 170
6.3 Runtimes for the simulation of wired weaves. 179

7.1 Testing conditions for CAF with different test aerosols. 191
7.2 Testing conditions for CAF with different electrostatic charging states. 192

List of Abbreviations

CAF	Cabin Air Filter
MPPS	Most Penetrating Particle Size
xCT	x-Ray Micro-Computed Tomography
OPC	Optical Particle Counter
APS	Aerodynamic Particle Sizer
SMPS	Scanning Mobility Particle Sizer
NaCl	Sodium Chloride
DEHS	Di-Ethyl-Hexyl-Sabacat
LIR	Left Identity Right
MD	Molecular Dynamics
LBM	Lattice-Boltzmann Method
BGK	Bhatnagar-Gross-Krook
SF	Single Fiber
FA	Fiber Array
WW	Wired Weave

Bibliography

[1] P. Ahlrichs and B. Dünweg. "Simulation of a single polymer chain in solution by combining lattice Boltzmann and molecular dynamics." In: *The Journal of Chemical Physics* 111.17 (1999), pp. 8225–8239 (cit. on p. 77).

[2] A. Arnold, J. de Joannis, and C. Holm. "Electrostatics in Periodic Slab geometries I." In: *The Journal of Chemical Physics* 117.6 (2002), pp. 2496–2502 (cit. on p. 65).

[3] A. Arnold and C. Holm. "Efficient Methods to Compute Long-Range Interactions for Soft Matter Systems." In: *Advanced Computer Simulation Approaches for Soft Matter Sciences, in: Advances in Polymer Sciences*. Vol. II. Springer, 2005, pp. 59–109 (cit. on p. 65).

[4] A. Arnold and C. Holm. "MMM2D: A fast and accurate summation method for electrostatic interactions in 2D slab geometries." In: *Computer Physics Communications* 148.3 (2002), pp. 327–348 (cit. on p. 65).

[5] A. Arnold, O. Lenz, S. Kesselheim, R. Weeber, F. Fahrenberger, D. Roehm, P. Košovan, and C. Holm. "ESPResSo 3.1: Molecular Dynamics Software for Coarse-Grained Models." In: *Meshfree Methods for Partial Differential Equations*. Vol. VI. Springer, 2013, pp. 1–23 (cit. on pp. 65, 66, 77).

[6] H. Banzhaf. "Analytische, numerische und experimentelle Untersuchungen zur Abscheidung von Partikeln aus Ölen mit Hilfe fasriger Tiefenfiltermedien." PhD thesis. University of Stuttgart, 2004 (cit. on p. 50).

[7] T. Batt. "Entwicklung eines Meltblow-Verfahrens zur Herstellung thermoplastischer Feinstfaser-Vliesstoffe." PhD thesis. University of Stuttgart, 2015 (cit. on p. 30).

[8] H. Baumgartner, F. Löffler, and H. Umhauer. "Deep-Bed Electret Filters: The Determination of Single Fiber Charge and Collection Efficiency." In: *IEEE Transactions on Electrical Insulation* 3 (1986), pp. 477–486 (cit. on p. 50).

[9] H. Baumgartner and F. Löffler. “Three-Dimensional Numerical Simulation of the Deposition of Polydisperse Aerosol Particles on Filter Fibres – Extended Concept and Preliminary Results.” In: *Journal of Aerosol Science* 18.6 (1987), pp. 885–888 (cit. on p. 47).

[10] H. Baumgartner, C. Piesch, and H. Umhauer. “High-Speed Cinematographic Recording and Numerical Simulation of Particles Depositing on Electret Fibres.” In: *Journal of Aerosol Science* 24.7 (1993), pp. 945–962 (cit. on pp. 27, 47, 71).

[11] H. Baumgartner and F. Löffler. “The Collection Performance of Electret Filters in the Particle Size Range 10 nm − 10 µm.” In: *Journal of Aerosol Science* 17.3 (1986), pp. 438–445 (cit. on pp. 47, 50, 85).

[12] J. Becker, L. Cheng, C. Kronsbein, and A. Wiegmann. “Simulation of Cake Filtration for Polydisperse Particles.” In: *Chemical Engineering & Technology* 39.3 (2016), pp. 559–566 (cit. on pp. 39, 50).

[13] J. Becker, A. Wiegmann, F. J. Hahn, and M. J. Lehmann. “Improved Modeling of Filter Efficiency in Life-Time Simulations on Fibrous Filter Media.” In: *Proceedings of Filtech Conference, Germany*. 2013 (cit. on p. 50).

[14] C. E. Billings. “Effects of Particle Accumulation in Aerosol Filtration.” PhD thesis. California Institute of Technology, 1966 (cit. on p. 45).

[15] D. H. Boal. *Mechanics of the Cell*. Cambridge University Press, 2002 (cit. on p. 64).

[16] R. Brown. “A Many-Fibre Model of Airflow Through a Fibrous Filter.” In: *Journal of Aerosol Science* 15.5 (1984), pp. 583–593 (cit. on p. 95).

[17] R. Brown. “Capture of Dust Particles in Filters by Linedipole Charged Fibres.” In: *Journal of Aerosol Science* 12.4 (1981), pp. 349–356 (cit. on pp. 47, 85).

[18] R. Brown, D. Wake, and P. Smith. “An electrically augmented filter made from conducting and dielectric fibres.” In: *Journal of Electrostatics* 33.3 (1994), pp. 393–412 (cit. on p. 24).

[19] R. C. Brown. *Air filtration: an integrated approach to the theory and applications of fibrous filters*. Pergamon, 1993 (cit. on p. 46).

[20] M. Buchholz. “Framework zur Parallelisierung von Molekulardynamiksimulationen in verfahrenstechnischen Anwendungen.” PhD thesis. Technical University of Munich, 2010 (cit. on p. 67).

[21] J. J. Cerda, V. Ballenegger, O. Lenz, and C. Holm. "P^3M algorithm for dipolar interactions." In: *The Journal of Chemical Physics* 129.23 (2008), p. 234104 (cit. on p. 68).

[22] C. Davies. "Filtration of Aerosols." In: *Journal of Aerosol Science* 14.2 (1983), pp. 147–161 (cit. on pp. 45, 71).

[23] G. S. Dawkins. "Electrostatic Effects in the Deposition of Aerosols on Cylindrical Shapes." PhD thesis. University of Illinois at Urbana-Champaign, 1957 (cit. on p. 85).

[24] P. De Haan, J. Van Turnhout, and K. Wapenaar. "Fibrous and Granular Filters with Electrically Enhanced Dust Capturing Efficiency." In: *IEEE Transactions on Electrical Insulation* 3 (1986), pp. 465–470 (cit. on p. 18).

[25] M. Deserno and C. Holm. "How to mesh up Ewald sums. I. A theoretical and numerical comparison of various particle mesh routines." In: *The Journal of Chemical Physics* 109.18 (1998), pp. 7678–7693 (cit. on pp. 65, 68).

[26] M. Deserno and C. Holm. "How to mesh up Ewald sums. II. An accurate error estimate for the P^3M algorithm." In: *The Journal of Chemical Physics* 109.18 (1998), pp. 7694–7701 (cit. on pp. 65, 68).

[27] DIN 71 460-1. *Straßenfahrzeuge – Luftfilter für Kraftfahrzeuginnenräume – Teil 1: Prüfverfahren für Partikelfiltration* (cit. on pp. 31, 35, 155, 188).

[28] B. Dünweg and A. J. Ladd. "Lattice Boltzmann simulations of soft matter systems." In: *Advanced Computer Simulation Approaches for Soft Matter Sciences*. Vol. III. Springer, 2009, pp. 89–166 (cit. on pp. 59, 69).

[29] H. Emi, C. Kanaoka, Y. Otani, and T. Ishiguro. "Collection Mechanisms of Electret Filter." In: *Particulate Science and Technology* 5.2 (1987), pp. 161–171 (cit. on p. 27).

[30] H. Emi, K. Okuyama, and M. Adachi. "The Effect of Neighbouring Fibers on the Single Fiber Inertia-Interception Efficiency of Aerosols." In: *Journal of Chemical Engineering of Japan* 10.2 (1977), pp. 148–153 (cit. on p. 44).

[31] B. Fardi and B. Y. Liu. "Efficiency of Fibrous Filters with Rectangular Fibers." In: *Aerosol Science and Technology* 17.1 (1992), pp. 45–58 (cit. on p. 95).

[32] B. Fardi and B. Y. Liu. "Flow Field and Pressure Drop of Filters with Rectangular Fibers." In: *Aerosol Science and Technology* 17.1 (1992), pp. 36–44 (cit. on p. 95).

[33] O. Filippova and D. Hänel. “Lattice-Boltzmann simulation of gas-particle flow in filters.” In: *Computers & Fluids* 26.7 (1997), pp. 697–712 (cit. on pp. 45, 46, 48).

[34] B. Forsyth, B. Y. Liu, and F. J. Romay. “Particle Charge Distribution Measurement for Commonly Generated Laboratory Aerosols.” In: *Aerosol Science and Technology* 28.6 (1998), pp. 489–501 (cit. on pp. 117–119).

[35] J. A. Giacometti and O. N. Oliveira. “Corona Charging of Polymers.” In: *IEEE Transactions on Electrical Insulation* 27.5 (1992), pp. 924–943 (cit. on p. 30).

[36] H. Hamaker. “The London – Van Der Waals Attraction Between Spherical Particles.” In: *Physica* 4.10 (1937), pp. 1058–1072 (cit. on p. 29).

[37] S. Heidenreich. “Hot gas filtration – A review.” In: *Fuel* 104 (2013), pp. 83–94 (cit. on p. 149).

[38] A. Hellmann, K. Schmidt, M. Pitz, and S. Ripperger. “Comparison of measurement and simulation of particle deposition at charged microfibers.” In: *Aerosol Technolgy* (2014) (cit. on p. 51).

[39] C. Helsper and W. Mölter. “Determination and Neutralization of the Charge Produced by the Dispersion of Powders.” In: *Journal of Aerosol Science* 18.6 (1987), pp. 877–880 (cit. on pp. 117, 118).

[40] R. Hiller and F. Löffler. “Der Einfluss von Auftreffgrad und Haftanteil auf die Partikelabscheidung in Faserfiltern.” In: *Staub – Reinhaltung der Luft* 40 (1980) (cit. on pp. 29, 44, 71).

[41] R. Hiller. “Der Einfluß von Partikelstoß und Partikelhaftung auf die Abscheidung in Faserfiltern.” PhD thesis. University of Karlsruhe, 1981 (cit. on pp. 29, 46).

[42] S. Hirschmann, M. Lahnert, C. Schober, M. Brunn, M. Mehl, and D. Pflüger. “Load-Balancing and Spatial Adaptivity for Coarse-Grained Molecular Dynamics Applications.” In: *High Performance Computing in Science and Engineering ‘18* (2018) (cit. on pp. 113, 114).

[43] R. W. Hockney and J. W. Eastwood. “Computer Simulation Using Particles.” In: *McGraw-Hill* (1988) (cit. on p. 68).

[44] ISO 12 103-1. *Road Vehicles – Test Dust for Filter Evaluation – Part 1: Arizona Test Dust*. 1997 (cit. on pp. 33, 115–117).

[45] H. Jodeit and F. Löffler. “The Influence of Electrostatic Forces upon Particle Collection in Fibrous Filters.” In: *Journal of Aerosol Science* 15.3 (1984), pp. 311–317 (cit. on pp. 27, 85).

[46] A. Johnston, J. Vincent, and A. Jones. “Electrical Charge Characteristics of Dry Aerosols Produced by a Number of Laboratory Mechanical Dispensers.” In: *Aerosol Science and Technology* 6.2 (1987), pp. 115–127 (cit. on p. 117).

[47] C. Kanaoka, S. Hiragi, and W. Tanthapanichakoon. “Stochastic simulation of the agglomerative deposition process of aerosol particles on an electret fiber.” In: *Powder Technology* 118.1-2 (2001), pp. 97–106 (cit. on pp. 27, 48).

[48] C. Kanaoka, H. Emi, and T. Myojo. “Simulation of the growing process of a particle dendrite and evaluation of a single fiber collection efficiency with dust load.” In: *Journal of Aerosol Science* 11.4 (1980), pp. 377–389 (cit. on pp. 45–48).

[49] C. Kanaoka, H. Emi, Y. Otani, and T. Iiyama. “Effect of charging state of particles on electret filtration.” In: *Aerosol Science and Technology* 7.1 (1987), pp. 1–13 (cit. on p. 49).

[50] G. Kasper, S. Schollmeier, J. Meyer, and J. Hoferer. “The collection efficiency of a particle-loaded single filter fiber.” In: *Journal of Aerosol Science* 40.12 (2009), pp. 993–1009 (cit. on pp. 44, 71, 72).

[51] M. Kerner, K. Schmidt, A. Hellmann, S. Schumacher, M. Pitz, C. Asbach, S. Ripperger, and S. Antonyuk. “Numerical and experimental study of submicron aerosol deposition in electret microfiber nonwovens.” In: *Journal of Aerosol Science* 122 (2018), pp. 32–44 (cit. on pp. 51, 195, 200).

[52] A. Kilic, S. Russell, E. Shim, and B. Pourdeyhimi. “The Charging and Stability of Electret Filters.” In: *Fibrous Filter Media*. Elsevier, 2017, pp. 95–121 (cit. on pp. 30, 31).

[53] H. F. Kraemer and H. F. Johnstone. “Collection of Aerosol Particles in Presence of Electrostatic Fields.” In: *Industrial & Engineering Chemistry* 47.12 (1955), pp. 2426–2434 (cit. on p. 85).

[54] S. Kuwabara. “The Forces experienced by Randomly Distributed Parallel Circular Cylinders or Spheres in a Viscous Flow at Small Reynolds Numbers.” In: *Journal of the Physical Society of Japan* 14.4 (1959), pp. 527–532 (cit. on p. 45).

[55] P. Lallemand, D. d’Humieres, L.-S. Luo, and R. Rubinstein. “Theory of the lattice Boltzmann method: Three-dimensional model for linear viscoelastic fluids.” In: *Physical Review E* 67.2 (2003) (cit. on p. 66).

[56] U. Lantermann and D. Hänel. “Particle Monte Carlo and lattice-Boltzmann methods for simulations of gas–particle flows.” In: *Computers & Fluids* 36.2 (2007), pp. 407–422 (cit. on p. 49).

[57] R. Lathrache, H. Fissan, and S. Neumann. “Deposition of submicron particles on electrically charged fibers.” In: *Journal of Aerosol Science* 17.3 (1986), pp. 446–449 (cit. on p. 47).

[58] A. Latz and A. Wiegmann. “Simulation of fluid particle separation in realistic three dimensional fiber structures.” In: *Proceedings of Filtech Conference, Düsseldorf, Germany* (2003) (cit. on p. 49).

[59] A. Latz and A. Wiegmann. “Virtuelles Filtermaterialdesign mit GeoDict/FilterDict.” In: *Laboratory IT User Service* 1 (2004) (cit. on pp. 49, 50).

[60] K. Lee and B. Liu. “On the Minimum Eefficiency and the Most Penetrating Particle Size for Fibrous Filters.” In: *Journal of the Air Pollution Control Association* 30.4 (1980), pp. 377–381 (cit. on p. 25).

[61] M. J. Lehmann. “Untersuchungen zur Struktur und zur Beladungskinetik von Tiefenfiltern.” PhD thesis. University of Karlsruhe (TH), 2005 (cit. on pp. 46, 71).

[62] M. J. Lehmann, J. Weber, A. Kilian, and M. Heim. “Microstructure Simulation as Part of Fibrous Filter Media Development Processes – From Real to Virtual Media.” In: *Chemical Engineering & Technology* 39.3 (2016), pp. 403–408 (cit. on pp. 17, 41, 50).

[63] M. Lehmann, H. Banzhaf, G. Klein, M. Durst, S. Rief, and A. Wiegmann. “Setting a New Milestone in Filter Media Design: Simulating Performance According to Multi Pass Test Based on 3D Fiber Structures.” In: *Proceedings of the 10th World Filtration Congress, Leipzig*. 2008 (cit. on p. 50).

[64] H.-J. Limbach, A. Arnold, B. A. Mann, and C. Holm. “ESPResSo – an extensible simulation package for research on soft matter systems.” In: *Computer Physics Communications* 174.9 (2006), pp. 704–727 (cit. on pp. 60, 65, 68).

[65] S. Linden, A. Wiegmann, and H. Hagen. “The LIR space partitioning system applied to the Stokes equations.” In: *Graphical Models* 82 (2015), pp. 58–66 (cit. on p. 42).

[66] Z. G. Liu and P. K. Wang. “Pressure Drop and Interception Efficiency of Multifiber Filters.” In: *Aerosol Science and Technology* 26.4 (2007), pp. 313–325 (cit. on pp. 95, 96).

[67] L.-S. Luo, W. Liao, X. Chen, Y. Peng, W. Zhang, et al. “Numerics of the lattice Boltzmann method: Effects of collision models on the lattice Boltzmann simulations.” In: *Physical Review E* 83.5 (2011) (cit. on p. 58).

[68] M. Machado, P. Moreira, P. Flores, and H. M. Lankarani. “Compliant contact force models in multibody dynamics: Evolution of the Hertz contact theory.” In: *Mechanism and Machine Theory* 53 (2012), pp. 99–121 (cit. on p. 60).

[69] T. Miyagi. “Viscous flow at low Reynolds numbers past an infinite row of equal circular cylinders.” In: *Journal of the Physical Society of Japan* 13.5 (1958), pp. 493–496 (cit. on pp. 46, 81).

[70] W. Muhr. “Theoretical and experimental investigation of particle deposition in fibrous filters by field and inertial forces.” PhD thesis. University of Karlsruhe, 1976 (cit. on pp. 44, 71).

[71] T. Müller, J. Meyer, and G. Kasper. “Low Reynolds number drag and particle collision efficiency of a cylindrical fiber within a parallel array.” In: *Journal of Aerosol Science* 77 (2014), pp. 50–66 (cit. on pp. 46, 71, 72, 76, 79–84).

[72] T. Myojo, C. Kanaoka, and H. Emi. “Experimental Observation of Collection Efficiency of a Dust-Loaded Fiber.” In: *Journal of Aerosol Science* 15.4 (1983), pp. 483–489 (cit. on pp. 45, 48).

[73] Y.-W. Oh, K.-J. Jeon, A.-I. Jung, and Y.-W. Jung. “A Simulation Study on the Collection of Submicron Particles in a Unipolar Charged Fiber.” In: *Aerosol Science & Technology* 36.5 (2002), pp. 573–582 (cit. on pp. 48, 85).

[74] Y. Otani, H. Emi, and J. Mori. “Initial Collection Efficiency of Electret Filter and Its Durability for Solid and Liquid Particles [Translated].” In: *KONA Powder and Particle Journal* 11 (1993), pp. 207–214 (cit. on p. 47).

[75] Palas GmbH. URL: `https://www.palas.de/`, accessed on February 13, 2019 (cit. on pp. 31, 33, 34, 190).

[76] J. C. Pàmies, A. Cacciuto, and D. Frenkel. “Phase diagram of Hertzian spheres.” In: *The Journal of Chemical Physics* 131.4 (2009) (cit. on p. 60).

[77] J. Pich, H. Emi, and C. Kanaoka. “Coulombic Deposition Mechanism in Electret Filters.” In: *Journal of Aerosol Science* 18.1 (1987), pp. 29–35 (cit. on pp. 27, 85).

[78] R. Przekop and L. Gradoń. “Deposition and Filtration of Nanoparticles in the Composites of Nano-and Microsized Fibers.” In: *Aerosol Science and Technology* 42.6 (2008), pp. 483–493 (cit. on p. 46).

[79] R. Przekop, A. Moskal, and L. Gradoń. "Lattice-Boltzmann approach for description of the structure of deposited particulate matter in fibrous filters." In: *Journal of Aerosol Science* 34.2 (2003), pp. 133–147 (cit. on p. 45).

[80] T. Ptak and T. Jaroszczyk. "Theoretical-experimental aerosol filtration model for fibrous filters at intermediate Reynolds numbers." In: *Proceedings of the* 5$^{\text{th}}$ *World Filtration Congress, Nice, France*. 1990, pp. 566–572 (cit. on pp. 44, 71).

[81] Reifenhäuser Reicofil. URL: `https://www.reicofil.com/`, accessed on February 13, 2019 (cit. on pp. 186–188).

[82] H.-J. Rembor, R. Maus, and H. Umhauer. "Measurements of Single Fibre Efficiencies at Critical Values of the Stokes Number." In: *Particle & Particle Systems Characterization* 16.2 (1999), pp. 54–59 (cit. on pp. 44, 71).

[83] S. Rief, O. Iliev, D. Kehrwald, A. Latz, K. Steiner, and A. Wiegmann. "Simulation und virtuelles Design von Filtermedien und Filterelementen." In: *Durst, GM, und Klein, M.(eds.) Filtration in Fahrzeugen. Expert-Verlag, Renningen* (2006) (cit. on p. 50).

[84] S. Rief, D. Kehrwald, K. Schmidt, and A. Wiegmann. "Fraunhofer Software Tools GeoDict/FilterDict for the Simulation of Diesel Particulate Filters." In: *NAFEM: Reliable Use of Numerical Methods in Upfront Simulations. Wiesbaden, Germany* (2007) (cit. on p. 50).

[85] S. Rief, A. Latz, and A. Wiegmann. "Computer simulation of air filtration including electric surface charges in three-dimensional fibrous micro structures." In: *Filtration* 6.2 (2006), pp. 169–172 (cit. on pp. 27, 51).

[86] D. Röhm and A. Arnold. "Lattice Boltzmann simulations on GPUs with ESPResSo." In: *The European Physical Journal Special Topics* 210.1 (2012), pp. 89–100 (cit. on pp. 65, 67).

[87] Sandler AG. URL: `https://www.sandler.de/`, accessed on February 13, 2019 (cit. on pp. 187, 188).

[88] U. D. Schiller. "Thermal fluctuations and boundary conditions in the lattice Boltzmann method." PhD thesis. University of Mainz (JGU), 2008 (cit. on pp. 57, 69).

[89] K. Schmidt, A. Hellmann, M. Pitz, and S. Ripperger. "Modeling of NaCl Aerosol Deposition at Electrically Charged Microfibers." In: *Proceedings of Filtech Conference, Germany*. 2013 (cit. on p. 51).

[90] C. Schober, D. Keerl, F. Keller, M. Lehmann, and M. Mehl. “Influence of Bipolar Dust Particle Charges on the Filtration Efficiency of Wired Weaves.” In: *Journal of Aerosol Science (submitted)* (2018) (cit. on pp. 115, 118, 119, 124, 125, 127, 132, 151, 165).

[91] C. Schober, D. Keerl, M. Lehmann, and M. Mehl. “Simulating the Interaction of Electrostatically Charged Particles in the Inflow Aera of Cabin Air Filters Using a Fully Coupled System.” In: *Proceedings of the VII International Conference on Coupled Problems in Science and Engineering, Rhodes* (2017), pp. 77–88 (cit. on pp. 59, 168, 169, 171).

[92] E. Schweers, H. Umhauer, and F. Löffler. “Experimental Investigation of Particle Collection on Single Fibres of Different Configurations.” In: *Particle & Particle Systems Characterization* 11.4 (1994), pp. 275–283 (cit. on pp. 44, 71).

[93] Spörl KG Präzisionsdrahtweberei. *Metallgewebe Broschüre*. URL: `http://www.spoerl.de/produkte/metallgewebe/download-broschuere/`, accessed on October 18, 2018 (cit. on pp. 149, 150).

[94] J. Stratton. “Electromagnetic Theory.” In: *McGraw-Hill* (1941), pp. 31–434 (cit. on p. 51).

[95] S. Succi. *The Lattice Boltzmann Equation: for Fluid Dynamics and Beyond*. Oxford University Press, 2001 (cit. on p. 67).

[96] S. Suneja and C. Lee. “Aerosol Filtration by Fibrous Filters at Intermediate Reynolds Numbers (≤ 100).” In: *Atmospheric Environment* 8.11 (1974), pp. 1081–1094 (cit. on pp. 44, 71).

[97] W. Tanthapanichakoon, K. Maneeintr, T. Charinpanitkul, and C. Kanaoka. “Estimation of collection efficiency enhancement factor for an electret fiber with dust load.” In: *Journal of Aerosol Science* 34.11 (2003), pp. 1505–1522 (cit. on p. 48).

[98] TSI Incorporated. URL: `https://www.sandler.de/`, accessed on March 8, 2019 (cit. on pp. 35, 36).

[99] D. Walsh and J. Stenhouse. “Clogging of an electrically active fibrous filter material: experimental results and two-dimensional simulations.” In: *Powder Technology* 93.1 (1997), pp. 63–75 (cit. on p. 47).

[100] D. Walsh and J. Stenhouse. “Parameters affecting the loading behavior and degradation of electrically active filter materials.” In: *Aerosol Science and Technology* 29.5 (1998), pp. 419–432 (cit. on p. 50).

[101] D. Walsh and J. Stenhouse. “The effect of particle size, charge, and composition on the loading characteristics of an electrically active fibrous filter material.” In: *Journal of Aerosol Science* 28.2 (1997), pp. 307–321 (cit. on p. 50).

[102] D. Walsh and I. Stenhouse. “Experimental studies of electrically active fibrous filter loading.” In: *Particle & Particle Systems Characterization* 13.1 (1996), pp. 47–53 (cit. on p. 50).

[103] C.-S. Wang. “Electrostatic forces in fibrous filters – a review.” In: *Powder Technology* 118.1-2 (2001), pp. 166–170 (cit. on p. 31).

[104] H. Wang, H. Zhao, Z. Guo, and C. Zheng. “Numerical simulation of particle capture process of fibrous filters using Lattice Boltzmann two-phase flow model.” In: *Powder Technology* 227 (2012), pp. 111–122 (cit. on p. 46).

[105] T. Warth. “Experimentelle und numerische Untersuchung von Strömungswiderstand, Abscheide- und Abreinigungsverhalten metallischer Filtermedien.” PhD thesis. University of Stuttgart, 2013 (cit. on p. 153).

[106] T. Warth and M. Piesche. “Experimentelle und numerische Untersuchung der Abscheidung an Metallfiltermedien unter Berücksichtigung von Partikel/Faser-Interaktionen.” In: *Chemie Ingenieur Technik* 85.10 (2013), pp. 1559–1567 (cit. on pp. 35, 181).

[107] J. Wei, C. Chun-Shun, C. Cheong-Ki, and Z. Chao. “The aerosol penetration through an electret fibrous filter.” In: *Chinese Physics* 15.8 (2006), p. 1864 (cit. on p. 48).

[108] A. Wiegmann. *GeoDict. The virtual material laboratory.* © 2001-2011 Fraunhofer ITWM, © 2012-2019 Math2Market GmbH. URL: `https://www.geodict.com`, accessed on March 15, 2019 (cit. on pp. 37, 40).

[109] A. Wiegmann and K. P. Bube. “The explicit-jump immersed interface method: finite difference methods for PDEs with piecewise smooth solutions.” In: *SIAM Journal on Numerical Analysis* 37.3 (2000), pp. 827–862 (cit. on p. 42).

[110] A. Wiegmann, S. Rief, and A. Latz. “Virtual material design and air filtration simulation techniques inside GeoDict and FilterDict.” In: *Proceedings of the American Filtration and Separation Society, Atlanta, USA*. 2005 (cit. on pp. 41, 42, 51).

[111] Z. Wu, I. Colbeck, and G. Zhang. “Deposition of Particles on a Single Cylinder by a Coulombic Force and Direct Interception.” In: *Aerosol Science and Technology* 19.1 (1993), pp. 40–50 (cit. on p. 27).

[112] H.-C. Yeh and B. Y. Liu. "Aerosol Filtration by Fibrous Filters – I. Theoretical." In: *Journal of Aerosol Science* 5.2 (1974), pp. 191–204 (cit. on p. 71).

[113] H.-C. Yeh and B. Y. Liu. "Aerosol Filtration by Fibrous Filters – II. Experimental." In: *Journal of Aerosol Science* 5.2 (1974), pp. 205–217 (cit. on p. 71).

[114] D. P. Ziegler. "Boundary Conditions for Lattice Boltzmann Simulations." In: *Journal of Statistical Physics* 71.5-6 (1993), pp. 1171–1177 (cit. on p. 67).

All URLs were last checked on July 1, 2019.

Declaration of Authorship

I hereby declare that this thesis titled

Modeling and Simulation of Cabin Air Filtration with Focus on Electrostatic Effects

was independently completed. Information taken directly or indirectly from external sources is properly marked as such.

Stuttgart, March 30, 2019